FEDERAL UNIVERSITY OF SANTA MARIA
TECNOLOGY CENTER
GRADUATE PROGRAM
IN ELECTRICAL ENGINEERING

Cesar José Volpato Filho

ADAPTIVE FULL-ORDER OBSERVER ANALYSIS AND DESIGN FOR FULL-RANGE SENSORLESS INTERIOR PERMANENT MAGNET SYNCHRONOUS MOTOR DRIVES

Santa Maria, RS
2021

Cesar José Volpato Filho

ADAPTIVE FULL-ORDER OBSERVER ANALYSIS AND DESIGN FOR FULL-RANGE SENSORLESS INTERIOR PERMANENT MAGNET SYNCHRONOUS MOTOR DRIVES

Thesis presented to the Graduate Program in Electrical Engineering, Concentration Area in Energy Processing, Federal University of Santa Maria (UFSM-RS), as a partial requirement in order to obtain the degree of **Doctor in Electrical Engineering**.

Advisor: Prof. Dr. Rodrigo Padilha Vieira

Santa Maria, RS
2021

Declaro, CESAR JOSé VOLPATO FILHO, para os devidos fins e sob as penas da lei, que a pesquisa constante neste trabalho de conclusão de curso (Tese) foi por mim elaborada e que as informações necessárias objeto de consulta em literatura e outras fontes estão devidamente referenciadas. Declaro, ainda, que este trabalho ou parte dele não foi apresentado anteriormente para obtenção de qualquer outro grau acadêmico, estando ciente de que a inveracidade da presente declaração poderá resultar na anulação da titulação pela Universidade, entre outras consequências legais.

Cesar José Volpato Filho

ADAPTIVE FULL-ORDER OBSERVER ANALYSIS AND DESIGN FOR FULL-RANGE SENSORLESS INTERIOR PERMANENT MAGNET SYNCHRONOUS MOTOR DRIVES

> Thesis presented to the Graduate Program in Electrical Engineering, Concentration Area in Energy Processing, Federal University of Santa Maria (UFSM-RS), as a partial requirement in order to obtain the degree of **Doctor in Electrical Engineering**.

Approved on October 22, 2021

Rodrigo Padilha Vieira, Dr. (UFSM)
(President/Advisor - Video conference)

Aurélio Tergolina Salton, Dr. (UFRGS)
(Video conference)

Helder Tavares Câmara, Dr. (Danfoss)
(Video conference)
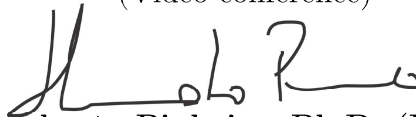
Humberto Pinheiro, Ph.D. (UFSM)
(Video conference)

Lucas Vizzotto Bellinaso, Dr. (UFSM)
(Video conference)

Santa Maria, RS, Brazil
2021

"To improve is to change, so to be perfect is to change often."

Winston Churchill

ACKNOWLEDGMENT

ABSTRACT

ADAPTIVE FULL-ORDER OBSERVER ANALYSIS AND DESIGN FOR FULL-RANGE SENSORLESS INTERIOR PERMANENT MAGNET SYNCHRONOUS MOTOR DRIVES

Author: Cesar José Volpato Filho
Advisor: Rodrigo Padilha Vieira

This Thesis presents contributions to the study, development, analysis and design of adaptive observers applied to the estimation of rotor position and speed of interior permanent magnet synchronous motors (IPMSM). The position estimation techniques for the IPMSM are divided in low and high speed methods. First, the adaptive full-order observer analysed and designed for high speed sensorless control. A cascade design method is presented for high performance estimation and robustness improvement under speed estimation error. An analysis of parameter variation effects on position and speed estimation is presented. Then, the adaptive full-order observer is modified for full-range IPMSM sensorless control. A high-frequency injection technique is used in order to guarantee position observability. The cascade design approach is adopted for the adaptive observer gains design. Experimental results are presented in order to validate the proposed adaptive observer design method.

Key-words: Interior permanent magnet synchronous motor, adaptive observer, position estimation, sensorless control.

LIST OF FIGURES

SYMBOL LIST

L	Stator Inductance
R	Stator Resistance
$L_{d,q}$	Synchronous Inductance
ρ	Diferencial Operator
ψ	Magnet Flux Constant
$i_{d,q}$	Currents in the Synchronous Reference
$v_{d,q}$	Voltages in the Synchronous Reference
$i_{\alpha,\beta}$	Currents in the Stationary Reference
$\hat{i}_{\alpha,\beta}$	Observed Currents in the Stationary Reference
$\tilde{i}_{\alpha,\beta}$	Observed Currents Error in the Stationary Reference
$v_{\alpha,\beta}$	Voltages in the Stationary Reference
ω_r	Rotor Speed
$\hat{\omega}_r$	Observed Rotor Speed
$\tilde{\omega}_r$	Rotor Speed Estimation Error
ω_e	Rotor Flux Speed
$\hat{\omega}_e$	Observed Rotor Flux Speed
$\tilde{\omega}_e$	Rotor Flux Speed Estimation Error
θ_e	Rotor Flux Position
$\hat{\theta}_e$	Estimated Rotor Flux Position
$\tilde{\theta}_e$	Estimated Rotor Flux Position Error
$e_{\alpha,\beta}$	Extended Electromotive Force
$\hat{e}_{\alpha,\beta}$	Observed Extended Electromotive Force
$\tilde{e}_{\alpha,\beta}$	Observed Extended Electromotive Force Error
$h_{1,2,3,4}$	Observer Feedback Gains
$k_{p,i}$	Observer Adaptive Gains
$\Gamma_{1,2}$	Cascade Design Poles
$Q_{\alpha,\beta}$	Quadratic Electromotive Force
$Q_{\alpha,\beta}^n$	Normalized Quadratic Electromotive Force
$\hat{Q}_{\alpha,\beta}$	Observed Quadratic Electromotive Force
$Q_{\alpha,\beta}^n$	Observed Normalized Quadratic Electromotive Force
f_h	Frequency of the Signal Injection
v_h	Magnitude of the Signal Injection

SUMARY

1 INTRODUCTION

1.1 Motivation

The recent technological developments combined with productivity growth, which lower products prices, have enabled the used of electric motors in more and new applications. Electric motors make up 53 % of the world electricity consumption (ANNEX, 2016). In the industry sector, electric motors have an even greater share in the consumption of electricity, estimated in about two thirds. In addition to the large amount of energy used by electric motors, high growth is also expected in the coming years. In the developed countries, such as the United States and Germany, the growth for new electric motors installed is estimated at 1% to 3% a year. In emerging markets, such as India and China, the electric motor installation growth can reach levels of 6% a year (IEA, 2011).

Within this context, high performance control of electrical motors emerges as a method of saving large amounts of energy. Modern electrical drives extracts the maximum performance from the electric motors due to its variable speed capabilites. The replacement of classic drive methods with the modern electric motor drives has electricity savings potentials of 50% (IEA, 2018). Furthermore, with the recent technology evolution, modern electrical drives have been gaining ground in applications outside the conventional industry, such as in robotics, drones and electric vehicles (EVs).

Electric vehicle(EV) sales broke a new record in 2018, surpassing the 2 million mark and making up 2.2% of the global market share. With impressive 49.18% of the total car sales composed of EV, Norway has stood out in adopting the new technology, followed by Iceland and Sweden, with 19.14% and 8%, respectively. The countries with highest EV market share in 2018 are illustrated in Figure 1.1. In absolute numbers, China was the largest market for electric vehicles, with 1.1 million sales and accounting for about 50 % of electric cars sold in the world and accounting for more than double that of the United States, second in the ranking with 358 thousands of units sold. Exponential growth is expected to continue in the next few decades as the concerns about the use of fossil fuels increases (IEA, 2017).

Another consolidated application of electric motors, which also shows exponential growth, is wind turbines (BLAABJERG; MA, 2013). The wind power market reached 742 GW of total capacity in 2020 (REN21, 2021), with China and the United States as dominant producers. As a share of the total electricity generation, several countries rely on wind power as a major source, such as Denmark with over 58%, Uruguay with 40.4%, Ireland with 38% and the United Kingdom with 24.2%.

Commercial industrial drives are an important drive tool which can be used for a large range of motors (WEG, 2013). Furthermore, this industrial drives may have the

Figure 1.1: Countries with highest EV market share at 2018.
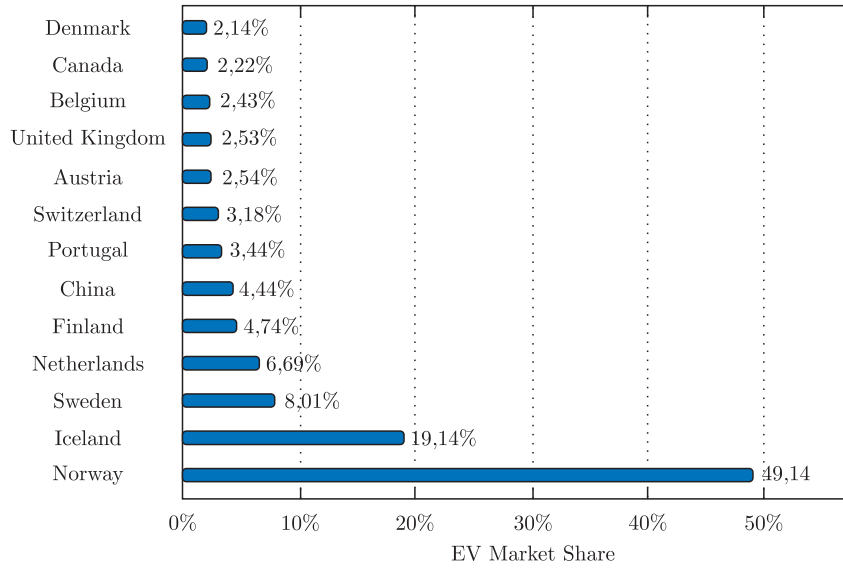
Source: Adapted from (EV-VOLUMES.COM, 2018).

capacity of estimating the machine parameters, thus being able to be used for motors not designed to used by the industrial drive previously. Commercial industrial drives have also sensorless control capabilities, making the speed control process be performed without the use of position and speed sensors.

1.2   Electric Motor Drives

An electric motor drive is used in order to convert electrical energy into mechanical energy with high efficiency. A general classification of the major electric motors types used in electric drives is presented in Fig. 1.2.

In low power applications, the DC motor is preferred due to its simple control and low cost. However, poor power density and low efficiency are important deficiencies that limit its use in other applications. The induction motor (IM) was the first electric machine used extensively in modern electric drives, being a major choice in the first EVs (RAMESH; LENIN, 2019). This is due to its constructive simplicity, which implies low production cost, low maintenance cost, good performance and robustness. In recent years, the permanent magnet synchronous machine (PMSM) has been gaining ground in applications that require high efficiency and reduced volume. The PMSM magnets can be constructed in different forms on the motor rotor. The simplest way in order to manufacture the PMSM rotor is insert the magnets on the surface of the rotor, being this form of construction known as surface PMSM (SPMSM). This method has lower cost with the drawback of losing efficiency. The insertion of the magnets in the interior of the rotor is used for higher efficiency applications where a higher performance and

additional mechanical robustness is required. This manufacturing process is known as interior PMSM (IPMSM).

The synchronous reluctance motor (SynRM) has emerged as a viable alternative for the PMSM in high-performance applications. This is mainly due to the very large reserves of rare-earth materials, used in PMSM, that China has in comparison with other countries, which led to supply concerns by some manufacturers. The absence of magnets and windings on the rotor is also a characteristic of the switched reluctance motor (SRM). Such aspect makes the SRM highly robust, thus being able to reach high temperatures up tp 400 °C. As main disadvantages of the SRM, are the lower power density and efficiency in comparison with the PMSM. Another major issue with the SRM is the high torque ripples generated by the double-salient format. The main features of the presented electrical motor types, such as power density, efficiency, controllability, manufacturing simplicity, and cost are illustrated in Fig. 1.3. It should be pointed out that these features are highly dependent on the operating conditions, motor materials and manufacturing quality. For exemple, the SRM can have a higher efficiency than the PMSM at higher speeds (SAYED et al., 2021).

An comprehensive state of the art review of modeling of electric motors is per-

Figure 1.2: Representation of the major electric motors types. (a) DC motor, (b) SPMSM, (c) IPMSM, (d) SynRM, (e) SRM, (f) Induction motor.
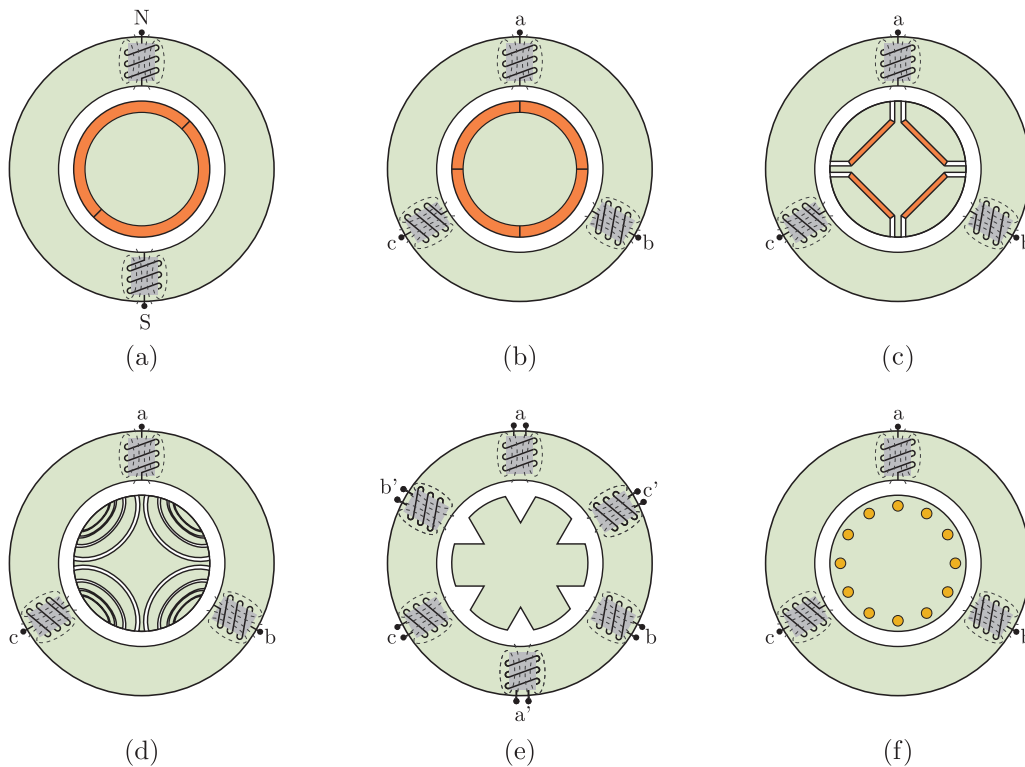
Source: Author.

Figure 1.3: Schematics of the major electric motors types features (more is better). (a) DC motor, (b) SPMSM, (c) IPMSM, (d) SynRM, (e) SRM, (f) Induction motor.
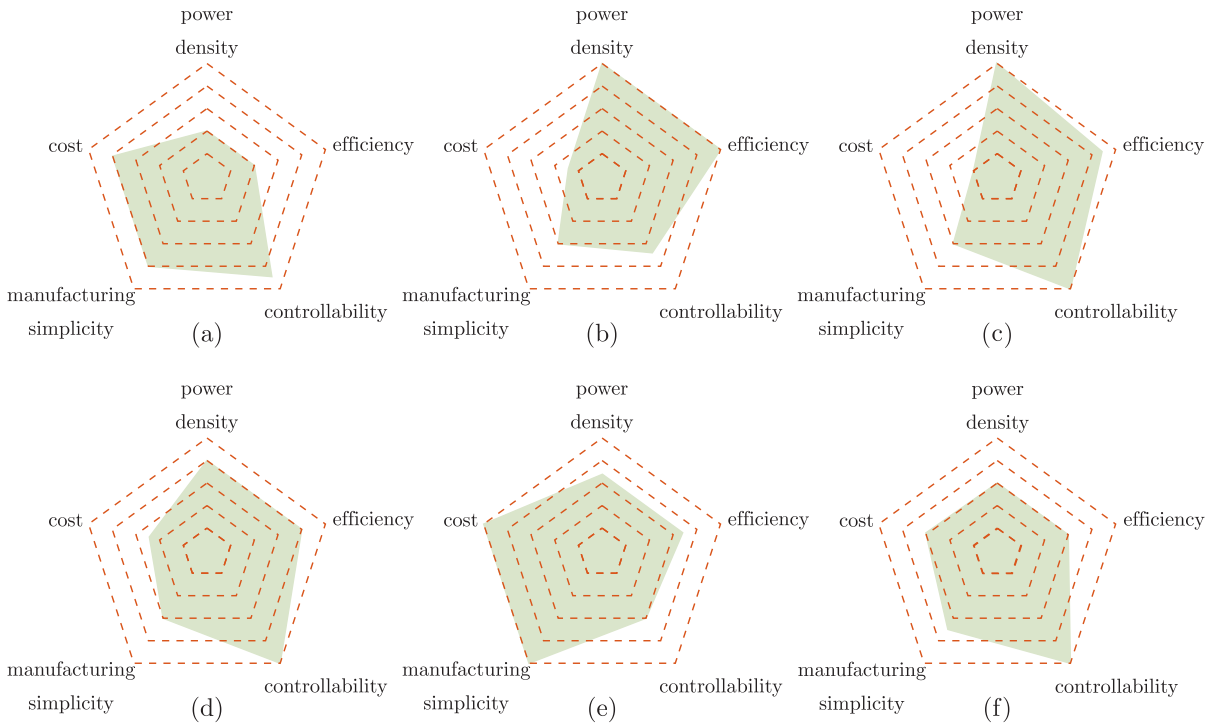
Source: Adapted from (RAMESH; LENIN, 2019) and (SAYED et al., 2021).

formed in (BILGIN et al., 2019). In this study, the important aspects of high-performance drives, such as dynamic modeling, demagnetization analysis, loss calculations, thermal modeling, vibration analysis, acoustic noise analysis and mechanical stress modeling are investigated.

1.2.1   IPMSM Drives

Torque generated by both reluctance and magnetic torque is the major characteristic of the IPMSM. However, different rotor constructive characteristics can cause both torques type having different weights in the final machine torque. When the both magnetic and reluctance torque are significant, the machine is named IPMSM. A dominant torque magnetic torque with a small reluctance torque is produced by the Inset SPMSM. In the other way around, the permanent magnet assisted synchronous reluctance motors (PMASynRM) have high reluctance torque and low magnetic torque. The classification of the synchronous motors by torque generation type is illustrated in Fig. 1.4.

The permanent magnet are made it with rare-earth materials, such as samarium, terbium, neodymium and dysprosium, or non-rare-earth materials, such as alnico and ferrite (TAHANIAN; ALIAHMADI; FAIZ, 2020). Demagnetization of the permanent magnet materials can cause meaningful reduction in the IPMSM output torque. High-

Figure 1.4: Synchronous motors definition by torque type.
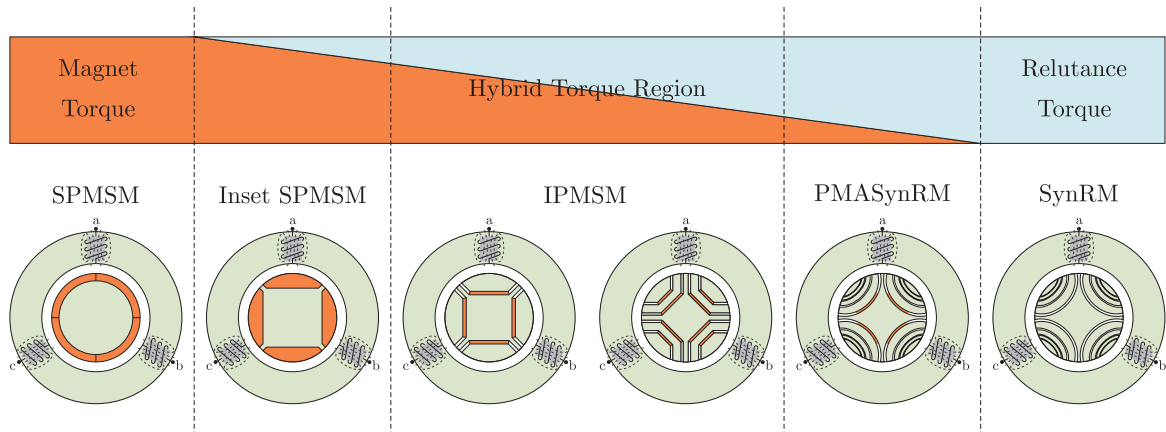
Source: Adapted from (VINH, 2016).

temperature has been pointed out as a major aspect that can cause demagnetization of the magnets (BILGIN et al., 2019).

The low cost and high efficiency features of the three phase voltage source inverters (VSI) made it the main choice for IPMSM drives for low-power applications (REIMERS et al., 2019). A general three phase VSI is illustrate in Fig. 1.5. Higher power density and efficiency, with the addition of improved waveform quality and innate fault-tolerance made multilevel inverters a recent topic o study for EV applications (POORFAKHRAEI; NARIMANI; EMADI, 2021). In high-power applications, multilevel converters are the dominant driving source (PEREZ et al., 2021).

Figure 1.5: Standard voltage source inverter (VSI) topology for IPMSM drives.
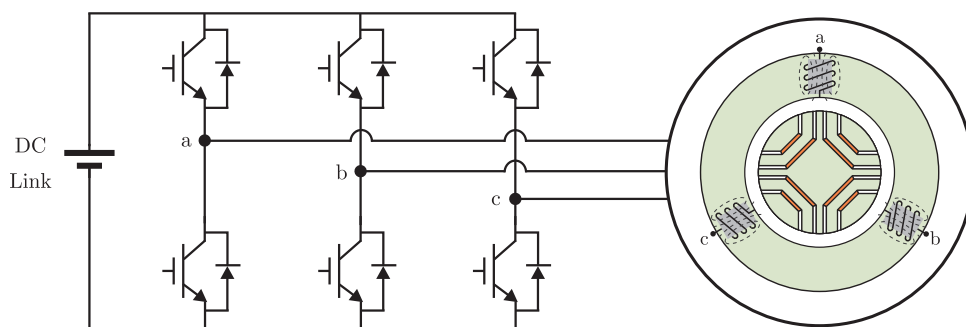
Source: Author.

The IPMSM hybrid torque feature creates the need to adjust the relationship between the currents i_d and i_q. Research efforts sought to minimize the stator current vector module in order to produce the required torque. This strategy is known as maximum torque per ampere (MTPA). A popular closed solution for MTPA implementation considering constant parameters is presented in (MORIMOTO; SANADA; TAKEDA,

1994).

It is established that the solution presented in (MORIMOTO; SANADA; TAKEDA, 1994), which uses constant parameters for its synthesis, has limited results as a result of the saturation of the synchronous inductances. Furthermore, the saturation on the q-axis inductance is more pronounced than d-axis inductance (MEESSEN et al., 2008). Advanced MTPA algorithms seek to track the minimum current vector considering inductance saturation (LI; WANG, 2019; XIA et al., 2020). The overall MTPA trajectory is represented in Fig. 1.6. As demonstrated by the Figure, higher IPMSM speeds reduce the operating region, where MTPA may not be possible. This limitation happens when the maximum available voltage is reached and, in order to increase the IPMSM torque at maximum voltage operation, a deeper flux weakening is required (SEPULCHRE et al., 2018).

Figure 1.6: Representation of the IPMSM maximum torque per ampere trajectory in the synchronous current plane.
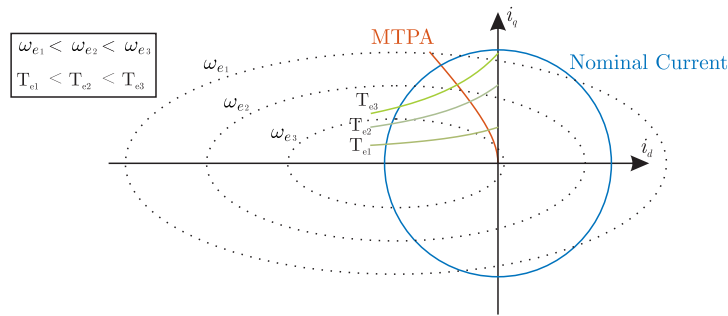
Source: Author.

In addition to current control optimization algorithms, sensorless methods have been studied for the past 30 years in order to eliminate the expensive and bulky mechanical sensors and make the system more compact and robust (PACAS, 2011). The major objectives from this research efforts from both academia and industry were to develop sensorless drives that contain dynamic performance comparable or similar of drives with mechanical sensor.

In this context, due to the importance of removing the mechanical sensor in the electrical drives, this thesis investigates the aspects of rotor speed estimation of IPMSM.

1.3   Thesis Objectives

The specific objectives of this thesis, which aim to improve the performance of sensorless IPMSM drives, are given as follows:

- Develop a straightforward design method for the adaptive full-order observer applied to the estimation of rotor position and speed for high speed sensorless IPMSM drives;

- Investigate the stability constraints of the adaptive full-order observer and adjust the observer design in order to improve the system robustness;

- Perform an analysis on the effects of parameter variation on the position and speed estimation in the adaptive observer;

- Integrate high-frequency signal injection in the adaptive full-order observer for an universal sensorless control algorithm;

- Validation of the proposed algorithms through simulations and experiments.

1.4   Thesis Organization

Chapter 1 presents the thesis motivation and discusses the main characteristics of high performance electric motor drives, such as motor types, control architectures and research topics. Furthermore, IPMSM sensorless control is identified as a important research topic and is the main topic of the thesis. The specific objectives to be achieved at the end of the thesis are also presented.

A deep and comprehensive review of position sensorless PMSM drives is presented in Chapter 2. First, the high-speed sensorless algorithms review is presented. The major observer techniques for high-performance estimation are described. Furthermore, the observer design methods for high performance estimation under non-ideal condition are also investigated. The high-frequency signal injection techniques for low-speed sensorless control are revised. Finally, the methods for full-range sensorless control are investigated.

In Chapter 3, a straightforward design guideline and analysis of the adaptive full-order observer for rotor position and speed estimation of interior permanent magnet synchronous motors (IPMSM) sensorless drives is presented. The adaptive observer is built upon the IPMSM extended electromotive force model in the stationary reference frame. The design of the adaptation and feedback gains is performed by a cascade approach, where state observer and adaptive law operate at distinct frequencies. Since speed estimation error impacts the system stability, this issue is the focus of the high bandwidth state observer design. On the other hand, the adaptive feedback loop, which operates at lower frequencies, ensures good rotor speed estimation performance. The effect of synchronous inductances and stator resistance variation on the estimation of the mechanical variables is investigated and analytically described. Experimental results validate the adaptive observer design method and the parameter variation analysis under sensorless vector control.

In Chapter 4, the adaptive full-order observer is augmented with the recently proposed quadratic extended electromotive force for full-range sensorless PMSM control. The proposed method enables the used of high-frequency signal injection for speed and position estimation under low-speed operation. Furthermore, gain design guidelines for

this approach is presented. Experimental results validate the adaptive observer design method under sensorless vector control.

Chapter 5 presents the final conclusions of the thesis, identifies the contributions and presents the articles published during the PhD.

2 POSITION SENSORLESS PMSM DRIVES LITERATURE REVIEW

Permanent magnet synchronous motors (PMSMs) have been extensively used in modern electrical drives due to their high performance. The higher efficiency and higher power density are the major assets of the PMSM in relation to its main competitor, the induction motor. Furthermore, closed-loop control requires accurate position information of the PMSM. This mechanical information can be extracted through an encoder or a resolver, which is expensive and bulky. Since the disadvantages are unwanted, sensorless control techniques have been a major topic of study (PACAS, 2011; CAPOLINO; CAVAGNINO, 2014). The rotor position estimation techniques are mainly classified into two categories, low-speed methods and high-speed methods. The low-speed sensorless approach depends upon high-frequency signal injection (HFSI) for computation of the position information through the motor reluctance. The high-speed methods are based on the computation of the PMSM flux or electromotive force, which is directly related to the rotor position.

2.1 Observers for High-Speed Sensorless PMSM Drives: Design Methods and Tuning Challenges

The first high-speed sensorless control methods for PMSMs were presented in the 1970s and 80s and were based on open-loop strategies (PLUNKETT; TURNBULL, 1979; IIZUKA et al., 1985; DAVOINE; PERRET; LE-HUY, 1983; WU; SLEMON, 1991). These approaches are sensitive to model mismatches, measurement errors and have poor dynamic behavior. In order to improve the estimation performance from the open-loop algorithms, nonlinear observer techniques began to be investigated in the following decades (SEPE; LANG, 1992; PARK; LEE, 1989; CONSOLI et al., 1994; TOMITA et al., 1998; MATSUI, 1996). Such methods make use of feedback for improvement of the system robustness, which can lead to a better estimation tracking. However, the first publications with these strategies were a direct application of the theoretical methods, which were mainly focused on the observer stability for high-order nonlinear systems. In sensorless applications, fast estimation of the mechanical variables is required to ensure that the closed-loop control will be not significantly affected. Therefore, it is necessary to adjust the design methods of high-order nonlinear observer techniques for the PMSM sensorless application, which requires, in addition to stability, good dynamic estimation performance.

The most advanced estimation techniques require an adequate adjustment of the observer feedback gains. A wide range of studies from the last decade seeks to synthesize the observer gains in closed-form solutions, which can be generalized for all PMSMs.

Figure 2.1: Field oriented PMSM sensorless control diagram.
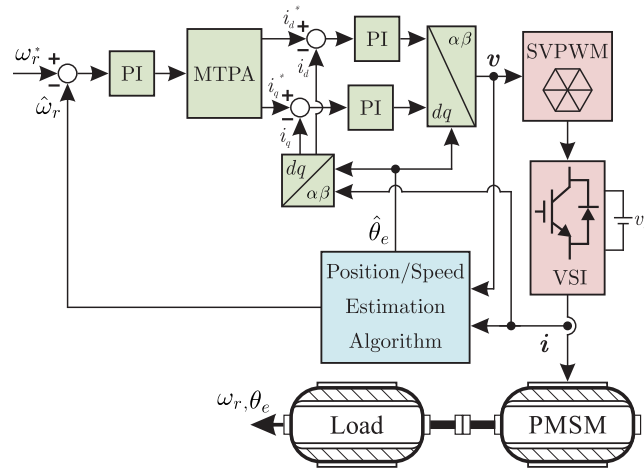
Source: DOI: 10.1109/ACCESS.2021.3072360, ©2021 IEEE.

Another focus of recent research efforts is developing additional observer analysis tools and improving the observer performance under non-ideal conditions. Such topics include the analysis of PMSM parameter variation effects, online parameter estimation, and position observer design against distortions. The study of high speed sensorless applications with low sampling frequencies has also received attention.

This chapter presents a comprehensive review on the design of rotor position estimation methods for high-performance sensorless control of PMSM drives. First, the established observer techniques, their design procedures, and performance specifications are discussed. Then, the effects of parameter variation on the position estimation, parameter estimation algorithms, harmonic and dc error suppression through observer modification, and low sampling frequency to speed ratio observer design are investigated. The main high-frequency signal injection methods are presented. Unification of low and high-speed methods, initial position and polarity estimation are also investigated.

2.1.1   Observer Design For High Performance Position and Speed Estimation

High-performance position and speed estimations are essential for the field-oriented sensorless control, a typical sensorless control diagram is presented in Fig. 2.1. If slow estimation occurs, the closed-loop speed control can become unstable, and the field orientation can be lost. In the case of too high observer bandwidth, the estimation algorithm can amplify the measurement noise, which can lead to deterioration in control performance. Therefore, the design properties are essential in the PMSM sensorless control system performance. In this section, the major PMSM observer design issues, such as models, control techniques, and gain design, are presented.

Model-based estimation algorithms have been the main approach for sensorless

control of PMSM drives in the medium and high-speed range (LIU; CHENG, 1994). The mathematical model of the PMSM is generally defined by the stator current equations in the synchronous frame (KRISHNAN, 2009) and is given by

$$\boldsymbol{v}_{dq} = \boldsymbol{L}_{dq}\rho\boldsymbol{i}_{dq} + R\boldsymbol{i}_{dq} + \boldsymbol{J}\boldsymbol{L}_{dq}\omega_e\boldsymbol{i}_{dq} + \boldsymbol{g}\omega_e\psi, \tag{2.1}$$

where

$\boldsymbol{i}_{dq}$ stator current vector in the synchronous frame,
$\boldsymbol{v}_{dq}$ stator voltage vector in the synchronous frame,
L_d, L_q stator inductances,
R stator resistance,
ω_e, ω_r rotor flux speed and rotor speed,
ψ permanent magnet flux linkage,
ρ differential operator,

$$\boldsymbol{L}_{dq} = \begin{bmatrix} L_d & 0 \\ 0 & L_q \end{bmatrix}, \boldsymbol{g} = \begin{bmatrix} 0 \\ 1 \end{bmatrix}.$$

In the stationary reference frame, the most popular representations of the PMSM dynamics are the linear flux $\boldsymbol{\lambda}$ (HASEGAWA; MATSUI, 2009) and the extended electromotive force (EEMF) $\boldsymbol{e}$ (CHEN et al., 2003). Both modeling approaches create vectors oriented with the PMSM rotor and have an angle equal to the rotor flux position θ_e. Other less popular models are also presented in the literature(BOLDEA; PAICU; ANDREESCU, 2008; ZHAO et al., 2015).

The attractiveness of EEMF and linear flux models are the ability to create linear models where the established control techniques and analysis methods can be easily implemented. The linear flux and EEMF models are represented in the linear form

$$\begin{cases} \frac{d}{dt}\boldsymbol{x} = \boldsymbol{A}\boldsymbol{x} + \boldsymbol{B}\boldsymbol{u} \\ \boldsymbol{y} = \boldsymbol{C}\boldsymbol{x} \end{cases} \tag{2.2}$$

and in Table 1, where $\boldsymbol{v}$ and $\boldsymbol{i}$ are the stator voltage and current vectors in the stator frame, respectively,

$$\boldsymbol{I} = \begin{bmatrix} 1 & 0 \\ 0 & 1 \end{bmatrix}, \boldsymbol{J} = \begin{bmatrix} 0 & -1 \\ 1 & 0 \end{bmatrix}, \boldsymbol{0} = \begin{bmatrix} 0 & 0 \\ 0 & 0 \end{bmatrix}.$$

The EEMF and linear flux accurately represent the behavior of the salient pole PMSM. Furthermore, when $L_q = L_d$, the EEMF, which becomes the standard electromotive force (SONG et al., 2016), and the linear flux (SANGWONGWANICH et al., 2007) models both describe the non-salient pole PMSM. Although it does not present magnets in its rotor, the synchronous reluctance motor can also be represented by such models. In order to simplify the chapter representation, the EEMF is used in equations and figures.

Model	x	A	B	C	u
Linear Flux	$\begin{bmatrix} i \\ \lambda \end{bmatrix}$	$\begin{bmatrix} -I\frac{R}{L_q} & -J\frac{\omega_e}{L_q} \\ 0 & J\omega_e \end{bmatrix}$	$\begin{bmatrix} \frac{I}{L_q} \\ 0 \end{bmatrix}$	$\begin{bmatrix} I & 0 \end{bmatrix}$	v
EEMF	$\begin{bmatrix} i \\ e \end{bmatrix}$	$\begin{bmatrix} -I\frac{R}{L_d} + J\omega_e\frac{L_d-L_q}{L_d} & -\frac{I}{L_d} \\ 0 & J\omega_e \end{bmatrix}$	$\begin{bmatrix} \frac{I}{L_d} \\ 0 \end{bmatrix}$	$\begin{bmatrix} I & 0 \end{bmatrix}$	v

Table 1: PMSM linear models in the stationary frame.

The observability properties of the PMSM model, studied in (VACLAVEK; BLAHA; HERMAN, 2013; KOTEICH et al., 2015; ZALTNI et al., 2009), indicate that position estimation process at low speeds can only be performed using the insertion of high-frequency signals (ZHAO; NALAKATH; EMADI, 2019; FOO; RAHMAN, 2010a; ANDREESCU et al., 2008; Ji-Hoon Jang et al., 2004; KIM; HA; SUL, 2012; LIU; ZHU, 2014a; YANG, 2015; IM; KIM, 2018). In the case of the surface PMSM (SPMSM), even with the insertion of high-frequency components, the position estimation can be a difficult task (JANG et al., 2003). The characteristic of observability deficiency at low speeds of the PMSM can be explained by the difficulty of extracting the EEMF vector angle when its value is null. In the case of the linear flux model, the term $J\omega_e\lambda$ is equal to zero when the rotor is at standstill, making it impossible to observe the rotor flux, and consequently, the position information is unreachable.

Figure 2.2: Main PMSM estimation approaches: (a) Open-Loop (b) Disturbance observer (c) Full-order observer.
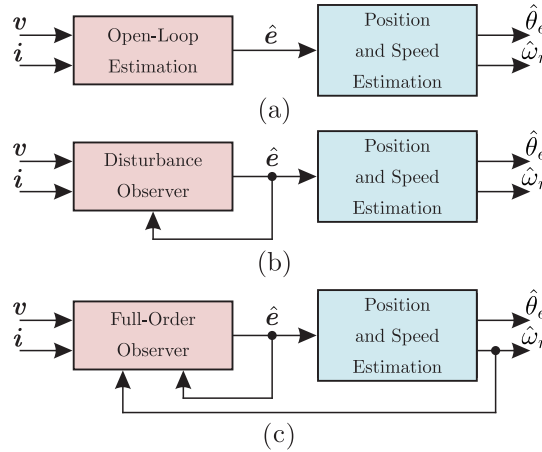
The linear model (2.2) fits the traditional control design problems. Three main estimation methodologies stand out in the literature for the observer design. The first computes the EEMF directly by the PMSM equations. This strategy, known as open-loop estimation, is susceptible to unmodeled dynamics and rapidly fell into disuse. The second most popular strategy is to use an observer with the same order as the plant; that observer

is known as a full-order observer (DAROUACH; ZASADZINSKI; XU, 1994). This method contains the multiplication of the estimated EEMF and speed, which implies high design complexity. The third major estimation method category uses the disturbance observer technique (CHEN et al., 2016) in order to eliminate the full-order observer nonlinearities. Through the disturbance observer, the coupling between the stationary axes disappears since the EEMF, where the coupling takes place, is modeled as a disturbance. These three prevalent strategies are illustrated in Fig. 2.2. Position and speed reconstruction algorithms are required to extract the mechanical variables from the observed EEMF. If the position and speed are observed states from the full-order observer, the reconstruction procedure is not required.

The disturbance observer is developed through the stator current equations of the PMSM model, such as

$$\frac{d}{dt}\hat{\boldsymbol{i}} = \boldsymbol{\rho}_1\left(\boldsymbol{u},\boldsymbol{x},t\right) + \boldsymbol{\sigma} \tag{2.3}$$

where $\boldsymbol{\rho}_1\left(\boldsymbol{u},\boldsymbol{x},t\right)$ is the perturbation term, which is dependent on the PMSM model, and $\boldsymbol{\sigma}$ is the observed disturbance, which estimates the EEMF vector. By selecting the perturbation term $\boldsymbol{\rho}_1\left(\boldsymbol{u},\boldsymbol{x},t\right)$ according to the PMSM model with the exception of the EEMF, the observed disturbance will achieve good tracking of the EEMF if the observed current converges to the actual one.

The main advantage of the disturbance observer estimation strategy is to avoid the nonlinearities of the full-order observer. Thus, the design of the estimator is broken in two simple systems, a disturbance observer and a position and speed reconstruction method.

The simplest topology of the disturbance observer approach is the linear disturbance observer (LDO) (BARATIERI; PINHEIRO, 2014; LU; LIN; HAN, 2016; ZHAO et al., 2018). This strategy design the observed disturbance as a linear feedback variable, enabling the use of classic control tools, such as bode diagram, as an analysis tool. The observed disturbance is defined as

$$\boldsymbol{\sigma} = \boldsymbol{\rho}_2\left(\boldsymbol{u},\boldsymbol{x},t\right)\tilde{\tilde{\boldsymbol{i}}}, \tag{2.4}$$

where $\boldsymbol{\rho}_2\left(\boldsymbol{u},\boldsymbol{x},t\right)$ defines the linear magnitude and frequency responses of the LDO. The block diagram of the LDO method is illustrated in Fig. 2.3.

The main disadvantage of the LDO is the uneven behavior in relation to the frequency of operation, which alters the performance of the estimator significantly in applications with high speed range. Furthermore, the absence of the EEMF dynamics in the perturbation design leads to higher bandwidth requirements for acceptable dynamic performance, which results in noise sensitivity.

The pursuit for proper EEMF tracking through the entire PMSM operating range by the disturbance method culminated in the study of sliding mode observer (SMO)

Figure 2.3: Linear disturbance observer block diagram.
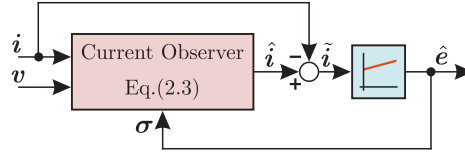
strategies (DING; LI; ZARGARI, 2021; AN et al., 2020a; CHI; ZHANG; XU, 2009; QIAO et al., 2013; ZHAO; QIAO; WU, 2013, 2015; XU et al., 2021). The sliding mode technique uses a high-frequency switching variable in order to ensure robustness to the observation process. The observed sliding mode disturbance is defined as follows:

$$\boldsymbol{\sigma} = k_1 sign\left(\tilde{\boldsymbol{i}}\right), \tag{2.5}$$

where k_1 is the SMO gain. If k_1 is designed high enough, sliding is guaranteed and, therefore, EEMF tracking. The block diagram of the SMO strategy is presented in Fig. 2.4.

The SMO approach is one of the most popular sensorless PMSM control methods. This is due to the easy design of the high-frequency switching variable and straightforward implementation. On the other hand, the resulting observed EEMF by the high-frequency component contains excessive noise, known in the literature as the chattering phenomenon, which makes the direct use of SMO unwanted. Thus, the filtering of the observed high-frequency variable is desired, which reduces the chattering in the observed EEMF.

Figure 2.4: Sliding mode disturbance observer block diagram.
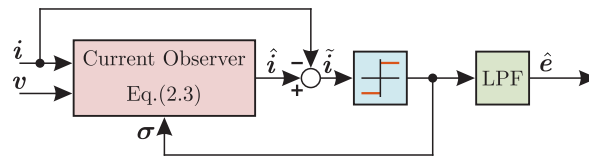
Filtering of the SMO disturbance leads to phase deviation of the observed EMF, thus requiring phase adjustments. In order to avoid this corrections, the replacement of the sign function by the sigmoid function can be performed (KIM; SON; LEE, 2011). This substituting eliminates the chattering phenomenon from the SMO but removes the sliding feature of the algorithm.

In order to avoid the chattering reduction procedure from the standard SMO, the super-twisting sliding mode algorithm, which was developed in (LEVANT; LEVAN-TOVSKY, 1993), was investigated (LIANG; LI; QU, 2017; BARATIERI; PINHEIRO,

2016; R; Singh, 2021; LIANG et al., 2018; WU; ZHANG; CHAI, 2019). The observed disturbance of the super-twisting observer (STO) is defined as

$$\boldsymbol{\sigma} = k_2 \left| \tilde{\boldsymbol{i}} \right|^{\frac{1}{2}} sign\left(\tilde{\boldsymbol{i}} \right) + \int k_3 sign\left(\tilde{\boldsymbol{i}} \right) dt \qquad (2.6)$$

where k_2 and k_3 are the STO gains. The overall structure of the STO method is illustrated in Fig. 2.5.

Figure 2.5: Super-twisting sliding mode disturbance observer block diagram.
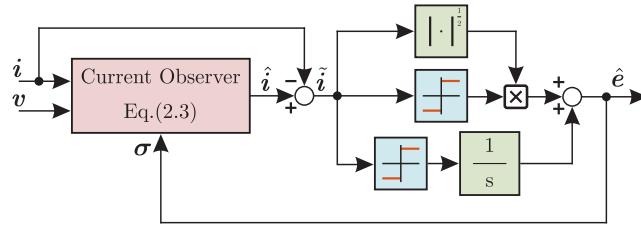
Source: DOI: 10.1109/ACCESS.2021.3072360, ©2021 IEEE.

In the STO strategy, while the standard high-frequency switching variable ensures that the observed EEMF will slide the actual ones, the chattering effect is reduced by the new integral portion part and the error norm. The major drawback of the super-twisting approach is the design of k_2 and k_3 due to the discontinuous dynamics of the system, which are difficult to model and analyze.

The rotor position estimation can be achieved by the full-order observer method, which implements the complete PMSM model with the addition of feedback. In this approach, the EEMF is viewed as a state and not as a disturbance, reducing the high bandwidth requirement in comparison with the LDO. Furthermore, the speed dependent full-order observer poles can be easily extracted, which allows an easy variable gain design for wide speed range applications.

Rotor position and speed estimation can be achieved by the extension of the classical Luenberger observer (BOLOGNANI; CALLIGARO; PETRELLA, 2014). The full-order observer (FOO) is built through the PMSM linear models, given in Table 1, such as follows

$$\begin{cases} \frac{d}{dt}\hat{\boldsymbol{x}} = \hat{\boldsymbol{A}}\hat{\boldsymbol{x}} + \boldsymbol{B}\boldsymbol{u} + \boldsymbol{H}\left(\hat{\boldsymbol{y}} - \boldsymbol{y} \right) \\ \hat{\boldsymbol{y}} = \boldsymbol{C}\hat{\boldsymbol{x}} \end{cases} \qquad (2.7)$$

where $\boldsymbol{H}$ is the feedback gain matrix, $\hat{}$ and $\tilde{}$ express the estimated variables and the error between the estimated variables and the actual variables, respectively.

The good performance of the FOO, required for accurate position tracking, depends on the adjustment of the gain matrix $\boldsymbol{H}$. Such design is performed through the error

dynamics of the FOO, which can be obtained by subtracting (2.2) from (2.7), such as

$$\frac{d}{dt}\tilde{\boldsymbol{x}} = \boldsymbol{A}^{'}\tilde{\boldsymbol{x}} + \boldsymbol{B}^{'}\hat{\boldsymbol{x}}\tilde{\omega}_e \tag{2.8}$$

where $\boldsymbol{A}^{'} = \boldsymbol{A} + \boldsymbol{HC}$ and $\tilde{\omega}_e\boldsymbol{B}^{'} = \tilde{\boldsymbol{A}}$.

The non-linear characteristic of the PMSM model is highlighted in (2.8), where the rotor speed, which is unknown in a sensorless operation, directly impacts the poles of $\boldsymbol{A}^{'}$. Hence, for a fixed $\boldsymbol{H}$, the estimation convergence will be dependent on the PMSM operating point, which will lead the observer to have poor estimation performance and may even cause instability in the sensorless control system. In order to solve this problem, the FOO design methods converge in using the estimated speed in the feedback matrix $\boldsymbol{H}$, which linearizes the estimation behavior of the observer. Through this design configuration, the poles of $\boldsymbol{A}^{'}$ can be adjusted by pole placement, H_{∞} and LMI techniques (HASEGAWA; YOSHIOKA; MATSUI, 2009; HASEGAWA; MATSUI, 2008; TOMITA; HASEGAWA; MATSUI, 2010; NOVAK; NOVAK, 2018; FILHO et al., 2017). These design methods are only ideal when the estimated speed matches the actual one. When speed estimation error occurs, the observer poles diverge from the designed positions, which may lead the system to instability.

The FOO stability conditions are studied in (PO-NGAM; SANGWONGWANICH, 2012), where positive real conditions for arbitrary speed estimation algorithm are obtained by applying the Kalman-Yakubovich Lemma (KYL) to the observer error equations (2.8), such as

$$\begin{cases} \boldsymbol{A}^{'T}\boldsymbol{P} + \boldsymbol{PA}^{'} \leq \boldsymbol{0} \\ \boldsymbol{PB}^{'} = \boldsymbol{C}^T \end{cases} \tag{2.9}$$

where $^{\exists}\boldsymbol{P} = \boldsymbol{P}^T > \boldsymbol{0}$.

The feedback gains derived from the KYL (2.9), which are dependent on the actual rotor speed, stabilize the FOO for arbitrary adaptive speed estimator gains. Furthermore, it is shown in (PO-NGAM; SANGWONGWANICH, 2012) that the local stability is still guaranteed when the estimated speed is used for the implementation of the stabilization gains. Such feedback gain design however, can lead to a poorly damped performance, which can force the control system to instability at sensorless operation, especially under load conditions. The normalized poles of a poorly damped designed FOO is presented in Fig. 2.6 (a). It is highlighted that small speed estimation errors can move the FOO poles to the real axis. Thus, it is shown a pole placement assignment can improve the FOO damping and robustness. The FOO normalized poles with improved pole placement estimation is showed in Fig. 2.6 (b).

The damping design approach can be unintuitive, since the relationship between the FOO gains and the estimation error is not addressed in the stability analysis. In (FILHO; VIEIRA, 2020), a cascade design strategy is presented in order to make the gain

Figure 2.6: FOO normalized poles (a) poorly damped design (b) improved pole placement design.

(a) (b)
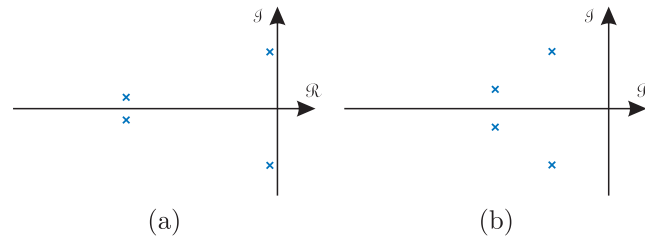
tuning process intuitive. In this design method, the state observer operates at higher frequencies, which demonstrates increasing the observer robustness to speed estimation errors. The adaptive speed estimation law is configured at lower frequencies, thus facilitating the modeling of the FOO gains. The FOO pole behavior under speed estimation error is shown in 2.7 (a). As speed estimation error is increased, the FOO eventually becomes unstable. The effect of increasing the FOO bandwidth on the robustness is illustrated in 2.7 (b). By moving the poles further to the left of the real axis, the effect of speed estimation error is mitigated and the robustness is increased. The cascade design concept, where the state observer is arranged with high bandwidth for expanded robustness, is mainly limited by the sampling frequency.

Figure 2.7: FOO poles with cascade design and (a) lower bandwidth (b) higher bandwidth.

(a) (b)
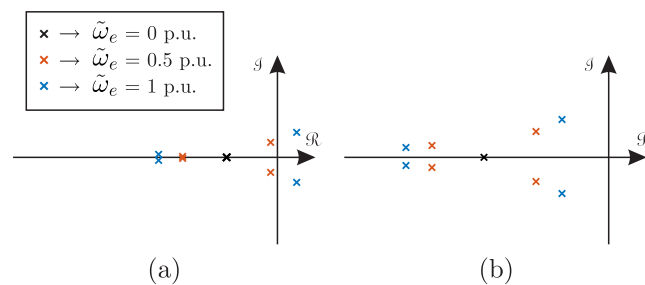
Despite the FOO stability is intrinsically dependent on the PMSM actual speed, the design approaches (PO-NGAM; SANGWONGWANICH, 2012; FILHO; VIEIRA, 2020) ensure robustness to high speed estimation errors. Moreover, the variable feedback gains linearize the estimation behavior in relation to the PMSM speed. It is opposite to the LDO, which has an uneven frequency response, and the SMO, which the chattering is dependent on the operation point.

The FOO can be built in the synchronous rotating frame (PIIPPO; HINKKANEN; LUOMI, 2009; TUOVINEN et al., 2012; HINKKANEN et al., 2012; PIIPPO; HINKKA-

NEN; LUOMI, 2008; KSHIRSAGAR et al., 2012) through the model (2.1), such as

$$\boldsymbol{L}_{dq}\rho\hat{\boldsymbol{i}}_{dq} = \boldsymbol{v}_{dq} - R\hat{\boldsymbol{i}}_{dq} - \boldsymbol{J}\boldsymbol{L}_{dq}\hat{\omega}_e\hat{\boldsymbol{i}}_{dq} - \boldsymbol{g}\hat{\omega}_e\psi + \boldsymbol{H}_{dq}\tilde{\boldsymbol{i}}_{dq} \qquad (2.10)$$

where $\boldsymbol{H}_{dq}$ is the observer feedback gain matrix in the synchronous frame.

In the rotating reference, it is not possible to guarantee that the currents and voltages measured in the synchronous reference are correct, since the estimated position is used in the Park transformations and can lead to a phase error in the observed synchronous variables. Thus, despite the observer having a lower order in the rotating frame, the FOO in the synchronous frame is affected by both the speed and position estimation errors, while the FOO in the stationary frame is only affected by speed estimation error. The FOO vector diagram in the synchronous frame is illustrated in Fig. 2.8. The stability and convergence analysis of the FOO in the rotating frame can be accurately modeled by the linearization of the observer error dynamics as a function of position and speed estimation errors (PIIPPO; HINKKANEN; LUOMI, 2008), which is given by

$$\frac{d}{dt}\begin{bmatrix} \tilde{\boldsymbol{i}}_{dq} \\ \tilde{\theta}_e \end{bmatrix} = \boldsymbol{A}_{dq}\begin{bmatrix} \tilde{\boldsymbol{i}}_{dq} \\ \tilde{\theta}_e \end{bmatrix} + \boldsymbol{B}_{dq}\tilde{\omega}_e \qquad (2.11)$$

where $\boldsymbol{A}_{dq}$ and $\boldsymbol{B}_{dq}$ are the observer error state and input matrices, respectively.

Figure 2.8: Full-order observer vector diagram in the synchronous frame.
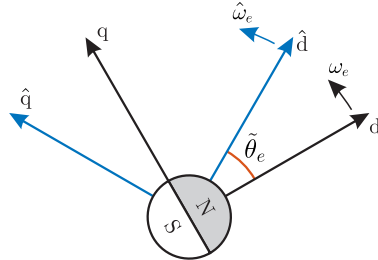
The design of the poles of $\boldsymbol{A}_{dq}$, which is dependent on the actual speed, has similar obstacles as the design of $\boldsymbol{A}'$. Variable speed-dependent feedback gain $\boldsymbol{H}_{dq}$ can improve the estimation performance, and damping enhancement is required. One explicit conclusion from the error equation (2.11) is that, if the observer closed-loop poles are properly designed, good rotor position estimation is accomplished. Therefore, the estimated rotor position can be obtained through the integration of the rotor flux speed, since the estimation structural guarantee the field orientation. In the case of the observer in the stationary frame, the integration of the rotor speed for position estimation can lead to the integration shift phenomenon (LI; LI, 2011).

The equivalence between the FOO in the stationary and synchronous frame is

presented in (PO-NGAM; SANGWONGWANICH, 2012).

The FOO approach presented previously requires a gain design procedure, which are limited to the design conditions previously defined. In contrast with such techniques, the extended Kalman filter (EKF) is a near to optimal estimation algorithm, where feedback gains are recalculated constantly. This characteristic makes it known as the standard of nonlinear systems estimation. The EKF is used in PMSM sensorless applications in (BOLOGNANI; TUBIANA; ZIGLIOTTO, 2003b; WANG et al., 2012; CAO; JIANG; LU, 2020; SMIDL; PEROUTKA, 2012; BOLOGNANI; TUBIANA; ZIGLIOTTO, 2003a; BOLOGNANI; OBOE; ZIGLIOTTO, 1999; FOO; ZHANG; VILATHGAMUWA, 2013). The EKF algorithm is composed by two main steps: Prediction and Correction, which are illustrated in Fig. 2.9 and summarized as follows:

1. **Prediction**: The observed vector $\hat{\boldsymbol{x}}^{ekf} = \begin{bmatrix} \hat{\boldsymbol{i}} & \hat{\theta}_e & \hat{\omega}_e \end{bmatrix}^T$ is computed through the stator currents and voltages similarly to an open-loop method. The covariance matrix $\boldsymbol{P}$ is predicted using the noise covariance matrix $\boldsymbol{Q}$, which needs to be tuned, and the Jacobian matrix of the PMSM model.

2. **Correction**: The near-optimal feedback gain $\boldsymbol{H}^{ekf}$, which is known to produce fast estimation, is computed and used to correct and observe the estimated variables. The measurement noise covariance matrix $\boldsymbol{R}$ is a tuning variable of the feedback gain calculation. Correction of the covariance matrix is also performed. The estimation of the correction EKF step is performed by the following relationship

$$\hat{\boldsymbol{x}}_k^{ekf} = \hat{\boldsymbol{x}}_{k-1}^{ekf} + \boldsymbol{H}^{ekf}\tilde{\boldsymbol{i}} \tag{2.12}$$

Figure 2.9: EKF based estimation structure.
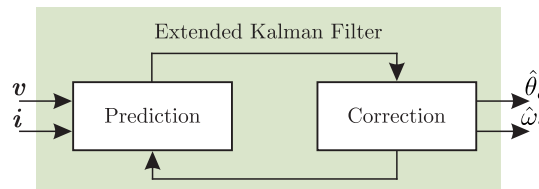
The near to optimal performance of the EKF is not obtained without disadvantages. The calculation of the matrix inversion lead to a significant larger computational cost in comparison with the other estimation methods.

A summarized table of the main characteristics of the major position estimation methods is given in Table 2.

In order to fulfill the estimation algorithm, the PMSM position and speed must be reconstructed from the observed EEMF obtained from the disturbance or full-order observer. The most popular position and speed computation strategies are the derivative approach, the phase-locked loop (PLL) method, and the adaptive algorithm.

Figure 2.10: Speed estimation through derivative method.
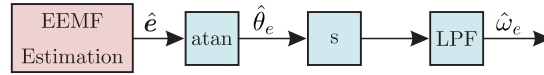
Source: DOI: 10.1109/ACCESS.2021.3072360, ©2021 IEEE.

The derivative approach (LIANG; LI; QU, 2017; BARATIERI; PINHEIRO, 2016; LIANG et al., 2018), which is the most straightforward and is showed in Fig. 2.10, computes the rotor position from the angle of the observed EEMF/flux by a trigonometric function, and the rotor speed is obtained by the derivative of the estimated position. Speed filtering is necessary due to the derivative function.

Figure 2.11: PLL for position and speed reconstruction.
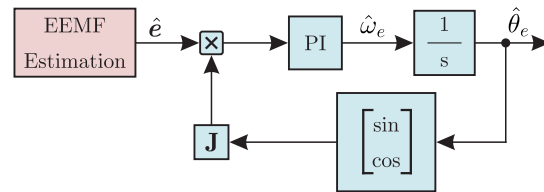
Source: DOI: 10.1109/ACCESS.2021.3072360, ©2021 IEEE.

Position reconstruction can also be performed by the PLL method (WANG et al., 2013; AN et al., 2020a; DING; LI; ZARGARI, 2021), which is illustrated in Fig. 2.11. In this algorithm, the estimated rotor speed is an internal variable. The PLL creates an adjustable vector with variable angle and compares with the observed disturbances. When the error between the vector is small, good position estimation is obtained. The proportional-integral (PI)-type regulator is usually used to converge the observed position, and its design is easy due to the PLL modeling simplicity. Furthermore, the PLL has a broad use in electrical power systems, thus being already well known by many designers.

Another major reconstruction method for the mechanical variables is the adaptive approach (BERNARDES et al., 2014; QIAO et al., 2013), that is demonstrated in Fig. 2.12. This strategy makes use of the gradient descendent algorithm with an adjustable model in order to track the frequency of the observed EEMF. The adaptive method requires design of internal feedback gains for the adjustable model and the gradient descendent adaptive gains. Both feedback and adaptive gains offer additional filtering properties, key features of the adaptive algorithm. The adaptive approach can also be

Position Estimation Category	Observer Method	Convergence Rate	Stability Constraints	Gain Design Complexity	Advantages	Disadvantages
Open Loop Estimation	None	Low	High	None	No tunable parameters	Susceptible to measurement disturbances, slow dynamic response, poor robustness
Disturbance Observer	LDO	Medium	Medium	Low	Simple implementation	Frequency variant performance
	SMO STO	High	Low	Low	Fast convergence and robustness	Chattering problem, complex high-order SMO gain design
Full-Order Observer	Luenberger	High	Medium	Medium	Uniform performance	Stability dependency on the actual rotor speed value
	Extended Kalman Filter	High	Low	High	Anti-measurement noise capability	Computational burden

Table 2: Summary and comparison of the major position estimation methods for sensorless PMSM drives.

Figure 2.12: Adaptive approach for position and speed estimation.
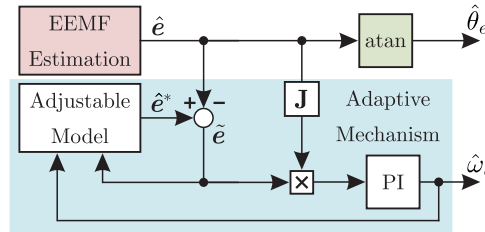
integrated with the FOO (PO-NGAM; SANGWONGWANICH, 2012; FILHO; VIEIRA, 2020), where FOO itself is the adjustable model, making it an adaptive full-order observer.

2.1.2 Observer Design For High Performance Estimation Under Non-Ideal Conditions

In the previous section, the major state observer design strategies for high performance sensorless control are investigated. The analysis and design of these schemes consider an ideal system, where current and voltage measurement inaccuracies, inverter nonlinearities, sampling limitations, and parameter variations are not taken into account. Recent research efforts seek to model such PMSM sensorless control system issues and propose modifications on the observer topologies, which require new design methodologies.

In this section, the main observer research topics for sensorless control under non-ideal conditions, which aim to improve position and speed estimation tracking, are presented.

Modern PMSM sensorless control algorithms are implemented through digital systems. In cases where the sampling frequency f_{samp} is very low in relation to the PMSM rotor flux fundamental frequency f_{ω_e}, the observer design methods presented in the pre-

vious section may have inadequate estimation performance or even may become unstable, making them unsuitable as a sensorless control algorithm.

In (AWAN et al., 2016) a designed method for the FOO in the synchronous frame in the discrete-time domain is proposed. It is demonstrated that the inherently delays in the control system, which can be addressed in discrete-time, affect the observer performance. The proposed design methodology is compared experimentally to the FOO designed in the continuous-time using the forward Euler approximation. The sampling-frequency-to-speed ratio was $f_{ratio} = f_{samp}/f_{\omega_e} = 10$ for the proposed method, which presented good response, and $f_{ratio} = 30$ for the FOO designed in the continuous-time, which became unstable. It is shown that major performance improvements can be obtained by the design in discrete-time. Similar results are obtained in (YANG; CHEN, 2017), where the observer aims to compensate the voltage error caused by delay. The advantages of the discrete-time design over the standard discretized FOO are demonstrated, and a $f_{ratio} = 10$ is achieved experimentally. The importance of delay compensation under low-frequency sampling is demonstrated in (LIANG et al., 2020). When the delay is not compensated, the position estimation error appears as rotor speed increases, with a linear relationship. This estimation error can be almost eliminated by digital delay compensation. Under $f_{ratio} = 10$ experimental results are presented (CHEN et al., 2017; ZHANG et al., 2017; YAO; HUANG; PENG, 2018) with no-load operation and, when shaft load is applied to the PMSM, lower f_{ratio} is achieved. These results suggest that the observer robustness in discrete-time is dependent on the PMSM load. This can be due to parameter error that arises due to inductance saturation at high currents. However, analytical analysis on the observer robustness degradation in discrete-time under load operation is still missing.

The SMO technique applied for low f_{ratio} operation is also studied (AN et al., 2020b; DING et al., 2020). In discrete-time domain, the sliding property of the SMO is not valid, and only quasi-sliding mode observation can be achieved (CORRADINI et al., 2011). Furthermore, under low f_{ratio}, the chattering phenomenon increases, and its reduction is of great importance. In (BERNARDES et al., 2014) the chattering is reduced by two lowpass filters, one internal in the SMO and other at the output of the EEMF observer. Phase compensation due to the filtering process is required. Bandpass filter can also be employed in order to reduce the SMO chattering. This strategy does not require phase compensation since the bandpass filter is a zero phase-shift amplifier (AN et al., 2020b).

The discretization method is crucial in order to achieve high performance low f_{ratio} estimation. The FOO observer poles with exact discretization (zero-order-hold), Euler and Tustin approximations are compared in (ZHANG et al., 2017) and are illustrated in Fig. 2.13. As the PMSM rotor speed increases, the observer poles move further to the left plane of the real axis. When the Euler approximation is employed, the estimation

becomes highly oscillatory at high speeds. The Tustin approximation does not exhibit oscillatory behavior of the Euler method but suffers from degradation in performance compared to the exact discretization.

Figure 2.13: Discrete-time poles as bandwidth increase with different discretization methods.
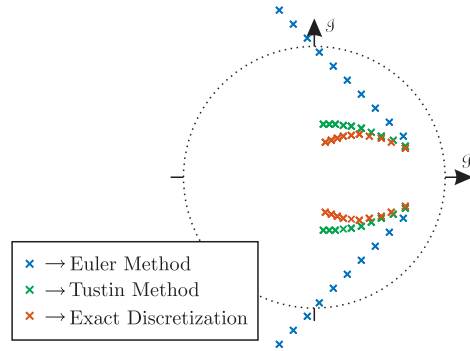
Source: DOI: 10.1109/ACCESS.2021.3072360, ©2021 IEEE.

The implementation of the high-performance PMSM position observers requires the knowledge of the motor parameters, which are the stator resistance, stator inductance, and magnetic flux linkage. The high-speed methods are more dependent on parameters errors (XIAO et al., 2021), where HFSI methods are independent on parameters. The sensorless algorithm sensitivity for parameter error can be analysed in model based methods (BOLOGNANI; CALLIGARO; PETRELLA, 2014; BOLOGNANI et al., 2018; KIM; SON; LEE, 2011; HINKKANEN et al., 2012). Magnetic flux linkage and d-axis stator inductance present no impact on the rotor position estimation. The q-axis inductance is the parameter which has the most influence on rotor position estimation and its effects are increased with the motor load. The stator resistance causes less influence on position estimation and its effects increases with load and decreases with speed.

In order to achieve accurate position estimation, the observer q-axis and stator resistance should match the PMSM. Despite flux linkage and d-axis inductance error do not impact rotor position estimation, they are both required in the current controllers design. Although nominal parameters are given by manufacturers, temperature and load conditions can cause changes in the parameters (RAFAQ; JUNG, 2020). (WANG et al., 2019). One way to mitigate the impact of q-axis inductance variation is to perform offline estimation and implement a lookup table (WANG et al., 2019). However, this process is hard to generalize for a large range of motors. Therefore, parameter estimation based adaptive observers have been proposed in order to perform online estimation of the PMSM parameters. The diagram of a standard parameter estimation based adaptive observer is presented in Fig. 2.14.

Adaptive algorithms are an extensively used approach for parameter estimation in

Figure 2.14: Parameter estimation based adaptive observer diagram.
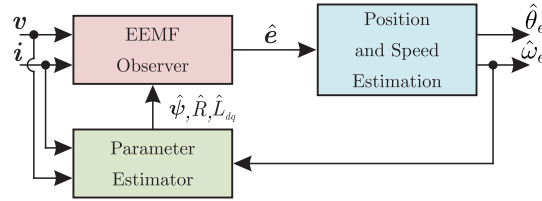
Source: Author.

the control systems literature. More specifically for PMSMs, adaptive filters were extensively studied for improvements in the control and estimation algorithms (ICHIKAWA et al., 2006a; INOUE et al., 2011, 2009; RAFAQ et al., 2017; SHI et al., 2012; AUGER et al., 2013; ZHU et al., 2007). The gradient descendent and the recursive least square (RLS) methods are the most common adaptive schemes. The gradient descendent performance is highly dependent on the adjustment of the adaptation gains, which can be hard to design when all parameters are estimated simultaneously. The RLS approach does not require de design of the adaptive gain, since it is embedded in the covariance matrix. However, the reset of the covariance matrix can be hard to systematize for a large range of motors. Furthermore, multi-parameter estimation through the RLS algorithm can be computationally costly due to the high-order covariance matrices.

The parameter estimation based on adaptive algorithms have been attached to state observers for improvements in the PMSM sensorless parameter estimation control (NAHID-MOBARAKEH; MEIBODY-TABAR; SARGOS, 2004; RASHED et al., 2007; KIVANC; OZTURK, 2018; KIM; SON; LEE, 2011; YE; YAO, 2020; LIANG; LI; QU, 2017; LEE; LEE, 2013; PIIPPO; HINKKANEN; LUOMI, 2009; HINKKANEN et al., 2012; YAO et al., 2020; HASEGAWA; MATSUI, 2009). Such approach uses the observer current error for estimation of the PMSM rotor position, speed and parameters. Due to the large number of estimated variables, a faster rotor variables estimation frequency is desired, so that the parameter estimation does not affect the dynamics of the sensorless control. Parameter estimation is performed at a lower frequency in order to reduce the effects of parameter error on steady-state position estimation.

As a form of achieve higher performance dynamic parameter estimation, HFSI has been is studied for PMSM parameter estimation (WU; ZHAO; SUN, 2020; NALAKATH; PREINDL; EMADI, 2017). It is demonstrated that some parameter combinations for estimation can present observability problems at steady-state without HFSI (NALAKATH; PREINDL; EMADI, 2017). In addition to ensuring parameter observability, the parameter estimation dynamics can be performed with better dynamics in comparison with the conventional adaptive algorithms. As a major drawback, HFSI causes large torque ripples and increases power loses.

Parameter Estimation Method	Advantage	Disadvantage
Gradient Descendent/RLS	Simple implementation	Complex gain design
HFSI	Fast Convergence	Additional noise due to signal injection

Table 3: Summary and comparison of the parameter estimation methods.

The major PMSM online estimation techniques are summarized in Table 3.

Recent research efforts have been made developing frequency adaptive observers for improving the estimation performance under distorted conditions. The observers presented in the previous section present a low-pass behavior (KIM; SON; LEE, 2011; WANG; YANG; XU, 2013; GONG et al., 2020; FOO; RAHMAN, 2010b; QIAO et al., 2013; YANG; CHEN, 2017; YANG; HSU, 2017; XIAO et al., 2021; ZHU et al., 2001; SOLSONA; VALLA; MURAVCHIK, 2000, 1996; QU; QIAO; QU, 2020; HEJNY; LORENZ, 2011; XIAO et al., 2020a). Such methods attenuate the high-frequency measurement current noises but not mitigate the dc- offset phenomenon (XIAO et al., 2020a; XU et al., 2018; JIANG et al., 2019; LU et al., 2020; CHOI et al., 2017) or the inverter nonlinearity effect (BOLOGNANI; CALLIGARO; PETRELLA, 2014). The effects dc-offset in the position estimation is given by

$$
\begin{cases}
\hat{\boldsymbol{e}} = \boldsymbol{e} + \boldsymbol{d}_{dc} \\
\tilde{\theta}_e = M_{dc}\sin(\omega_e t + \varphi_{dc})
\end{cases}
\tag{2.13}
$$

where $\boldsymbol{d}_{dc}$ is the disturbance caused by dc-offtset in the EEMF, and M_{dc} and φ_{dc} are the magnitude and phase of position error caused by the dc-offset, respectively. The dc-offset error can lead open-loop estimation strategies to instability (XU et al., 2018; XIAO et al., 2020a).

The inverter nonlinearity is the primary source of the odd harmonics in the EEMF estimation (WANG et al., 2014; KIM et al., 2016; HUTTERER et al., 2009; WANG et al., 2020) and impact the estimated position in the following manner

$$
\begin{cases}
\hat{\boldsymbol{e}} = \boldsymbol{e} + \boldsymbol{d}_{-5\text{th}} + \boldsymbol{d}_{7\text{th}} \\
\tilde{\theta}_e = M_{6\text{th}}\sin(6\omega_e t + \varphi_{6\text{th}})
\end{cases}
\tag{2.14}
$$

where $\boldsymbol{d}_{-5th}$ and $\boldsymbol{d}_{7th}$ are the dominant odd-order harmonics, and M_{6th} and φ_{6th} are the magnitude and phase of the position error caused by the odd harmonics. As shown by (2.14), the negative fifth and seventh have the major impact on the position estimation, where the third harmonic is canceled by y-connected motor.

Even-order harmonics have been less studied in sensorless PMSM drives. This harmonics are generated by the space-vector PWM (SVPWM) (WU, 2005). The dominant even-order harmonics are the second and fourth components, which impact the estimated

Figure 2.15: Adaptive bandpass observer block diagram.
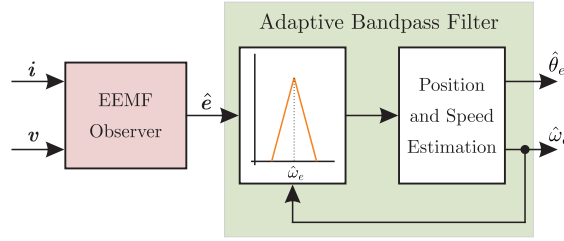
Source: Author.

rotor speed in the following form

$$
\begin{cases}
\hat{\boldsymbol{e}} = \boldsymbol{e} + \boldsymbol{d}_{-2\text{th}} + \boldsymbol{d}_{4\text{th}} \\
\tilde{\theta}_e = M_{3\text{th}} \sin(3\omega_e t + \varphi_{3\text{th}})
\end{cases},
\tag{2.15}
$$

where $\boldsymbol{d}_{-2th}$ and $\boldsymbol{d}_{4th}$ are the dominant even-order harmonics, and M_{3th} and φ_{3th} are the magnitude and phase of the position error caused by the even harmonics.

Adaptive bandpass position observers were developed in order to reduce the distortions on the position estimation (XIAO et al., 2020a; XU et al., 2018; JIANG et al., 2019; JIANG; XU; MU, 2017; ZHAO et al., 2018; CHEN et al., 2019; JI et al., 2020; SONG et al., 2016; WANG; XU; ZOU, 2019; BAO et al., 2018; AN et al., 2020b; ZHAO et al., 2018; BAO et al., 2018; AN et al., 2020b).

The standard behavior of the adaptive bandpass observer is given by

$$
G_{bp}(s) = \frac{k_4 \hat{\omega}_e s}{s^2 + k_4 \hat{\omega}_e s + \hat{\omega}_e^2}
\tag{2.16}
$$

where k_4 is the observer gain. The overall structure of the adaptive bandpass observer is illustrated in Fig. 2.15 and the frequency response is presented Fig. 2.16. Such response reduces the low-order harmonics and dc-offset. Second order generalized integrator (SOGI) based adaptive bandpass observers (JIANG; XU; MU, 2017; XU et al., 2018; JIANG et al., 2019; CHEN et al., 2019; JI et al., 2020; SONG et al., 2016; WANG; XU; ZOU, 2019) are also studied in order to eliminate the dc-offset distortion.

Adaptive bandpass observers are techniques adapted from methods used in grid-connected converters (GOLESTAN; GUERRERO; GHAREHPETIAN, 2016; GOLESTAN et al., 2019, 2017, 2018; GUDE; CHU; VEDULA, 2019; RAMEZANI et al., 2018). For sensorless PMSM drives, stability of the adaptive bandpass observer (XIAO et al., 2020a; GOLESTAN et al., 2017) can be a challenge since the estimated rotor speed, which is used for changes in the observer frequency response, can operate in a large range.

Adaptive multiple harmonic elimination (MHE) observers are an option for elimination of the low-order harmonics (WANG et al., 2014; ZHANG et al., 2016a, 2016b;

Figure 2.16: Adaptive bandpass observer bode diagram.
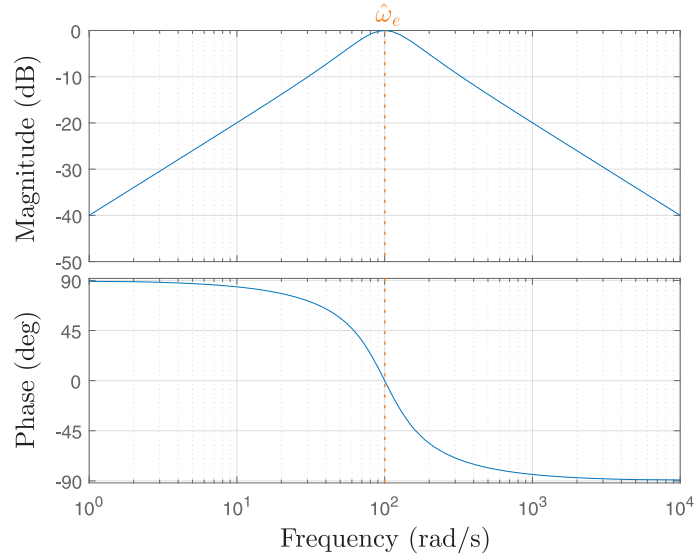
Source: Author.

WANG et al., 2014, 2014; WU et al., 2020; XIAO et al., 2020b; WANG; XU; ZOU, 2020; GUDE; CHU; VEDULA, 2019; TEDESCO; CASAVOLA; FEDELE, 2017). The adaptive MHE observer is usually implemented as a combination of multiple bandpass observer, which have the following frequency response

$$G_{MHE}(s) = G_1 \frac{1 - G_5 - G_7 + G_5 G_7}{1 - G_5 G_7 - G_1 G_5 - G_1 G_7 + 2 G_1 G_5 G_7} \tag{2.17}$$

where G_1, G_5 and G_7 are the adaptive bandpass observers with central frequency of $\hat{\omega}_e$, $5\hat{\omega}_e$ and $7\hat{\omega}_e$, respectively. The block diagram of the adaptive MHE observer is presented in Fig. 2.17 and the bode diagram in Fig. 2.18.

Figure 2.17: Adaptive MHE observer block diagram.
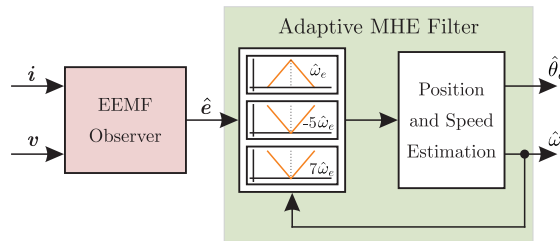
Source: Author.

The adjustment of the multiple gains of the MHE observer can be a hard task. Therefore, learning MHE observers (WANG et al., 2014, 2014; ZHANG et al., 2016a) have been presented as solution. This strategy uses the observer EEMF to learn the amplitude of the main low-order harmonics and compensate its impacts on the position estimation.

Figure 2.18: Adaptive MHE observer bode diagram.
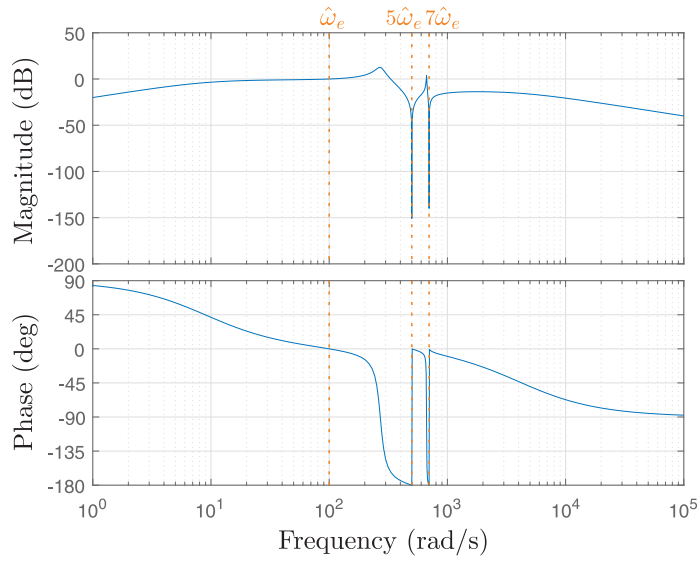
The block diagram of the adaptive learning MHE observer is presented in Fig. 2.19.

Figure 2.19: Diagram of the learning based MHE observer.
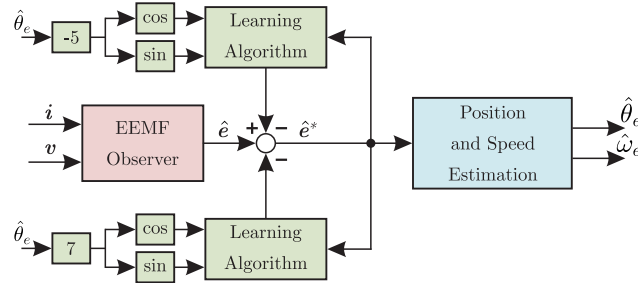
The dc-Offset and low-order harmonic suppression features of the major frequency-adaptive observer are summarized in Table 4.

2.2 High frequency Signal Injection for Low-Speed Sensorless IPMSM Drives

The limitations of EMF and flux based position estimation under low-speed operation, which are based on the PMSM fundamental, are established in the literature (WANG; VALLA; SOLSONA, 2020). This is mainly due to the fact that both variables have their amplitude directly related to the PMSM speed. High-frequency signal injection became the major solution in order to avoid the PMSM observability issues under

Frequency Adaptive Observer	dc-Offset	Low-Order Harmonics
Second-Order Bandpass Filter	Reduced	Reduced
SOGI	Eliminated	Reduced
Multiple Adaptive Bandpass Filter	Eliminated	Eliminated odd harmonics
Learning Algorithm	Unchanged	Eliminated odd harmonics

Table 4: Summary and comparison of the frequency adaptive observer methods.

low-speed. Such strategy utilizes the magnetic anisotropy of IPMSM, and therefore, can not be used in SPMSM.

The first works that employ the high frequency signal injection tool for low-speed sensorless IPMSM can be traced from the late 90s (CORLEY; LORENZ, 1998; MIZU-TANI; TAKESHITA; MATSUI, 1998). In the last two decades algorithm improvements were investigated in the literature. Such studies examine the types of signal injection waveform approaches, the differences between synchronous and stationary frame signal injection and effects of parameter variation.

Other approaches use high frequency injection indirectly and are known in the literature as fundamental pulse-width modulation (PWM) excitation (FPE) based methods. These strategies still perform a high-frequency current in the IPMSM, but have a simpler implementation.

Initial Position and Polarity Estimation is also a major concern for the sensorless control initiation and some low-speed sensorless algorithms are unable to obtain such information. Therefore, this characteristics must be investigated for the applied method and, if the algorithm is unable to obtain the initial position, an additional algorithm must be used together to perform this function.

2.2.1 Rotating Signal Injection

The standard rotating signal injection strategy is illustrated in Fig. 2.20. This strategy is characterized by injecting the high-frequency signal in the stationary frame, making the signal processing to be phase-modulated (KIM et al., 2016; GABRIEL et al., 2013; ALMARHOON; ZHU; XU, 2017). Furthermore, the position estimation through rotating injection is more sensitive from the inverter nonlinear effect. The HF injection in the stationary frame has as major advantage not requiring the IPMSM initial position information.

2.2.2 Pulsating Signal Injection

The standard pulsating signal injection strategy is demonstrated in Fig. 2.21. This magnitude modulated scheme is defined by the injection of the HF signal in the

Figure 2.20: Block diagram of a rotating/stationary signal injection method.
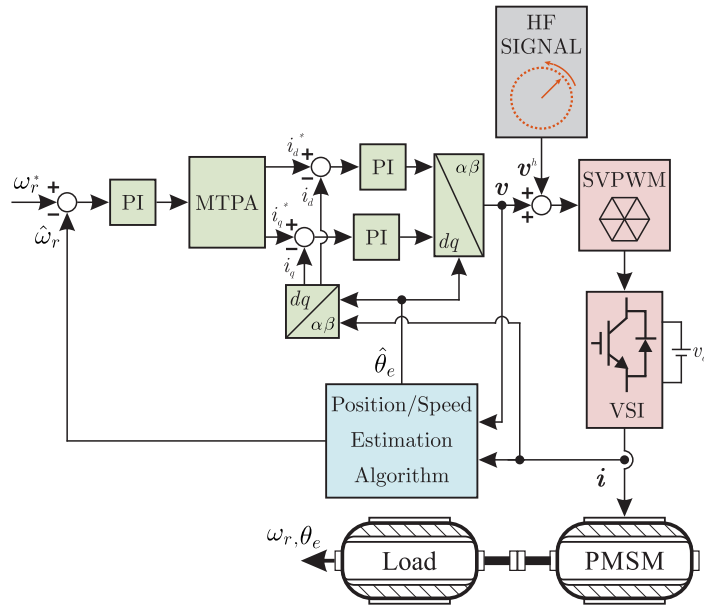
Source: Author.

synchronous frame (ZHANG et al., 2018, 2019; LIU; ZHU, 2014b; WANG et al., 2017). The signal injection in the synchronous frame is reported to have better robustness in relation to the inverter nonlinear effect (RACA et al., 2008). As major disadvantage of the pulsating method, is the IPMSM initial position information requirement. The HF signal injection in the pulsating approach is usually performed in the d-axis in order to reduce torque ripple and improve the closed-loop sensorless control algorithm.

A summarized table of some critical features of the HF signal injection schemes is provided in Table 5.

2.2.3 Other Methods

Fundamental pulse-width modulation excitation (FPE) algorithms are a less popular alternative to the high-frequency injection methods. The FPE strategy was developed in order to avoid the observer design and facilitate the implementation.

The FPE methods are mainly divided in the indirect flux detection by on-line reactance measurement (SCHROEDL, 1996), the zero sequence current derivatives measurements method (STAINES et al., 2006; STAINES; ASHER; SUMNER, 2006) and zero voltage vector injection method (WANG et al., 2018; XIE et al., 2015). All these approaches are based on inserting voltages vectors between the PWM control commands. In this way, the rotor position can be detected and reconstructed, and such technique can be expanded for other AC motors.

Figure 2.21: Block diagram of a pulsating/synchronous signal injection method.
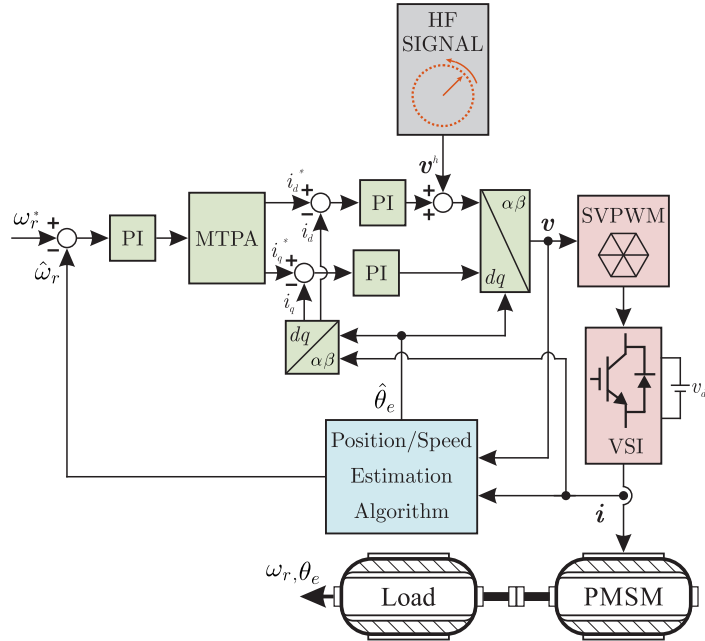
Source: Author.

Injection Method	Reference Frame	Modulation Type	Initial Position Information	Inverter Nonlinear Effect
Rotating Signal Injection	$\alpha\beta$	Phase	Not required	High
Pulsating Signal Injection	dq	Magnitude	Required	Low

Table 5: Summary and comparison of the HF signal injection schemes.

2.2.4 Initial Position and Polarity Estimation

Some of the low-speed position estimation methods are not capable of detecting the initial polarity at start-up. In order to solve this issue, algorithms have been proposed in the literature (NAKASHIMA; INAGAKI; MIKI, 2000; KIM et al., 2004; MURAKAMI et al., 2012). These methods are based on the nonlinear magnetization aspects of the IPMSM.

2.3 Full-range Sensorless IPMSM Drives

As presented the the previous sections, the signal injection based methods presents high performance at low-speeds, but there are drawbacks of the injected signal approach if used at medium to high-speed range, such as torque ripple, acoustic noise and lower efficiency. Therefore, in order to achieve high sensorless control performance for the full speed range, fundamental EMF based methods must be combined with the injection based

algorithms. Consequently, research efforts turned into combining the distinct approaches presented in the previously sections.

The integration of the high and low-speed methods are primarily performed by a blending function or an unified full-range observer.

2.3.1   Blending Function

Switching between the low and high-speed algorithms can cause transient performance issues, which can lead to system instability. In order to perform a smooth speed transition, the estimated rotor position must be blended for accurate full-speed sensorless control. A common blending function for incorporate both low and high-speed methods (LARA; CHANDRA; XU, 2012; SEILMEIER; PIEPENBREIER, 2015) is given by

$$\hat{\theta}_e^{full} = f\left(\hat{\omega}_e\right)\hat{\theta}_e^{low} + \left[1 - f\left(\hat{\omega}_e\right)\right]\hat{\theta}_e^{high} \tag{2.18}$$

where $f\left(\hat{\omega}_e\right)$ is the blending function, which is illustrate in Fig. 2.22. This type of method avoid sudden and repetitive changes between algorithms. Furthermore, instead of a fixed speed for method transition, a speed band is used with a lower speed ω_e^{lower} and an upper speed ω_e^{upper}.

The blending function has as the major drawback the requirement of design two observers, doubling the design process effort.

Figure 2.22: Block diagram of full-range estimation based on the blending function.
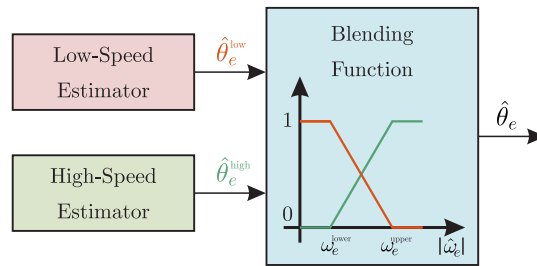
Source: Author.

2.3.2   Unified Full-Ranged Speed Estimation

In order to avoid the design of two observers, unified full-range sensorless schemes have been proposed. Such methods provide a versatile and straightforward implementation approach.

The adaptive observer for high-speed sensorless IPMSM using the synchronous model is analysed in (PIIPPO; LUOMI, 2005; PIIPPO; HINKKANEN; LUOMI, 2008). A high-frequency signal injection is coupled to the adaptive observer in order to achieve

full-range speed estimation. In this way, low-speed estimation can be performed with the same observer used for high-speed estimation. Furthermore, the gains design properties of the high-speed observer remains the same at low-speed operation. Therefore, the overall estimation structure is simplified in relation to the blending function approach. This overall full-range estimation structure is illustrated in Fig. 2.23.

Figure 2.23: Block diagram of the adaptive observer method with the augmentation with HF signal injection.
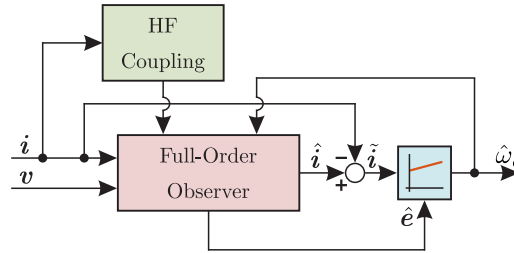
Source: Author.

Another unified estimation approach can be made at the stationary frame. This strategy is possible due to the EEMF contains the i_q current derivative in its model dynamics. This phenomenon enables to avoid the zero speed null EEMF value and, therefore, achieving low-speed estimation through the high-speed based EEMF observers. However, the high-frequency signal create a pulsating EEMF response, which makes it difficult to directly implement the high-speed algorithms. Thus, new quadratic EMF (QEMF) variables are proposed in(XIAO et al., 2020) in order to perform the demodulation of the high-frequency signal EEMF and extract the envelope of the EEMF response.

The overall diagram of the QEMF based demodulation process trough EEMF estimation is presented in Fig. 2.24. This strategy encompasses all types of signal injections, since the demodulation process is carried out by the normalization process of the QEMF vectors.

Figure 2.24: Block diagram of the QEMF based demodulation strategy for full-speed sensorless control.

Source: Author.

2.4 Chapter Conclusion

The PMSM sensorless methods have been widely used due to its cost and volume reduction capabilities, which leads to a vast research in order to achieve similar perfor-

mance from the drives with sensor. A comprehensive review of observer methods for position sensorless PMSM drives, as well with the major tuning challenges are presented in this chapter.

More specifically, the major high-speed estimation approaches are investigated, which are the open-loop estimation, disturbance observer and full-order observer. The open-loop strategy lacks the robustness that is essential for real applications. Disturbance observers can remove some nonlinearities from the estimation design, simplifying the design process. The full-order observer offers a better understanding of the complete system. The design and stability constraints of the specific observer methods are commented. Then, the dominant recent research topics are presented. Low-sampling frequency observer design offers the possibility of operation at high speeds with low sampling frequency. Online parameter estimation removes the parameter error effects on position estimation. Frequency-adaptive observers for reduction of the harmonic content caused by the inverter nonlinear effects are also investigated.

Finally, a review of high-frequency signal injections techniques for low-speed sensorless control and unified full-ranged speed estimation are presented. The injection can be performed in the synchronous frame, reducing the effects of the inverter nonlinearities, or in the stationary frame, which does not require initial position information. The initial position and polarity estimation is executed using the nonlinear magnetization aspects of the IPMSM. The low and high-speed methods are unified through the blending function or universal sensorless methods.

3 ADAPTIVE FULL-ORDER OBSERVER ANALYSIS AND DESIGN FOR SENSORLESS IPMSM DRIVES

The first high-speed methods for rotor position and speed estimation of synchronous machines were presented for the surface permanent magnet synchronous motor (SPMSM) (TOMITA et al., 1998; BOLOGNANI; OBOE; ZIGLIOTTO, 1999; MATSUI, 1996). These methods seek to compute the electromotive force (EMF), where the rotor position information is contained, through the SPMSM electrical circuit model. The main concern of these first studies was the stability conditions of the estimation method under constant rotor speed. However, the algorithm stability does not guarantee the desire high performance sensorless control, as a stable but slow estimation can lead to problems with the speed closed-loop control. In recent years, design solutions were proposed aiming to obtain good dynamical estimation of the mechanical variables (LIANG et al., 2018; PARK; SUL, 2014; WANG et al., 2012; HINKKANEN et al., 2018; PO-NGAM; SANGWONGWANICH, 2012; KSHIRSAGAR et al., 2012; AWAN et al., 2016).

In order to apply the consolidated high-speed SPMSM adaptive observer methods to the IPMSM, the model of this machine is required. The main IPMSM models are the active flux concept (BOLDEA; PAICU; ANDREESCU, 2008) and the extended EMF (EEMF)(CHEN et al., 2003). The active flux concept uses the flux which generates torque in order to model the IPMSM. Through this approach, the active flux is obtained by the integration of the stator equivalent IPMSM circuit. This approach is susceptible to integration dc-offset and parametric error, and therefore an additional variable is required for proper active flux estimation (BOLDEA; PAICU; ANDREESCU, 2008). The EEMF model has similar characteristics to the traditional EMF model, but presents an additional coupling in the stator current dynamics and the IPMSM reluctance appears in the EEMF equations. Disturbance observers have been used to avoid some of these model nonlinearities and obtain the extended EMF (ZHAO; QIAO; WU, 2014, 2013). In this approach, the EEMF is estimated first by the disturbance observer and, then, the rotor position is extracted from the EEMF by means of an adaptive observer. In (PIIPPO; HINKKANEN; LUOMI, 2008; YUAN et al., 2013) rotor speed estimation is performed in the synchronous reference frame, with the disadvantage of being more sensitive to parametric variations. Alternative methods to observers are also presented in the literature (BUI et al., 2019; TANG et al., 2020).

Despite the efforts to develop algorithms for IPMSM rotor speed estimation, analytical impact of parameter variation on the adaptive observer rotor speed and position estimations remain to be solved. A straightforward design method for the adaptation and feedback gains of the adaptive full-order observer is also a challenge, since it is necessary to adjust multiple gains in order to estimate the rotor speed properly in transients.

Furthermore, observer stability is dependent on the value of the rotor speed, which is unknown, and therefore must be taken into account in the system analysis (PO-NGAM; SANGWONGWANICH, 2012).

The motivation of this chapter is to develop and apply the adaptive observer estimation concepts previously presented to the SPMSM for the IPMSM. The main contributions of this chapter can be summarized as follows:

- Design guidelines for the adaptation and feedback gains based on a cascade strategy are presented. The proposed framework enables to explore the state observer design aiming robustness improvements and achieve good rotor speed estimation damping without the commonly used proportional gain of the adaptation law. This feature reduces stator current noise amplification on the rotor speed estimation.

- The analytical formulation of the effects of parameter variation on the estimation of both rotor speed and position presented in (PO-NGAM; SANGWONGWANICH, 2012) for the SPMSM are expanded for the IPMSM. Through this investigation, is quantified the impact of each parameter error in the rotor speed regulation and in the maximum torque per ampere algorithm.

Experimental results under sensorless control operation are provided in order to validate the proposed adaptive observer design and analytical contributions.

3.1   IPMSM Linear Model

The dynamical model of the IPMSM stator currents in the synchronous reference dq is well known in the literature (KRISHNAN, 2009) and is given by

$$
\begin{bmatrix} v_d \\ v_q \end{bmatrix} = \begin{bmatrix} R + \rho L_d & -\omega_e L_q \\ \omega_e L_d & R + \rho L_q \end{bmatrix} \begin{bmatrix} i_d \\ i_q \end{bmatrix} + \begin{bmatrix} 0 \\ \omega_e \psi \end{bmatrix}, \tag{3.1}
$$

where R is the stator resistance, L_d and L_q are the inductances of the d and q axes, respectively, ρ is the differential operator, ψ is the permanent magnet flux linkage and ω_e is the rotor flux speed. The mechanical speed ω_r is given by dividing ω_e by the number of pole pairs n_p and i_d, i_q, v_d, v_q are the stator currents and voltages in the synchronous reference frame, respectively.

Direct transformation of (3.1) to the stationary coordinates is undesired due to the asymmetrical form of the impedance matrix. Thus, the IPMSM model in synchronous reference frame (3.1) is rewritten symmetrically as

$$
\begin{bmatrix} v_d \\ v_q \end{bmatrix} = \begin{bmatrix} R + \rho L_d & -\omega_e L_q \\ \omega_e L_q & R + \rho L_d \end{bmatrix} \begin{bmatrix} i_d \\ i_q \end{bmatrix} + \begin{bmatrix} 0 \\ (L_d - L_q)\left(\omega_e i_d - \dot{i}_q\right) + \omega_e \psi \end{bmatrix}. \tag{3.2}
$$

By applying the inverse Park transform in (3.2), the stationary circuit model of the IPMSM is obtained as

$$\boldsymbol{v} = [(R + \rho L_d)\,\boldsymbol{I} + (L_d - L_q)\,\omega_e \boldsymbol{J}]\,\boldsymbol{i} + \boldsymbol{e}, \tag{3.3}$$

where

$$\boldsymbol{e} = \left\{ (L_d - L_q)\left(\omega_e i_d - \rho i_q\right) + \omega_e \psi \right\} \begin{bmatrix} -\sin\theta_e \\ \cos\theta_e \end{bmatrix}, \tag{3.4}$$

and θ_e is the rotor flux position.

The vector $\boldsymbol{e}$ is the extended electromotive force (EEMF) (CHEN et al., 2003) and contains the information of the IPMSM rotor position.

The IPMSM behavior can be modeled by a state space equation in the stationary reference frame. In this model, the input are the stator voltages $\boldsymbol{v} = \begin{bmatrix} v_\alpha & v_\beta \end{bmatrix}^T$, the states variables are the stator currents $\boldsymbol{i} = \begin{bmatrix} i_\alpha & i_\beta \end{bmatrix}^T$ and the EEMF $\boldsymbol{e} = \begin{bmatrix} e_\alpha & e_\beta \end{bmatrix}^T$. Assuming constant rotor speed and constant shaft load, it is obtained that $\dot{i}_d = \dot{i}_q = \dot{\omega}_e = 0$. Through this consideration, the IPMSM linear model takes form as

$$\frac{d}{dt}\begin{bmatrix} \boldsymbol{i} \\ \boldsymbol{e} \end{bmatrix} = \begin{bmatrix} -\boldsymbol{I}\frac{R}{L_d} + \boldsymbol{J}\omega_e \frac{L_d - L_q}{L_d} & -\frac{\boldsymbol{I}}{L_d} \\ \boldsymbol{0} & \boldsymbol{J}\omega_e \end{bmatrix}\begin{bmatrix} \boldsymbol{i} \\ \boldsymbol{e} \end{bmatrix} + \begin{bmatrix} \frac{\boldsymbol{I}}{L_d} \\ \boldsymbol{0} \end{bmatrix}\boldsymbol{v}, \tag{3.5}$$

where

$$\boldsymbol{I} = \begin{bmatrix} 1 & 0 \\ 0 & 1 \end{bmatrix}, \boldsymbol{J} = \begin{bmatrix} 0 & -1 \\ 1 & 0 \end{bmatrix}, \boldsymbol{0} = \begin{bmatrix} 0 & 0 \\ 0 & 0 \end{bmatrix}.$$

The EEMF model was first presented in (CHEN et al., 2003) and can be used in order to implement the estimation algorithms previosly used to the SPMSM. Furthermore, the IPMSM state space model (3.5) is the dynamical representation of all sinusoidal synchronous machines. When $L_q = L_d$, the model produces the behavior of the SPMSM. When $\psi = 0$, these differential equations model the synchronous reluctance motor. Thus, the proposed analysis and design of this chapter can be extended to the mentioned motors beyond IPMSM.

3.2 Adaptive Full-Order Observer for Rotor Position and Speed Estimation

By means of the state space model (3.5) obtained in the previous section, the full-order state observer is proposed as

$$\frac{d}{dt}\begin{bmatrix} \hat{\boldsymbol{i}} \\ \hat{\boldsymbol{e}} \end{bmatrix} = \begin{bmatrix} -\boldsymbol{I}\frac{R}{L_d} + \boldsymbol{J}\hat{\omega}_e \frac{L_d - L_q}{L_d} & -\frac{\boldsymbol{I}}{L_d} \\ \boldsymbol{0} & \boldsymbol{J}\hat{\omega}_e \end{bmatrix}\begin{bmatrix} \boldsymbol{i} \\ \hat{\boldsymbol{e}} \end{bmatrix} + \begin{bmatrix} \frac{\boldsymbol{I}}{L_d} \\ \boldsymbol{0} \end{bmatrix}\boldsymbol{v} + \boldsymbol{H}\tilde{\boldsymbol{i}}, \tag{3.6}$$

where $\boldsymbol{H} = \begin{bmatrix} h_1\boldsymbol{I} + h_2\boldsymbol{J} & h_3\boldsymbol{I} + h_4\boldsymbol{J} \end{bmatrix}^T$ is the feedback gain matrix and the elements $\hat{\cdot}$ and $\tilde{\cdot}$ express the estimated variables and the error between the estimated variables and the actual variables, respectively. The measured stator current is used instead of the observed current in the state observer for later design simplifications.

Rotor flux speed estimation is performed through the following adaptation mechanism

$$\hat{\omega}_e = -\hat{\boldsymbol{e}}^T \boldsymbol{J}\tilde{\boldsymbol{i}} \left(k_p + \frac{k_i}{\rho} \right), \tag{3.7}$$

where k_p and k_i are the adaptive gains. This estimation method (3.7) is the well known gradient descent algorithm (IOANNOU; SUN, 1995).

The rotor flux position, used for the axis transformations, can be estimated through the angle of observed EEMF as

$$\hat{\theta}_e = \tan^{-1} \left(-\frac{\hat{e}_\alpha}{\hat{e}_\beta} \right). \tag{3.8}$$

3.3 Cascade Design Guidelines for the Adaptive and Feedback Gains

In this section, a gain design method will be proposed for the IPMSM adaptive full-order observer. Stability of the observer for all operating speed range is a minimum requirement of the project. Moreover, high performance drivers demand good dynamic performance of rotor speed and position estimations.

By subtracting (3.5) from (3.6), the error equations of the state observer are obtained as

$$\frac{d}{dt}\begin{bmatrix} \tilde{\boldsymbol{i}} \\ \tilde{\boldsymbol{e}} \end{bmatrix} = \underbrace{\begin{bmatrix} h_1\boldsymbol{I} + h_2\boldsymbol{J} & -\frac{\boldsymbol{I}}{L_d} \\ h_3\boldsymbol{I} + h_4\boldsymbol{J} & \boldsymbol{J}\omega_e \end{bmatrix}}_{\boldsymbol{A}} \begin{bmatrix} \tilde{\boldsymbol{i}} \\ \tilde{\boldsymbol{e}} \end{bmatrix} + \underbrace{\begin{bmatrix} \boldsymbol{0} \\ \boldsymbol{I} \end{bmatrix}}_{\boldsymbol{B}_1} \boldsymbol{J}\hat{\boldsymbol{e}}\tilde{\omega}_e + \underbrace{\begin{bmatrix} \frac{L_d-L_q}{L_d}\boldsymbol{I} \\ \boldsymbol{0} \end{bmatrix}}_{\boldsymbol{B}_2} \boldsymbol{J}\boldsymbol{i}\tilde{\omega}_e, \tag{3.9}$$

where the output error is giving by

$$\tilde{\boldsymbol{i}} = \underbrace{\begin{bmatrix} \boldsymbol{I} & \boldsymbol{0} \end{bmatrix}}_{\boldsymbol{C}} \begin{bmatrix} \tilde{\boldsymbol{i}} \\ \tilde{\boldsymbol{e}} \end{bmatrix}. \tag{3.10}$$

Through the error equations of the state observer (3.9) and the gradient algorithm (3.7), the overall closed-loop structure of the rotor speed estimation system is established. The block diagram of this structure, illustrated in Fig. 3.1, demonstrates that the estimated speed behavior depends on both state observer and adaptive law performances.

A cascade design strategy is proposed in order to simplify the adaptive observer analysis. In this method, the state observer feedforward is designed to operate at signif-

Figure 3.1: Error block diagram of the proposed adaptive observer cascade design method.
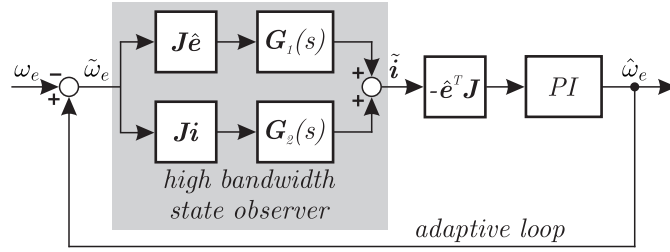
icantly higher frequencies than the adaptive feedback loop, which dominates the speed estimator dynamics.

By applying the cascade design strategy, the state observer feedfoward does not offers additional dynamics for the adaptive law and, therefore, can be seen as a static gain. Thus, the feedback and adaptation gains can be designed separately through the cascade strategy.

3.3.1   State observer design

The observer error is excited by rotor speed estimation error and its frequency domain model is given by

$$\tilde{\boldsymbol{i}} = \boldsymbol{G}_1\left(s\right)\boldsymbol{J}\hat{\boldsymbol{e}}\tilde{\omega}_e + \boldsymbol{G}_2\left(s\right)\boldsymbol{J}\boldsymbol{i}\tilde{\omega}_e, \tag{3.11}$$

where

$$\boldsymbol{G}_1\left(s\right) = \ \boldsymbol{C}[s\boldsymbol{I} - \boldsymbol{A}]^{-1}\boldsymbol{B}_1 = \ \frac{-[s^2\boldsymbol{I} + \left(a_1\boldsymbol{I} + a_2\boldsymbol{J}\right)s + a_3\boldsymbol{I} + a_4\boldsymbol{J}]^{-1}}{L_d}, \tag{3.12}$$

and

$$\begin{cases} a_1 = -h_1 \\ a_2 = -\omega_e - h_2 \\ a_3 = \frac{h_3}{L_d} - \omega_e h_2 \\ a_4 = \frac{h_4}{L_d} + \omega_e h_1 \end{cases} . \tag{3.13}$$

The transfer function $\boldsymbol{G}_2\left(s\right)$ can be written as a function of $\boldsymbol{G}_1\left(s\right)$ as follows

$$\boldsymbol{G}_2\left(s\right) = \ \boldsymbol{C}[s\boldsymbol{I} - \boldsymbol{A}]^{-1}\boldsymbol{B}_2 = \ \left(L_q - L_d\right)\left(s\boldsymbol{I} - \omega_e\boldsymbol{J}\right)\boldsymbol{G}_1\left(s\right). \tag{3.14}$$

Stability and bandwidth of the state observer are given by the placement of the eigenvalues of the state matrix $\boldsymbol{A}$. A standard pole placement method can be used to achieve the desired design requirements. The feedback gains of the state observer are

designed as follows

$$\begin{cases} h_1 = -2\Gamma_1 \\ h_2 = -\omega_e \\ h_3 = L_d \left(\omega_e h_2 + \Gamma_1^2\right) \\ h_4 = -L_d \omega_e h_1 \end{cases}, \tag{3.15}$$

where Γ_1 is the place of all eigenvalues of $\boldsymbol{A}$ in the real negative axis.

Unfortunately, the actual rotor flux speed is not available for the computation of the feedback gains and, therefore, the estimated speed must be used instead. This substitution is only ideal when $\tilde{\omega}_e = 0$, and in the other cases, the eigenvalues of $\boldsymbol{A}$ change the designed positions. Since speed estimation error is expected in real applications due to stator current measurement noise and the acceleration and deceleration of the IPMSM, the state observer poles behavior under speed estimation error must be investigated.

The two pair of conjugated poles $\boldsymbol{P}$ of the state matrix $\boldsymbol{A}$ are given by the following expression

$$\boldsymbol{P} = \frac{h_1 \boldsymbol{I}}{2} + \frac{(h_2 + \omega_e)\boldsymbol{J}}{2} \pm \frac{1}{2}\sqrt{\left(h_1^2 - 4h_3 L_d^{-1} + (h_2 - \omega_e)^2\right)\boldsymbol{I} + 2\left(h_1\left(h_2 - \omega_e\right) - 2L_d^{-1}h_4\right)\boldsymbol{J}} \tag{3.16}$$

By replacing the actual rotor flux speed by the estimated speed in the pole placement design method (3.15) and substituting the new feedback gains in (3.16), the poles of the state observer under speed estimation error are obtained as

$$\boldsymbol{P} = -\Gamma_1 \boldsymbol{I} - \frac{\tilde{\omega}_e}{2}\boldsymbol{J} \pm \frac{1}{2}\sqrt{\left(3\tilde{\omega}_e^2 - 4\omega_e\tilde{\omega}_e\right)\boldsymbol{I} - \left(4\Gamma_1\tilde{\omega}_e\right)\boldsymbol{J}}. \tag{3.17}$$

Figure 3.2: Stability boundary for the proposed state observer design.
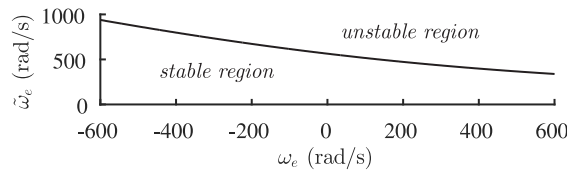
For the proposed design, the pole locations are only dependent on Γ_1, ω_e and $\tilde{\omega}_e$. When $\tilde{\omega}_e = 0$, all four poles of the state observer are placed in $-\Gamma_1$. As $|\tilde{\omega}_e|$ increases, the observer poles continuously diverge from the designed position and, eventually, the system becomes unstable. The state observer stability boundary from the proposed design strategy, with $\Gamma_1 = \omega_{e-rated} = 564$ rad/s, is presented in Fig. 3.2. As can be seen, the state observer operation point with least robustness is at maximum speed with speed estimation error with same signal.

In order to illustrate the behavior of the observer poles for speed estimation error,

Figure 3.3: Behavior of the normalized poles of the state observer under speed estimation error with (a) $\Gamma_1 = \omega_{e-rated}$ and $\omega_e = 0.2\omega_{e-rated}$, (b) $\Gamma_1 = \omega_{e-rated} = \omega_e$, (c) $\Gamma_1 = 2\omega_{e-rated}$ and $\omega_e = \omega_{e-rated}$ and (d) $\Gamma_1 = 10\omega_{e-rated}$ and $\omega_e = \omega_{e-rated}$.

(a)   (b)

(c)   (d)
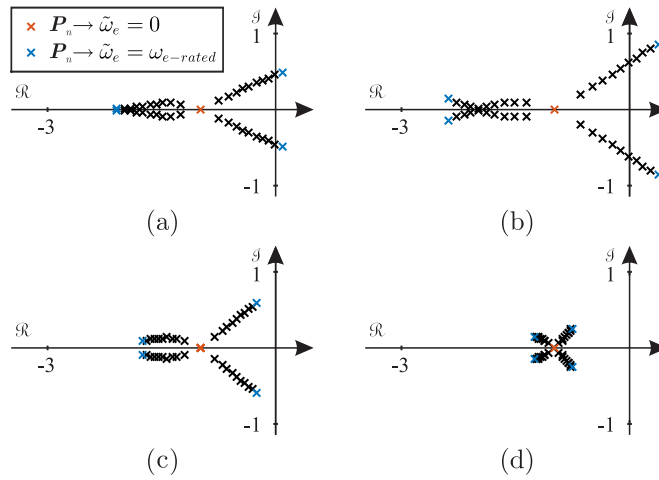
the normalized poles $\boldsymbol{P}_n$ are defined as

$$\boldsymbol{P}_n = \frac{\boldsymbol{P}}{\Gamma_1}. \tag{3.18}$$

Fig. 3.3 presents the behavior of the normalized observer poles with the proposed designed method under speed estimation error. The normalized observer poles operating at low speed $\omega_e = 0.2\omega_{e-rated}$ and rated speed $\omega_e = \omega_{e-rated}$, with $\Gamma_1 = \omega_{e-rated}$, are shown in Fig. 3.3 (a) and Fig. 3.3 (b), respectively. Clearly, as the rotor speed increases, the proposed design method becomes more susceptible to speed estimation error. This effect can be reduced with increase of Γ_1, as is illustrated in Fig. 3.3 (c) and Fig. 3.3 (d), where the IPMSM operates at nominal speed and $\Gamma_1 = 2\omega_{e-rated}$ and $\Gamma_1 = 10\omega_{e-rated}$, respectively. In all cases, when $\tilde{\omega}_e = 0$, the normalized poles are placed at -1. However, the sensitivity of the observer for speed estimation error changes as the bandwidth increases. Clearly, as Γ_1 raises, the poles are less affected by speed estimation error and keep closer to the designed location, resulting in an improvement of robustness.

Stability of the full-order observer is dependent on the actual rotor flux speed and, therefore, left half plane poles can not be stated for all rotor speed values. However, real applications use finite values. Then, by placing the poles significantly faster than the maximum IPMSM operation rotor flux speed will make the observer becomes robust to large speed estimation errors.

The bandwidth of the state observer can not be increased indefinitely because the system can become unstable with some discretization methods. Therefore, the sampling frequency becomes a limiting parameter in the design process.

In order to evaluate the state observer stability in the discrete time, the forward Euler method is employed. By replacing $s = \frac{z-1}{T_s}$, the state observer discrete-time stability condition under $\tilde{\omega}_e = 0$ is obtained as

$$-1 \leq (1 - T_s\Gamma_1) \geq 1. \tag{3.19}$$

From (3.17) and (3.19), the characteristic of robustness, performance and discrete-time stability of the state observer are highlighted.

3.3.2 Adaptive feedback loop design

The role of the adaptive feedback loop is to ensure proper estimation of the rotor speed and its dynamics can be altered by adjusting the performance of the adaptive law. According to the gradient algorithm (3.7), the transfer function from the current error to the estimated speed is given by

$$\boldsymbol{D}(s) = \frac{\hat{\omega}_e}{\tilde{\boldsymbol{i}}} = -\hat{\boldsymbol{e}}^T\boldsymbol{J}\left(k_p + \frac{k_i}{s}\right). \tag{3.20}$$

Through (3.11) and (3.20), the transfer function between the estimated and the actual rotor speed can be written as

$$\boldsymbol{W}(s) = \frac{\hat{\omega}_e}{\omega_e} = \overbrace{-\boldsymbol{D}(s)\left(\boldsymbol{G}_1(s)\boldsymbol{J}\hat{\boldsymbol{e}} + \boldsymbol{G}_2(s)\boldsymbol{J}\boldsymbol{i}\right)}^{\boldsymbol{E}(s)}[-\boldsymbol{D}(s)\left(\boldsymbol{G}_1(s)\boldsymbol{J}\hat{\boldsymbol{e}} + \boldsymbol{G}_2(s)\boldsymbol{J}\boldsymbol{i}\right) + 1]^{-1}, \tag{3.21}$$

where $\boldsymbol{E}(s)$ is the speed estimation forward path.

Since the state observer bandwidth is designed faster than the maximum rotor flux speed, which is considerably larger than the desired adaptive feedback loop bandwidth, the dynamics of the state observer seen by the adaptive feedback loop are given by

$$\boldsymbol{G}_1(s)|_{s\boldsymbol{I}\to\boldsymbol{0}} = \frac{-\boldsymbol{I}}{L_d\Gamma_1^2}, \tag{3.22}$$

and

$$\boldsymbol{G}_2(s)|_{s\boldsymbol{I}\to\boldsymbol{0}} = (L_d - L_q)\,\omega_e\boldsymbol{J}\boldsymbol{G}_1(s)|_{s\boldsymbol{I}\to0}. \tag{3.23}$$

By replacing (3.20), (3.22) and (3.23) in $\boldsymbol{E}(s)$, the resulting adaptive observer forward path, with the proposed cascade design strategy, is obtained as follows

$$\boldsymbol{E}(s) = \left(k_p + \frac{k_i}{s}\right)\left(\frac{\hat{\boldsymbol{e}}^T\hat{\boldsymbol{e}} + (L_d - L_q)\,\hat{\boldsymbol{e}}^T\boldsymbol{J}\omega_e\boldsymbol{i}}{L_d\Gamma_1^2}\right). \tag{3.24}$$

The adaptive observer forward path can be simplified by the operation point in

the flux weakening strategy, such as follows

$$\boldsymbol{E}\left(s\right) = \left(k_p + \frac{k_i}{s}\right) \frac{\|\hat{\boldsymbol{e}}\| \left(\|\hat{\boldsymbol{e}}\| + \|\boldsymbol{i}\| \left(L_q - L_d\right) \omega_e \sin \theta_i\right)}{L_d \Gamma_1^2}, \tag{3.25}$$

where

$$\theta_i = \tan^{-1}\left(\frac{-i_d}{i_q}\right). \tag{3.26}$$

Due to the high bandwidth of the state observer design, the norm of the observed EEMF can be regarded as approximately the actual. Thus, it is possible to make the consideration (3.27). When the IPMSM is operating with $\mid i_q \mid \gg \mid i_d \mid$, the consideration (3.27) is valid because $\sin \theta_i \approx 0$. At the extreme of the flux weakening operation, when $\mid i_q \mid \ll \mid i_d \mid$, the right part of (3.27) becomes the reluctance portion of the EEMF and, therefore, significantly smaller than the observer EEMF.

$$\|\hat{\boldsymbol{e}}\| \gg \|\boldsymbol{i}\| \left(L_q - L_d\right) \omega_e \sin \theta_i. \tag{3.27}$$

This consideration makes it possible to simplify the speed estimation dynamics (3.21) such as follows

$$\boldsymbol{W}\left(s\right) = \frac{\hat{\omega}_e}{\omega_e} \approx \frac{\left(k_p + \frac{k_i}{s}\right) \frac{\|\hat{e}\|^2}{L_d \Gamma_1^2}}{\left(k_p + \frac{k_i}{s}\right) \frac{\|\hat{e}\|^2}{L_d \Gamma_1^2} + 1}. \tag{3.28}$$

Equation (3.28) shows the nonlinear behavior of the adaptive observer. For fixed adaptation PI gains, the estimated speed will have different performances for each EEMF vector value. In addition, the sensorless IPMSM drive is required to operate in a wide speed range with high performance and the estimation method must maintain its behavior throughout the entire operation range. Here, in order to linearize the speed estimation performance, this chapter proposes the following design guidelines of the adaptation PI gains

$$\begin{cases} k_p = 0 \\ k_i = \frac{L_d \Gamma_1^2 \Gamma_2}{\|\hat{e}\|^2} \end{cases}, \tag{3.29}$$

where Γ_2 gives the location of the dominant pole of the adaptive feedback loop.

The resulting adaptive feedback loop behavior with the proposed PI adaptation gains is obtained by replacing (3.29) into (3.28), which results,

$$\boldsymbol{W}\left(s\right) = \frac{\hat{\omega}_e}{\omega_e} \approx \frac{\Gamma_2}{s + \Gamma_2}. \tag{3.30}$$

The presented adaptive observer cascade design method culminates with the dynamics of the estimated speed equal to a first order filter with a pole in -Γ_2.

Past papers (PO-NGAM; SANGWONGWANICH, 2012; PIIPPO; HINKKANEN; LUOMI, 2008; HINKKANEN et al., 2018) have used the proportional portion in the adap-

tive algorithm aiming to improve the damping of the speed estimation. In the proposed method, the feedback gain matrix is designed targeting higher frequencies. This strategy, in addition to improving the state observer robustness for speed estimation error, makes the dynamics so fast that do not affect the adaptive feedback loop. Thus, in the proposed cascade design method, the adaptive law achieve suitable damping without the need of the proportional gain, which makes the speed estimation insensitive to current noise.

The first order behavior of the adaptive feedback loop is illustrated in Fig. 3.4. A speed closed-loop control system with sensor is implemented with a bandwidth of $\omega_n = 6$ rad/s, where ω_n is the closed-loop speed control bandwidth, and the state observer is set with Γ_1 ten times faster than the IPMSM nominal rotor flux speed. In order to illustrate the linear performance of the rotor speed estimation algorithm, the adaptive feedback loop was simulated with gains chosen as $\Gamma_2 = \omega_n$ and $\Gamma_2 = 10\omega_n$. As presented through (3.30), the estimated speed converges towards the actual speed with a first order behavior defined by Γ_2.

Sensorless closed-loop control requires small speed estimation error. Therefore, Fig. 3.4 shows that the adaptive loop must operate at higher frequencies than the closed-loop control system bandwidth to precisely estimate the rotor speed through the system dynamics. When Γ_2 was selected as $10\omega_n$, high estimation performance was achieved.

Figure 3.4: Adaptive feedback loop estimation performance in a closed-loop speed control with sensor with $\Gamma_2 = \omega_n$ and $\Gamma_2 = 10\omega_n$.
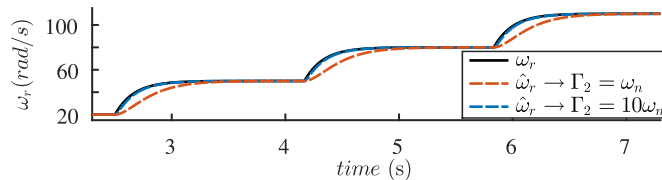
3.3.3   Comments on the proposed adaptive observer cascade design method

The presented cascade design method reduce the six gains of the adaptive observer in two intuitive design variables. For the selection of Γ_1 and Γ_2, the proposed adaptive observer cascade design method can be summarized as follows

1. The bandwidth of the adaptive feedback loop must be selected at lower frequencies so that the dynamics of the state observer can be disregarded. However, Γ_2 should be chosen high enough for good estimation of the rotor speed dynamics. Thus, the design guidelines for Γ_2 are given as

$$\omega_n \ll \Gamma_2 \ll \Gamma_{1-min}, \tag{3.31}$$

where $\Gamma_{1-\min}$ is the minimum value of Γ_1.

2. The state observer must have a fast response so it can be treated as a gain for the adaptive feedback loop. Furthermore, high state observer bandwidth is desired to expand the system robustness and the limitations of the bandwidth increase is the sampling time T_s. Therefore, the choice of Γ_1 should respect the following expression

$$\omega_{e-\max} \ll \Gamma_1 \ll \frac{2}{T_s}. \tag{3.32}$$

A fixed state observer bandwidth can lead to distinct response to measurement noise for each speed operation point. For a normalized noise response, the state observer bandwidth can be adjusted as the estimated speed changes, such as

$$\Gamma_1 = \hat{\omega}_e k_1, \tag{3.33}$$

with the cascade design limiting Γ_1 as

$$\begin{cases} \Gamma_{1-\min} = k_2 \Gamma_2 \\ (1 - T_s \Gamma_{1-\max}) \geq -1 \end{cases} \tag{3.34}$$

where k_2 is the minimum relationship between the state observer and adaptive loop frequencies, required for the cascade design method.

By respecting the restrictions (3.32) and (3.31), the adaptive observer has good performance for tracking both the rotor flux position and speed at medium to high speed values. However, at the singularity point $\omega_e = 0$, the EEMF vector becomes equal to zero and the rotor flux position (3.8) becomes unobservable, highlighting the low-speed limitations of the EEMF model. Furthermore, the rotor speed adaptive estimation is dependent on the EEMF vector (3.7) and when the rotor speed is at standstill, the gradient algorithm becomes stagnant. This phenomenon manifest the absence of persistent excitation in the adaptive system (BOYD; SASTRY, 1986).

The proposed adaptation gains design guidelines (3.29) tend to infinite at low speed operation. In order to maintain the estimator stability, the adaptation gain must be saturated as follows

$$k_i = \min \left[\frac{L_d \Gamma_1^2 \Gamma_2}{\hat{e}^T \hat{e}}, k_{i-\max} \right], \tag{3.35}$$

where k_{i-max} is the maximum adaptation gain.

3.4 Effects of Parameter Variation

The adaptive observer depend upon the d and q axes inductances and the stator resistance values for proper operation. Nonetheless, these parameters are subject to

variation due to temperature, skin effect and flux saturation, which may affect the performance of the rotor speed and position estimation algorithm. In (TOMITA et al., 1998; PO-NGAM; SANGWONGWANICH, 2012), the effects of parameter variation were analyzed for the adaptive observer applied to the SPMSM. The effects of inductance error on position estimation for the synchronous reluctance motor are studied in (ICHIKAWA et al., 2006b). In this section, these effects are evaluated for the adaptive observer applied to the IPMSM.

In order to investigate the effects of parameter variation, the adaptive observer (3.6) is rewritten as

$$\frac{d}{dt}\begin{bmatrix} \hat{\boldsymbol{i}} \\ \hat{\boldsymbol{e}} \end{bmatrix} = \begin{bmatrix} -\boldsymbol{I}\frac{\hat{R}}{\hat{L}_d} + \boldsymbol{J}\hat{\omega}_e\frac{\hat{L}_d - \hat{L}_q}{\hat{L}_d} & -\frac{\boldsymbol{I}}{\hat{L}_d} \\ \boldsymbol{0} & \boldsymbol{J}\hat{\omega}_e \end{bmatrix}\begin{bmatrix} \boldsymbol{i} \\ \hat{\boldsymbol{e}} \end{bmatrix} + \begin{bmatrix} \frac{\boldsymbol{I}}{\hat{L}_d} \\ \boldsymbol{0} \end{bmatrix}\boldsymbol{v} + \boldsymbol{H}\tilde{\boldsymbol{i}}, \tag{3.36}$$

where $\hat{R}$, $\hat{L}_d$ and $\hat{L}_q$ are the nominal values of R, L_d and L_q.

3.4.1   Effects of Resistance Variation

Considering resistance variation without inductance variation, that is, $\tilde{R} \neq 0$ and $\tilde{L}_d = \tilde{L}_q = 0$, the current estimation error in the frequency domain becomes

$$\tilde{\boldsymbol{i}} = \boldsymbol{G}_1(s)\boldsymbol{J}\hat{\boldsymbol{e}}\tilde{\omega}_e + \boldsymbol{G}_2(s)\boldsymbol{J}\boldsymbol{i}\tilde{\omega}_e + \boldsymbol{G}_{\tilde{R}}(s)\tilde{R}\boldsymbol{i}, \tag{3.37}$$

where

$$\boldsymbol{G}_{\tilde{R}}(s) = \boldsymbol{C}[s\boldsymbol{I} - \boldsymbol{A}]^{-1}\boldsymbol{B}_{\tilde{R}} = \boldsymbol{G}_1(s)(s\boldsymbol{I} - \boldsymbol{J}\omega_e), \tag{3.38}$$

and $\boldsymbol{B}_{\tilde{R}} = \begin{bmatrix} -\frac{\boldsymbol{I}}{L_d} & \boldsymbol{0} \end{bmatrix}^T$.

Equation (3.37) gives the error model taking the stator resistance variation in consideration. The stability conditions of the adaptive observer with resistance error are the same of the state observer design since $\boldsymbol{G}_{\tilde{R}}(s)$ share of poles of $\boldsymbol{G}_1(s)$.

In steady state, it is obtained that

$$\boldsymbol{G}_{\tilde{R}}(s)|_{s\boldsymbol{I} \to \boldsymbol{J}\omega_e} = \boldsymbol{G}_1(s)|_{s\boldsymbol{I} \to \boldsymbol{J}\omega_e}(\boldsymbol{J}\omega_e - \boldsymbol{J}\omega_e) = 0. \tag{3.39}$$

It is demonstrated through (3.39) that the stator resistance does not affect the observed current at steady state. Thus, its is concluded that the speed estimation at steady state remains correct under stator resistance error.

The current estimation error differential equation under stator resistance error is given as follows

$$\frac{d}{dt}\tilde{\boldsymbol{i}} = (h_1\boldsymbol{I} + h_2\boldsymbol{J})\tilde{\boldsymbol{i}} + \left(\frac{L_d - L_q}{L_d}\right)\boldsymbol{J}\boldsymbol{i}\tilde{\omega}_e - \frac{\tilde{\boldsymbol{e}}}{L_d} - \frac{\tilde{R}}{L_d}\boldsymbol{i}. \tag{3.40}$$

Since the estimated speed and current are not affected by stator resistance variation, (3.40) at steady state takes form of

$$\tilde{\boldsymbol{e}} = -\tilde{R}\boldsymbol{i}. \tag{3.41}$$

The effects of resistance error in the position estimation can be quantified through Fig.3.5 (a), such as

$$\left|\tilde{\theta}_e\right| = \left|\sin^{-1}\frac{\tilde{\boldsymbol{e}}}{\boldsymbol{e}}\right| \sin\theta_i = \sin^{-1}\frac{\left\|\tilde{R}\boldsymbol{i}\right\|}{\|\boldsymbol{e}\|} \sin\theta_i, \tag{3.42}$$

At medium to high speeds, the EEMF assume big values and, therefore, the position estimation error should be insignificant with resistance variation.

3.4.2   Effects of d-axis Inductance Variation

Similarly as done before, it is considered d-axis inductance variation and $\tilde{R} = \tilde{L}_q = 0$. Through this consideration, the current estimation error in the frequency domain is given by

$$\tilde{\boldsymbol{i}} = \boldsymbol{G}_1\left(s\right)\boldsymbol{J}\hat{\boldsymbol{e}}\tilde{\omega}_e + \boldsymbol{G}_2\left(s\right)\boldsymbol{J}\boldsymbol{i}\tilde{\omega}_e + \boldsymbol{G}_1\left(s\right)\left(s\boldsymbol{I} - \boldsymbol{J}\omega_e\right)\left(1 - \frac{L_d}{\hat{L}_d}\right)\left(L_q\boldsymbol{J}\boldsymbol{i}\hat{\omega}_e + \hat{\boldsymbol{e}} + R\boldsymbol{i} - \boldsymbol{v}\right). \tag{3.43}$$

In the same manner as the stator resistance error, at steady state $(s\boldsymbol{I} - \boldsymbol{J}\omega_e)$ becomes equal to zero. Therefore, both the observed current and the estimated speed are not affected by the d-axis inductance error.

The current estimation error differential equation under d-axis inductance error is given as follows

$$\tilde{L}_d\frac{d}{dt}\boldsymbol{i} + \hat{L}_d\frac{d}{dt}\tilde{\boldsymbol{i}} = \hat{L}_d\left(h_1\boldsymbol{I} + h_2\boldsymbol{J}\right)\tilde{\boldsymbol{i}} + \tilde{L}_d\boldsymbol{J}\boldsymbol{i}\omega_e + \left(\hat{L}_d - L_q\right)\boldsymbol{J}\boldsymbol{i}\tilde{\omega}_e - \tilde{\boldsymbol{e}}. \tag{3.44}$$

Due to the current and speed estimation error are null at steady state, the EEMF error caused by the d-axis inductance error is given by

$$\tilde{\boldsymbol{e}} = 0. \tag{3.45}$$

It is shown through (3.45) and Fig.3.5 (b) that L_d error has no influence on the position estimation at steady state.

Figure 3.5: Observed EEMF phasor diagram with variation on (a) R, (b) L_d and (c) L_q.
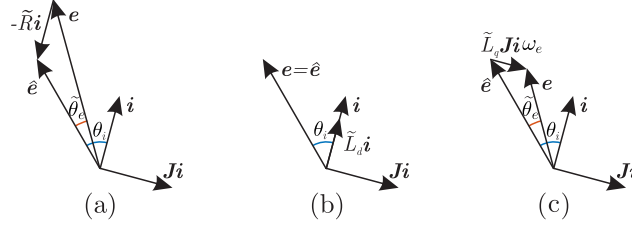
Source: DOI: 10.1109/TIE.2020.3007101, ©2021 IEEE.

3.4.3   Effects of q-axis Inductance Variation

For the q-axis inductance variation, is considered that $\tilde{R} = \tilde{L}_d = 0$. The current estimation error model under L_q error in the frequency domain is obtained as

$$\tilde{\boldsymbol{i}} = \boldsymbol{G}_1(s)\,\boldsymbol{J}\hat{\boldsymbol{e}}\tilde{\omega}_e + \boldsymbol{G}_2(s)\,\boldsymbol{J}\boldsymbol{i}\tilde{\omega}_e - \boldsymbol{G}_1(s)\,(s\boldsymbol{I} - \boldsymbol{J}\omega_e)\,\boldsymbol{J}\boldsymbol{i}\hat{\omega}_e\tilde{L}_q. \tag{3.46}$$

It is obtained that the q axis inductance variation does not effect the observer current due to $(s\boldsymbol{I} - \boldsymbol{J}\omega_e) = 0$ at steady state. It is concluded that impedance variation does not influence speed estimation. This is intuitive due to the fact that frequency of the stator current is not influenced by the inductances and stator resistance values.

The error equation of the observed current in relation to L_q variation is obtained as

$$L_d \frac{d}{dt}\tilde{\boldsymbol{i}} = \frac{(h_1\boldsymbol{I} + h_2\boldsymbol{J})}{L_d^{-1}}\tilde{\boldsymbol{i}} + \left(L_d - \hat{L}_q\right)\boldsymbol{J}\boldsymbol{i}\tilde{\omega}_e - \tilde{L}_q\boldsymbol{J}\boldsymbol{i}\omega_e - \tilde{\boldsymbol{e}}. \tag{3.47}$$

At steady state, the q axis inductance error has no effect on the current or speed estimation. Therefore, the EEMF error under L_q variation is obtained as

$$\tilde{\boldsymbol{e}} = -\tilde{L}_q\boldsymbol{J}\boldsymbol{i}\omega_e. \tag{3.48}$$

For the maximum torque per ampere control technique, the L_q variation causes a phase variation on the observed EEMF. Furthermore, the EEMF error is proportional to the IPMSM speed, and therefore, is significant throughout the entire speed range. Thus, position estimation is impaired under q-axis inductance error. This effect have been shown experimentally in the literature (NALAKATH et al., 2018). From Fig.3.5 (c), the position estimation error under $\tilde{L}_q$ can be quantified, such as

$$\left|\tilde{\theta}_e\right| = \left|\sin^{-1}\frac{\tilde{\boldsymbol{e}}}{\boldsymbol{e}}\right|\cos\theta_i = \sin^{-1}\frac{\left\|\tilde{L}_q\boldsymbol{i}\omega_e\right\|}{\|\boldsymbol{e}\|}\cos\theta_i. \tag{3.49}$$

From (3.49), it is clear that the position error estimation due to q-axis inductance error is reduced at deep flux weakening operation, which is commonly used in IPMSM

Parameter Error Effects	R	L_d	L_q
$\left\|\tilde{\theta}_e\right\|$	$\sin^{-1}\frac{\\|\tilde{R}\boldsymbol{i}\\|}{\\|\boldsymbol{e}\\|}\sin\theta_i$	0	$\sin^{-1}\frac{\\|\tilde{L}_q\boldsymbol{i}\omega_e\\|}{\\|\boldsymbol{e}\\|}\cos\theta_i$

Table 6: Summary of parameter error effects on position estimation.

drives (SEPULCHRE et al., 2018). The effects of parameter variation on position estimation are summarized in Table 6.

3.5   Experimental Results

The performance of the proposed adaptive full-order observer design method was verified experimentally in an IPMSM sensorless control operation. The IPMSM speed regulation is performed through a field oriented control algorithm with PI controllers. The sensorless algorithm was implemented in an interface with a DSP TMS320F28335, a voltage source inverter (VSI) and a IPMSM. The experimental setup photograph is shown in Fig..2 at Appendix A. Both sampling and inverter switching frequency were set to 10 kHz. The IPMSM parameters are presented in Table 7 at Appendix A. The Euler method is employed for integration of the differential equations of the adaptive observer in discrete-time. An absolute encoder gives the actual rotor position and rotor speed. The simplified diagram of the implemented sensorless control system is presented in Fig.3.6.

Figure 3.6: Sensorless control system diagram.
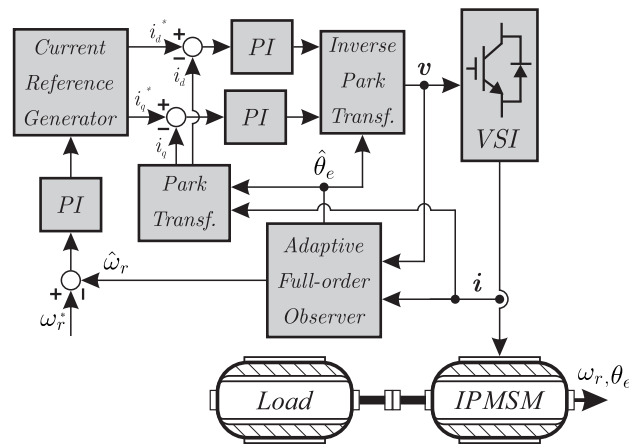
3.5.1   Cascade Design Validation

In order to evaluate the state observer stability boundary, two experiments were performed using speed control with position sensor. The rotor speed is regulated at $\omega_r = 100$ rad/s, which results in a rotor flux speed of $\omega_e = 300$ rad/s for 3 pole pairs,

and the state observer is designed with $\Gamma_1 = 2.5\omega_e$. The stability boundary of the state observer with $\Gamma_1 = 2.5\omega_e$ is illustrated in Fig.3.7.

Figure 3.7: Stability boundary for $\Gamma_1 = 2.5\omega_e$.
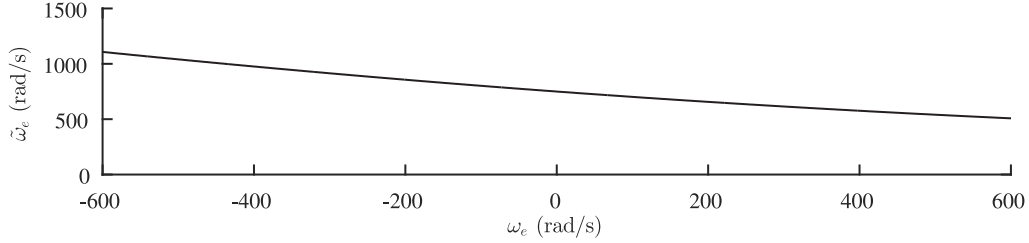
Source: Author.

In the first experiment, the adaptive observer operates at steady state and, at second 3, the estimated rotor flux speed is changed through software to $\hat{\omega}_e = 700$ rad/s, resulting in a rotor flux speed error of $\tilde{\omega}_e = 400$ rad/s and a rotor speed error of $\tilde{\omega}_r = \hat{\omega}_r - \omega_r$=233.3-100=133.3 rad/s, for 0.01 seconds. The adaptive observer response is demonstrate in Fig. 3.8 and the maximum error at the stability boundary is illustrated in Fig.3.9. As the error step puts the state observer in an operation point inside the stable region, and consequently, the estimated variables converge properly.

Figure 3.8: Experimental results for the stability boundary test with rotor speed error step.
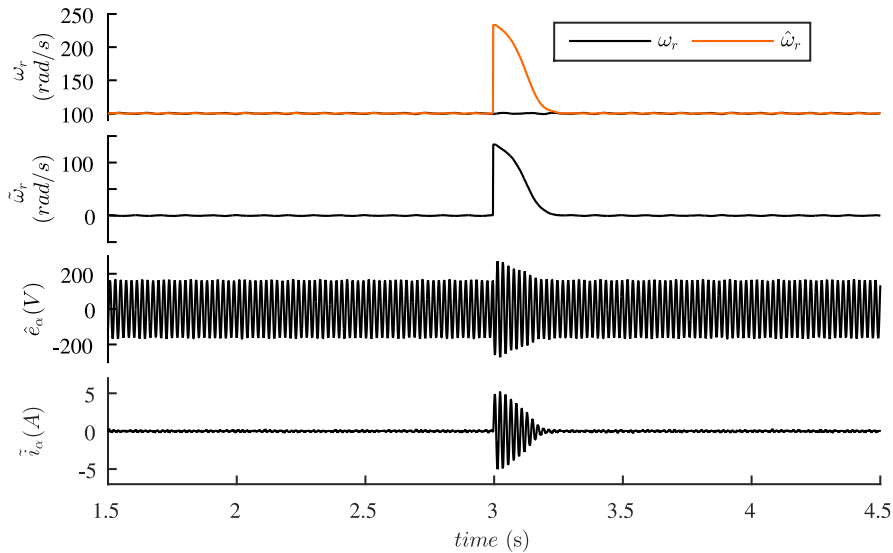
Source: Author.

The second operation is the reproduction of the first experiment with $\hat{\omega}_e = 1200$ rad/s, $\tilde{\omega}_e = 900$ rad/s and a rotor speed error of $\tilde{\omega}_r = \hat{\omega}_r - \omega_r$=400-100=300 rad/s. In this case, the speed estimation error step puts the adaptive observer in the unstable region.

Figure 3.9: Adaptive observer operation for Fig. 3.8.
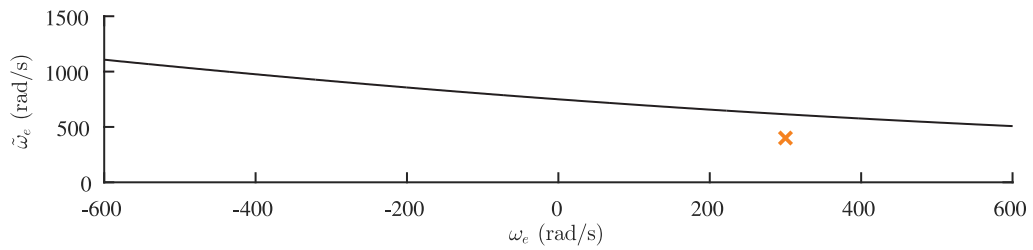
3.10 illustrates the results of the experiment and Fig. 3.11 illustrates the operation point in relationship to the stability boundary. The estimated variables did not recover from the error step and instability is visible from the experiment.

Figure 3.10: Experimental results for the stability boundary test with rotor speed error step.
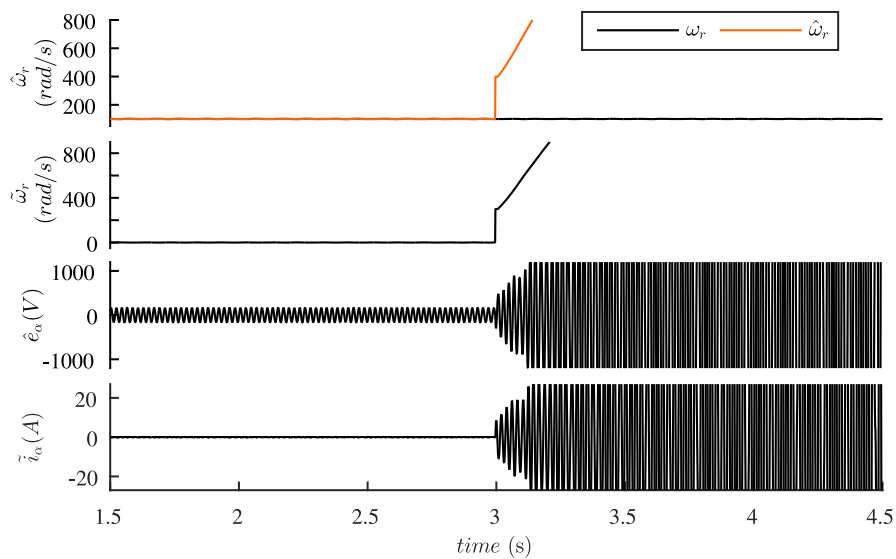
Figure 3.11: Adaptive observer operation for Fig. 3.10.
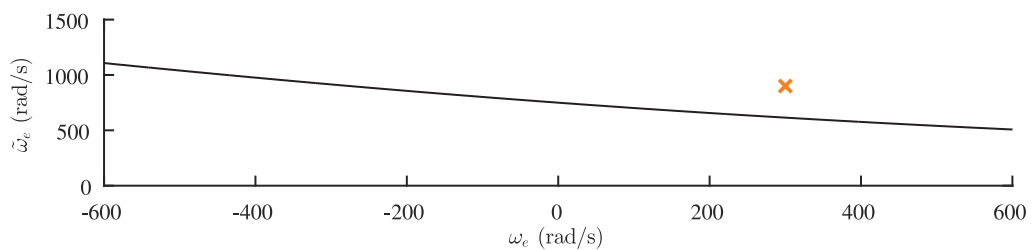
3.5.2   Sensorless Control Validation

The cascade design variables are defined with $\Gamma_2 = 60$, $\Gamma_1 = 5.3\hat{\omega}_e$ and limited by $(1 - T_s\Gamma_{1-\max}) = 0.7$ and $\Gamma_{1-\min} = 5\Gamma_2$. Performance of the adaptive observer under rotor speed acceleration and deceleration is presented in Fig.3.12. The speed reference begins with 20 rad/s and changes to 120 rad/s at 1 s and changes again to 20 rad/s at 5 s. This figure shows good rotor speed estimation performance through the entire experiment. The observed EEMF has its amplitude with a similar behavior as the rotor speed, as is expected. The state observer has also good performance to estimate the actual current and small error is obtained even with high transient currents. Fig.3.12 bottom illustrates

Figure 3.12: Adaptive observer experimental results under speed variation.

Source: DOI: 10.1109/TIE.2020.3007101, ©2021 IEEE.
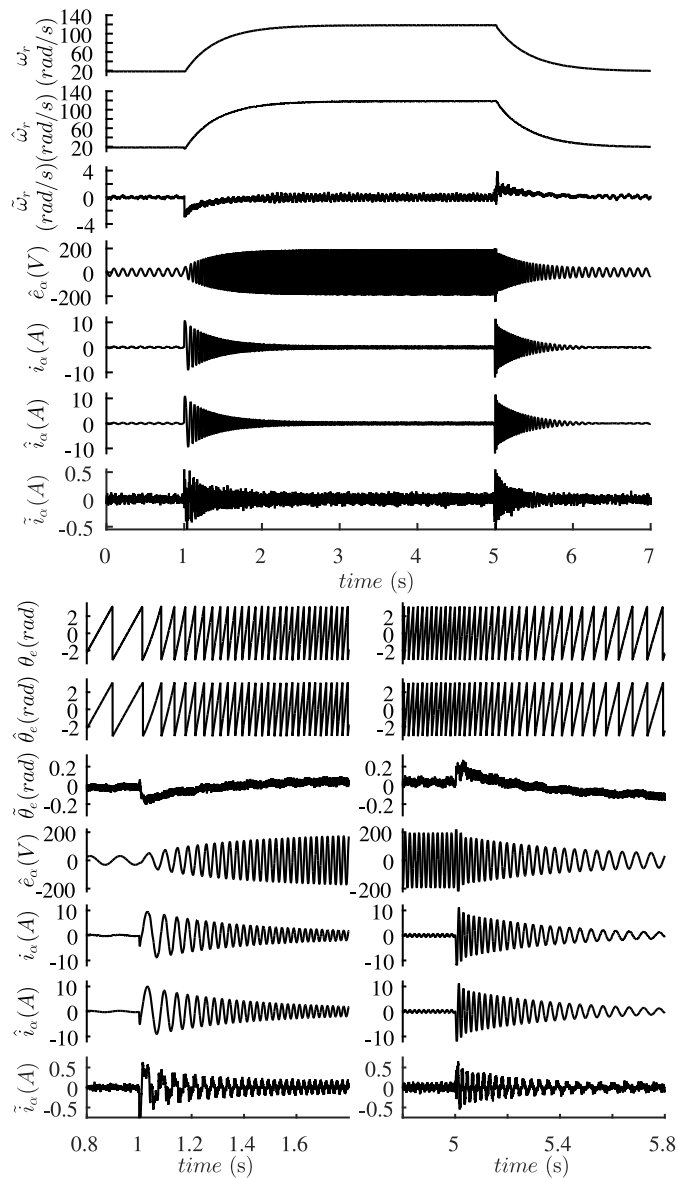
experimental results of rotor flux position estimation performance at IPMSM acceleration and deceleration. The cascade design strategy results in small position estimation error even under fast dynamics. The small position estimation error offers negligible impact on the field orientation control strategy. The observed current sustains small estimation error during the 10 A current overshoot. The observed EEMF maintain a sinusoidal behavior and the small position estimation error validate the phase estimation of the observed EEMF.

Figure 3.13: Adaptive observer experimental results at high speed with reduced sampling frequency.
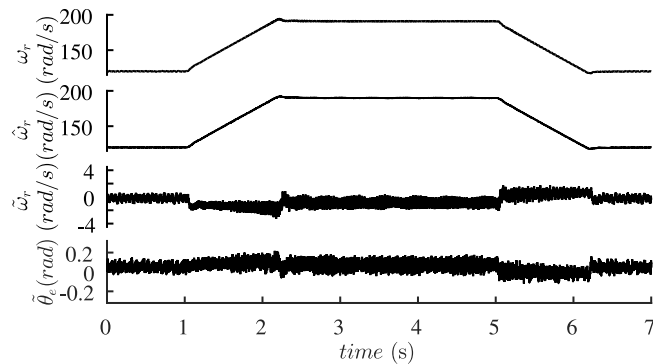
Figure 3.14: Adaptive observer experimental results under low speed.
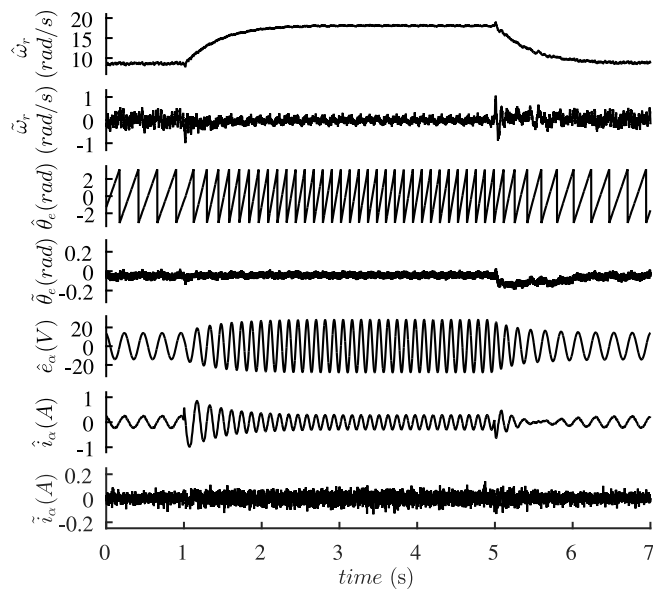
Since the proposed cascade design method requires a high bandwidth state observer, the performance at nominal speed is tested with a reduced sampling frequency

of 5 kHz. In order to maintain the state observer upper frequency limitation as $(1 - T_s\Gamma_{1-\max}) = 0.7$, the gain is adjusted to $\Gamma_1 = 2.65\hat{\omega}_e$. The nominal speed sensorless results are presented in Fig. 3.13 and small position and speed estimation error is noticed. The proposed adaptive full-order observer design method is evaluated at low-speed operation and presented in Fig. 3.14. The rotor speed shifts from 9 rad/s to 18 rad/s at 1s an back to 9 rad/s at 5s. Moderate transient position error is observed at deceleration when the current approaches zero without compromising the control algorithm.

Figure 3.15: Adaptive observer experimental results under shaft load.
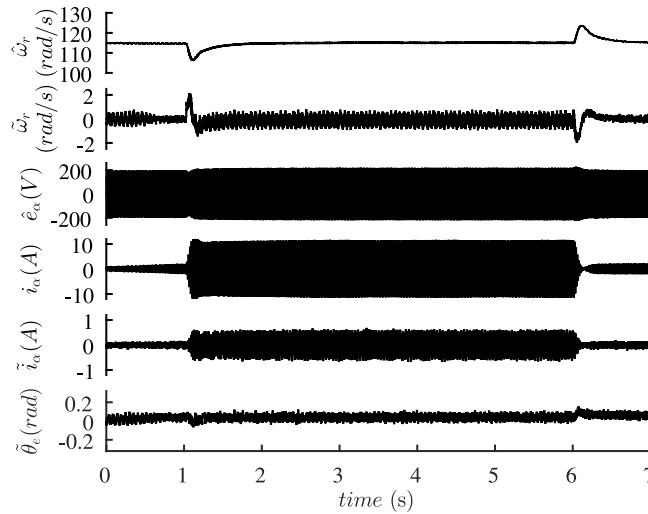
The parameter effects on position error estimation are highly related with the stator current magnitude, and therefore, experimental results under step load are performed. The load step results in a operation point of $i_d = -3.9$ A, $i_q = 10.7$ A and $\theta_i = 0.35$ rad. In order to evaluate q-axis parameter effects, the results are compared with the response with the actual inductance value in the operation point, which is given as as $L_q = 34$ mH. Experimental results of the IPMSM adaptive observer under shaft load is shown in Fig.3.15. The estimation error of all variables are equal to zero even under load sensorless operation. For evaluation of the obtained analytical effects of parameter variation, the experiment done in Fig.3.15 is repeated with parameter error in Fig.3.16. The Fig.3.16 (a) shows the adaptive observer under shaft load with resistance error of 50%. No significant effect is seen on the estimation of position, speed and current. Fig.3.16 (b) presents the adaptive observer under shaft load with d-axis inductance error of 20%. No visual effect is observed on the estimation of the adaptive observer variables. Adaptive observer under shaft load with q-axis inductance error of 20% is illustrated in Fig.3.16 (c). Considerable position error occur due to q-axis inductance error.

The average position estimation error resulted from q-axis inductance error is

Figure 3.16: Adaptive observer experimental results under load for variation of (a) 50% of R, (b) 20% of L_d and (c) 20% of L_q.
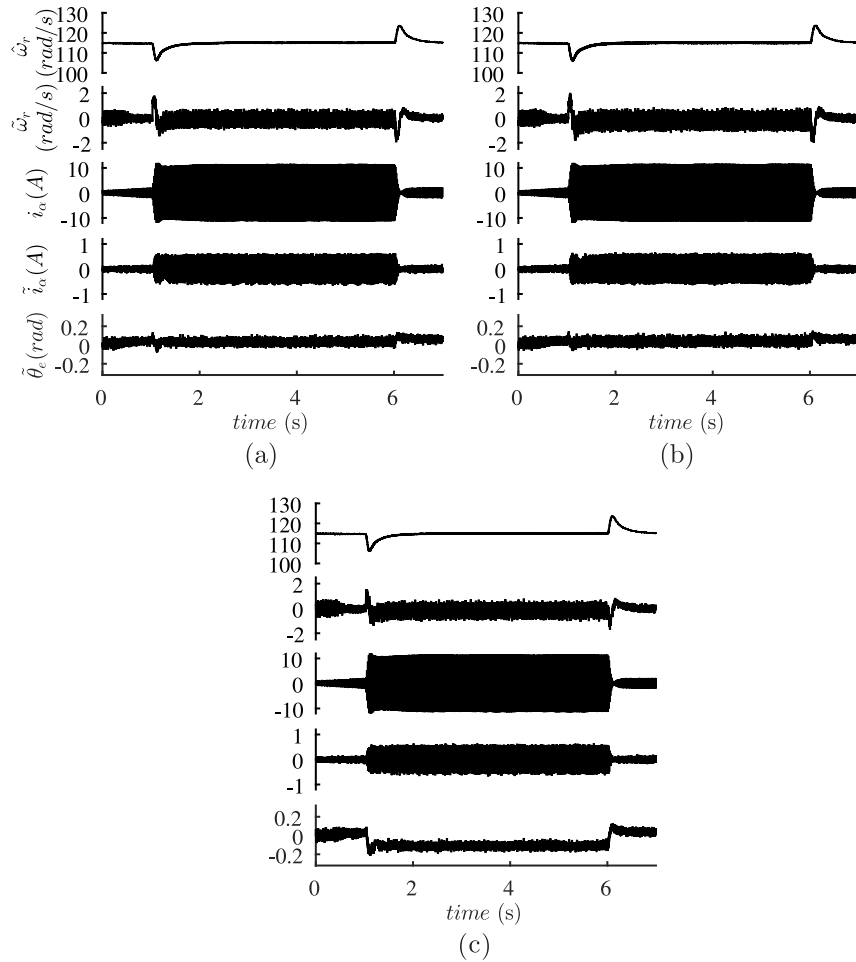
$\left|\tilde{\theta}_e\right|$ = 0.1175 rad, resulting in a torque error of 0.69%. The theoretical error (3.49) can be computed with the observed EEMF of Fig.3.15 as the actual, which results in a position error of $\left|\tilde{\theta}_e\right|$ = 0.1193 rad. The computed theoretical position estimation error for resistance variation (3.42) is obtained as $\left|\tilde{\theta}_e\right|$ = 0.0046 rad. Due to the absence of rotor flux speed in the position error equation (3.42) and to the operating angle θ_i, the resistance error has no visual effects on the steady state position estimation.

Flux weakening, MTPA and MTPV strategies are commonly used in IPMSM drives. In order to evaluate the effect of the i_d current change in the position estimation error under L_q variation, an experiment is performed and presented in Fig. 3.17. The IPMSM operates with $i_d = -5$ A and changes to $i_d = -17$ A when the load is applied, resulting in $\left|\tilde{\theta}_e\right|$ = 0.11 rad. While the load is applied, the flux weakening operation is changed to $i_d = -21$ A and then, to $i_d = -25$ A, resulting in position errors of $\left|\tilde{\theta}_e\right|$ = 0.04 rad and $\left|\tilde{\theta}_e\right|$ = 0.01 rad, respectively. As obtained by the theoretical analysis,

the position estimation error caused by $\tilde{L}_q$ is mitigated as the flux weakening is expanded.

Figure 3.17: Experimental results of flux weakening effects on position estimation error under variation of L_q.
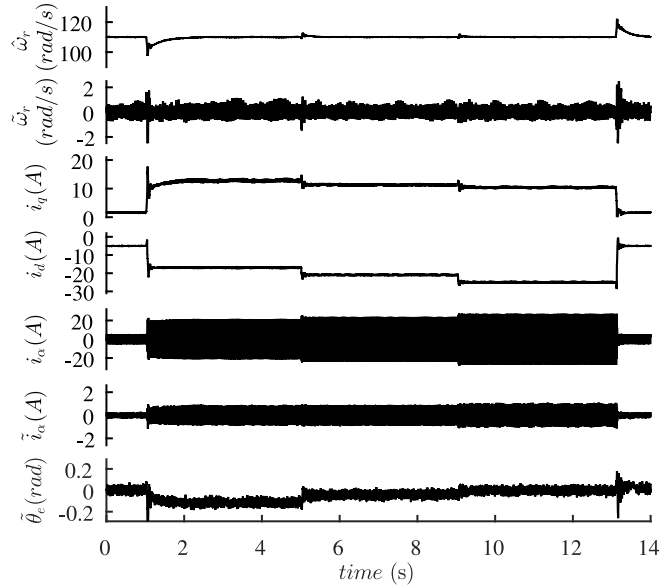
3.6 Chapter Conclusion

This chapter presented a rotor speed estimation method for sensorless IPMSM drives based on the adaptive full-order observer. The adaptive observer is build upon the obtained extended EMF linear model of the IPMSM. A cascade strategy is proposed for computation of the adaptation and feedback gains. The state observer is designed with high bandwidth to expand the observer stability conditions and to be considered as a gain by the adaptive feedback loop, which is responsible for good dynamic estimation of the rotor speed. Through the presented design guidelines, the tuning of the six gain adaptive observer is reduced to two intuitive design variables. The effects of adaptive observer parameter variation for rotor position and speed estimation are obtained analytically. It is concluded that only the q-axis inductance error impacts significantly the position estimation and no parameter error influences the rotor speed estimation at steady state. Experimental results are provided for verification of the proposed cascade design method and parameter variation analysis.

4 ADAPTIVE FULL-ORDER OBSERVER FOR FULL-RANGE SENSORLESS IPMSM DRIVES

Adaptive observers based on EEMF have been a major estimation strategy for high-speed sensorless IPMSM drives (HASEGAWA; YOSHIOKA; MATSUI, 2009; HASEGAWA; MATSUI, 2008; TOMITA; HASEGAWA; MATSUI, 2010; NOVAK; NOVAK, 2018; PONGAM; SANGWONGWANICH, 2012; FILHO; VIEIRA, 2020). This is mainly due to the linear behavior of the EEMF that allows the use of traditional estimation algorithms. However, at low-speed sensorless operation, the IPMSM requires HFSI for rotor position observability, which makes the standard linear EEMF model insufficient for achieving an adequate estimation algorithm.

The dominant approach for low-speed is to adapt the IPMSM model for HFSI (ZHAO; NALAKATH; EMADI, 2019; WANG; VALLA; SOLSONA, 2020). This methodology has as major drawback the low universality to changes in the HFSI method. Furthermore, development of specific low-speed estimation methods require a sensorless transition to the high-speed estimation algorithm, which increases the system complexity.

Recent research presented a new concept which allows full-range position estimation through EEMF observation by the quadratic EEMF (QEMF) (XIAO et al., 2021). This new variables feature an arbitrary use of HFSI methods since the demodulation process is inherent to the computing of the QEMF. Furthermore, the QEMF presents sinusoidal behavior with or without HFSI. Therefore, this approach enables to extend the adaptive observer presented in the Chapter 3 to a full-range IPMSM position estimation algorithm.

The motivation of this chapter is to develop an adaptive full-order observer in order to achieve high-performance full-range sensorless control. The main contributions of this chapter can be summarized such as follows:

- Modify and improve the adaptive full-order observer presented in the Chapter 3 aiming QEMF estimation for full-range sensorless control.

- Design guidelines for the adaptation and feedback gains are adapted from the cascade concept for the new developed adaptive observer. The proposed design framework has similar properties to the design method presented in Chapter 2.

4.1 IPMSM Model

As demonstrated in the Chapter 3, the IPMSM can be modeled in the stationary frame through the EEMF concept, such as

$$\boldsymbol{v} = \left[\left(R + \rho L_d \right) \boldsymbol{I} + \left(L_d - L_q \right) \omega_e \boldsymbol{J} \right] \boldsymbol{i} + \boldsymbol{e}, \tag{4.1}$$

where

$$\boldsymbol{e} = \left\{ (L_d - L_q) \left(\omega_e i_d - \rho i_q \right) + \omega_e \psi \right\} \begin{bmatrix} -\sin\theta_e \\ \cos\theta_e \end{bmatrix}. \tag{4.2}$$

At medium to high speeds the HFSI method is not used, and therefore, the constant load and constant speed assumption $\dot{i}_d = \dot{i}_q = \dot{\omega}_e = 0$ can be used in order to obtain the IPMSM linear model. This high-speed IPMSM representation is given by

$$\frac{d}{dt} \begin{bmatrix} \boldsymbol{i} \\ \boldsymbol{e} \end{bmatrix} = \begin{bmatrix} -\boldsymbol{I}\frac{R}{L_d} + \boldsymbol{J}\omega_e\frac{L_d-L_q}{L_d} & -\frac{\boldsymbol{I}}{L_d} \\ \boldsymbol{0} & \boldsymbol{J}\omega_e \end{bmatrix} \begin{bmatrix} \boldsymbol{i} \\ \boldsymbol{e} \end{bmatrix} + \begin{bmatrix} \frac{\boldsymbol{I}}{L_d} \\ \boldsymbol{0} \end{bmatrix} \boldsymbol{v}, \tag{4.3}$$

where

$$\boldsymbol{I} = \begin{bmatrix} 1 & 0 \\ 0 & 1 \end{bmatrix}, \boldsymbol{J} = \begin{bmatrix} 0 & -1 \\ 1 & 0 \end{bmatrix}, \boldsymbol{0} = \begin{bmatrix} 0 & 0 \\ 0 & 0 \end{bmatrix}.$$

At low-speed operation, the EEMF (4.2) becomes null and unobservable when $\rho i_q = 0$. Through HFSI, EEMF reaches enough magnitude for observability, but the product between derivatives of currents with $\sin\theta_e$ and $\sin\theta_e$ makes the demodulation process dependent on the accurate measurement of the high frequency current. Furthermore, at sensorless operation, the exact i_q current obtained by the park transformations calculated with θ_e can not be achieved. Only i_q obtained with $\hat{\theta}_e$ is available for the demodulation process. If position estimation error occurs, the demodulation will be incorrect, and therefore, additional position estimation error will follow, which can make the sensorless control system unstable.

A recent research allowed unify the high-speed EEMF (4.2) capabilities with the ρi_q portion through the quadratic extended electromotive force (QEMF) (XIAO et al., 2021) and, then, achieve an universal model for full-range IPMSM sensorless control.

The QEMF are defined as follows

$$\boldsymbol{Q} = \begin{bmatrix} Q_\alpha \\ Q_\beta \end{bmatrix} = \begin{bmatrix} 2e_\alpha e_\beta \\ e_\beta{}^2 - e_\alpha{}^2 \end{bmatrix} = M \begin{bmatrix} -\sin(2\theta_e) \\ \cos(2\theta_e) \end{bmatrix}, \tag{4.4}$$

where $M = \left\{ (L_d - L_q) \left(\omega_e i_d - \rho i_q \right) + \omega_e \psi \right\}^2$.

Unlike the EEMF, which with HFSI effect loses the synchronous sinusoidal behavior, the QEMF has a similar nature to the EEMF without HFSI since M is always positive. However, the QEMF is still high-frequency modulated and its fundamental frequency can be extracted through the following normalization procedure

$$\boldsymbol{Q}^n = \frac{\boldsymbol{Q}}{|\boldsymbol{Q}|} = \begin{bmatrix} -\sin(2\theta_e) \\ \cos(2\theta_e) \end{bmatrix}, \tag{4.5}$$

where $\boldsymbol{Q}^n$ is the normalized QEMF.

When the IPMSM is operating at high-speeds, the QEMF has sufficient magnitude

to be observed by standard estimation methods. At low-speeds, HFSI is employed in order to guarantee sufficient amplitude of M and, therefore, rotor position observability.

The overall EEMF and QEMF dynamics under square wave based HFSI are presented in Fig. 4.1. The rotor flux speed operates at $\omega_e = 15$ rad/s, the HFSI voltage magnitude is set to $v_h = 100$ V and HFSI frequency is adjusted to $f_h = 125$ Hz and $f_h = 500$ Hz. The HFSI includes an oscillatory behavior in the traditional EEMF dynamics and the EEMF fundamental can still be noticed in the envelop of the signal. Furthermore, the EEMF dynamics under HFSI loses the standard position estimation features since the high-frequency components appear in all the vector operating quadrants. This characteristic disappears for QEMF, where the high-frequency components appear with sign equal to terms $\sin(2\theta_e)$ and $\cos(2\theta_e)$. Finally, the normalized QEMF completes the demodulation procedure by removing the high-frequency components. This normalized QEMF presents a similar sinusoidal behavior from the EEMF at high-speeds and, therefore, rotor position estimation can be achieved from standard methods. The QEMF presents a fundamental with the double of the frequency of the EEMF fundamental.

Figure 4.1: Simulated waveforms of the EEMF, QEMF and normalized QEMF with square wave HFSI at $\omega_e = 15$ rad/s. (a) $v_h = 100$ V and $f_h = 125$ Hz and (b) $v_h = 100$ V and $f_h = 500$ Hz.
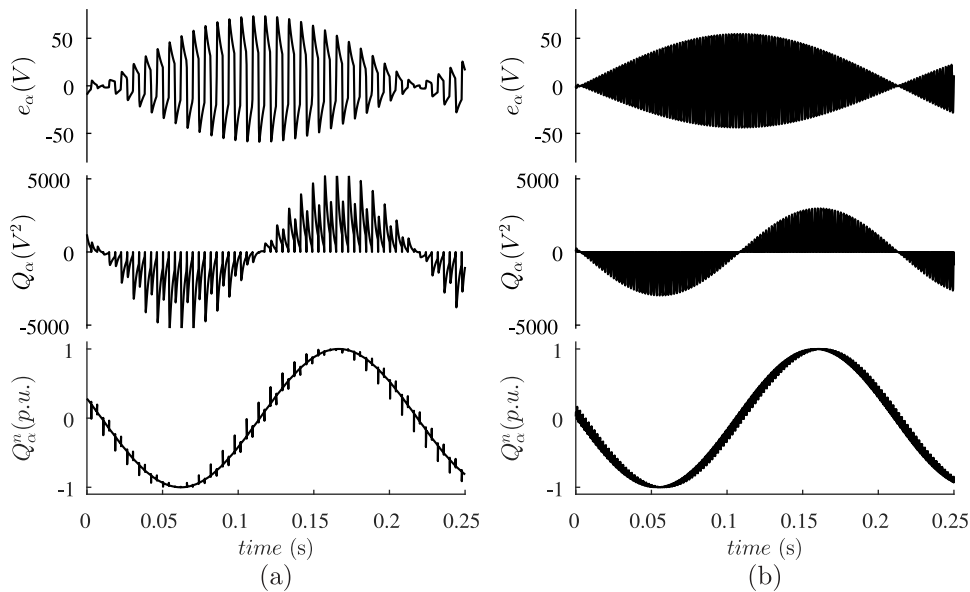
Source: Author.

The QEMF make it possible full-range sensorless operation through the estimation of the EEMF. At low-speeds, where the fundamental EEMF has small amplitude, HFSI is implemented to ensure position observability and the rotor position can be estimated from the normalized QEMF. When the IPMSM operates at medium to high-speeds, HFSI is removed and the EEMF changes its behavior to the standard sinusoidal fundamental based characteristic. Nonetheless, the normalized QEMF maintains the sinusoidal form

from the low-speed operation. Therefore, the position can be estimated throughout the entire operating range with the QEMF components and adequate HFSI.

4.2 Adaptive Full-Order Observer for Full-Range Rotor Position and Speed Estimation

The full-order observer presented in the Chapter 3 is modified for full-range sensorless operation, and is given by

$$\frac{d}{dt}\begin{bmatrix} \hat{\boldsymbol{i}} \\ \hat{\boldsymbol{e}} \end{bmatrix} = \begin{bmatrix} -\boldsymbol{I}\frac{R}{L_d} + \boldsymbol{J}\hat{\omega}_e\frac{L_d-L_q}{L_d} & -\frac{\boldsymbol{I}}{L_d} \\ \boldsymbol{0} & \boldsymbol{J}\hat{\omega}_e\sigma \end{bmatrix}\begin{bmatrix} \boldsymbol{i} \\ \hat{\boldsymbol{e}} \end{bmatrix} + \begin{bmatrix} \frac{\boldsymbol{I}}{L_d} \\ \boldsymbol{0} \end{bmatrix}\boldsymbol{v} + \boldsymbol{H}\tilde{\boldsymbol{i}}, \qquad (4.6)$$

where $\boldsymbol{H} = \begin{bmatrix} h_1\boldsymbol{I} + h_2\boldsymbol{J} & h_3\boldsymbol{I} + h_4\boldsymbol{J} \end{bmatrix}^T$ is the feedback gain matrix and

$$\sigma = \begin{cases} 1 \\ 0 \end{cases} \quad if \quad \begin{matrix} v_h = 0 \\ v_h \neq 0 \end{matrix} \quad ,$$

where v_h is the amplitude of the HFSI.

If the proposed observer estimates the EEMF satisfactorily, the QEMF can be computed and used in order to extract the rotor position and speed. Here, the estimation of the mechanical variables is performed through the following adaptation mechanism

$$\varepsilon = -\hat{\boldsymbol{Q}}^{nT}\begin{bmatrix} \cos 2\hat{\theta}_e \\ \sin 2\hat{\theta}_e \end{bmatrix}, \qquad (4.7)$$

where the rotor flux speed is computed by

$$\hat{\omega}_e = \varepsilon\left(k_p + \frac{k_i}{s}\right), \qquad (4.8)$$

and the rotor flux position by

$$\hat{\theta}_e = \frac{\hat{\omega}_e}{s}, \qquad (4.9)$$

where k_p and k_i are the adaptive gains.

The presented rotor position and speed reconstruction method (4.7)-(4.9) is the well known PLL. From (4.7), the necessity of the starting position knowledge for sensorless operation is highlighted (ZHAO; NALAKATH; EMADI, 2019; NALAKATH et al., 2018; SUN et al., 2019), since $2\theta_e = \theta_e$. Once initial rotor position is obtained, the integrative nature of the PLL makes the estimated position to stay aligned to the N pole. Fig. 4.2 illustrate the overall structure of the QEMF based adaptive full-order observer.

The PLL possess a low-pass filter behavior which enables to mitigate the high frequency components that can remain after the demodulation procedure. Furthermore,

Figure 4.2: QEMF base adaptive full-order observer diagram.
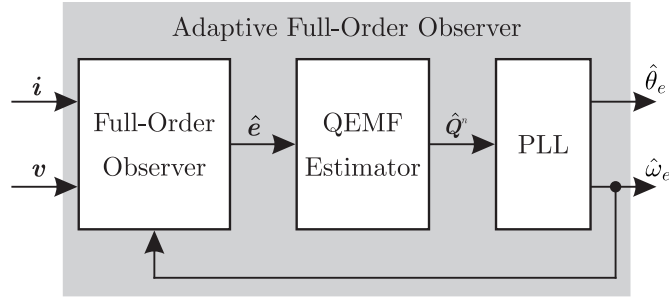
the starting IPMSM position can be set in the PLL due to the integration nature of the algorithm, making unnecessary an additional method to solve $2\theta_e$.

4.3　Design Guidelines for the Adaptive and Feedback Gains

In this section, the gain design concepts of the cascade approach are adapted to the adaptive full-order observer with HFSI. Furthermore, when the EEMF is under effect of HFSI, its dynamics increases due to the q-axis currents derivatives. Therefore, the observer response must be fast enough in order to track the desired variables.

The dynamics of the state observer are given as follows,

$$
\frac{d}{dt}\begin{bmatrix} \tilde{\boldsymbol{i}} \\ \tilde{\boldsymbol{e}} \end{bmatrix} = \underbrace{\begin{bmatrix} h_1\boldsymbol{I}+h_2\boldsymbol{J} & -\frac{\boldsymbol{I}}{L_d} \\ h_3\boldsymbol{I}+h_4\boldsymbol{J} & \boldsymbol{J}\omega_e\sigma \end{bmatrix}}_{\boldsymbol{A}}\begin{bmatrix} \tilde{\boldsymbol{i}} \\ \tilde{\boldsymbol{e}} \end{bmatrix} +
$$
$$
+ \underbrace{\begin{bmatrix} \boldsymbol{0} \\ \boldsymbol{I} \end{bmatrix}}_{\boldsymbol{B}_1}\sigma\boldsymbol{J}\hat{\boldsymbol{e}}\tilde{\omega}_e + \underbrace{\begin{bmatrix} \frac{L_d-L_q}{L_d}\boldsymbol{I} \\ \boldsymbol{0} \end{bmatrix}}_{\boldsymbol{B}_2}\boldsymbol{J}\boldsymbol{i}\tilde{\omega}_e + \underbrace{\begin{bmatrix} \boldsymbol{0} \\ \boldsymbol{I} \end{bmatrix}}_{\boldsymbol{B}_3}\left(1-\sigma\right)\rho\boldsymbol{e}. \tag{4.10}
$$

Since the input of the QEMF estimator is the observed EEMF, the observer output is defined such as

$$
\tilde{\boldsymbol{e}} = \underbrace{\begin{bmatrix} \boldsymbol{0} & \boldsymbol{I} \end{bmatrix}}_{\boldsymbol{C}}\begin{bmatrix} \tilde{\boldsymbol{i}} \\ \tilde{\boldsymbol{e}} \end{bmatrix}. \tag{4.11}
$$

The frequency response of $\boldsymbol{G}_1$ and $\boldsymbol{G}_3$ is given by

$$
\begin{aligned}
\boldsymbol{G}_1\left(s\right) = \boldsymbol{G}_3\left(s\right) &= \boldsymbol{C}[s\boldsymbol{I}-\boldsymbol{A}]^{-1}\boldsymbol{B}_1 \\
&= [s\boldsymbol{I}-(h_1\boldsymbol{I}+h_2\boldsymbol{J})][s^2\boldsymbol{I}+(a_1\boldsymbol{I}+a_2\boldsymbol{J})\,s+a_3\boldsymbol{I}+a_4\boldsymbol{J}]^{-1},
\end{aligned} \tag{4.12}
$$

Figure 4.3: Adaptive full-order observer error block diagram at (a) high-speed (b) HFSI low-speed.

(a)

(b)
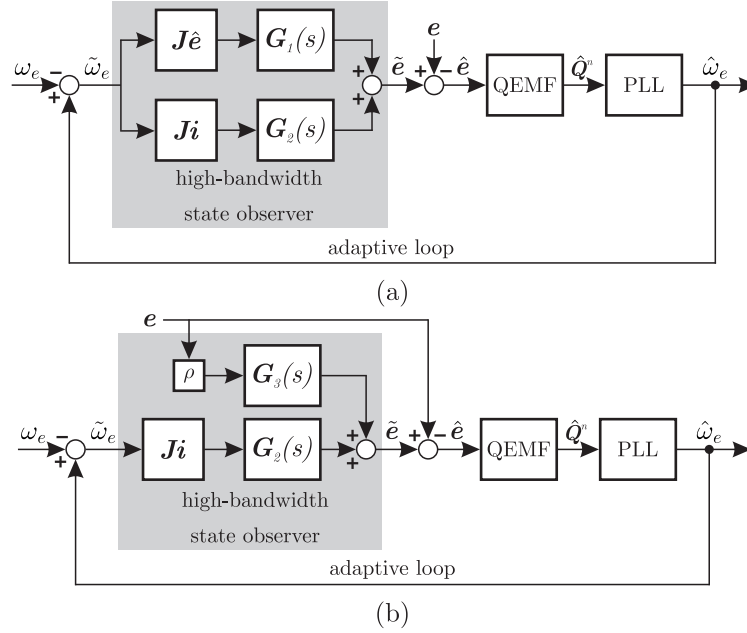
Source: Author.

and $\boldsymbol{G}_2$

$$
\begin{aligned}
\boldsymbol{G}_2\left(s\right) &= \boldsymbol{C}[s\boldsymbol{I} - \boldsymbol{A}]^{-1}\boldsymbol{B}_2 \\
&= [\,L_d{}^{-1}(L_d - L_q)\,(h_3\boldsymbol{I} + h_4\boldsymbol{J})][s^2\boldsymbol{I} + (a_1\boldsymbol{I} + a_2\boldsymbol{J})\,s + a_3\boldsymbol{I} + a_4\boldsymbol{J}]^{-1},
\end{aligned}
\tag{4.13}
$$

where

$$
\begin{cases}
\quad a_1 = -h_1 \\
\quad a_2 = -\omega_e\sigma - h_2 \\
\quad a_3 = \frac{h_3}{L_d} - \sigma\omega_e h_2 \\
\quad a_4 = \frac{h_4}{L_d} + \sigma\omega_e h_1
\end{cases}
\tag{4.14}
$$

The overall adaptive observer error block diagram is presented in Fig. 4.3. At high-speeds, $\sigma = 1$ is set and the full-order observer takes the form of the observer presented in Chapter 3. When HFSI is applied at low-speed, $\sigma = 0$ is obtained and the observer does not match anymore the IPMSM model. The EEMF derivative become the system input and the observer turn into a disturbance type observer.

The pole placement feedback gain design is proposed as follows

$$
\begin{cases}
\quad h_1 = -2\Gamma_1 \\
\quad h_2 = -\hat{\omega}_e\sigma \\
\quad h_3 = L_d\left(\hat{\omega}_e h_2\sigma + \Gamma_1^2\right) \\
\quad h_4 = -L_d\hat{\omega}_e h_1\sigma
\end{cases}
\tag{4.15}
$$

where Γ_1 is the placement of all observer poles.

4.3.1 High-Speed Design

At high-speed, the observer design must be fast enough in order to observe the EEMF fundamental at maximum speed. Furthermore, robustness to speed estimation error is desired and, as obtained in the Chapter 3, increasing the poles frequency achieve this objective. The effects of poles frequency on observer robustness is illustrated in Fig. 4.4. The IPMSM operates at nominal speed and the gains are tuned with $\Gamma_1 = \omega_{e-rated}$ and $\Gamma_1 = 5\omega_{e-rated}$. As the observer with increased bandwidth achieves improved robustness and fast estimation, the design guidelines for high-speed operation should be as high as the sampling frequency permit.

Figure 4.4: State observer normalized poles under speed estimation error with IPMSM at nominal speed, no HFSI and (a) $\Gamma_1 = \omega_{e-rated}$ and (b) $\Gamma_1 = 5\omega_{e-rated}$.
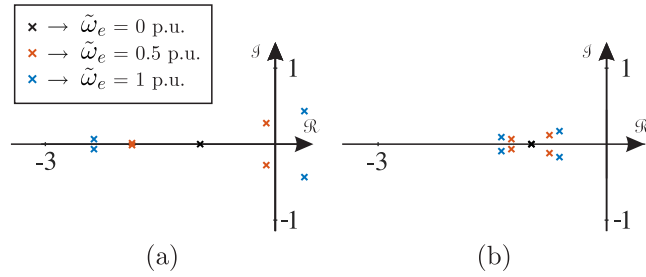
Source: Author.

4.3.2 Low-Speed Design

The observer at low-speed is under the effect of HFSI. This phenomenon increases the EEMF frequency response, requiring high bandwidths for accurate EEMF tracking. Furthermore, the proposed state observer with HFSI does not present the rotor speed in $\boldsymbol{A}$, eliminating the high-speed effects of speed estimation error on the observer stability.

The state-observer with $\sigma = 0$ assumes the form of a disturbance observer. Despite this approach has fewer stability constraints, a random placement of the poles in the left half plane may not guarantee accurate estimation, since the observer does not match the IPMSM model under HFSI. Therefore, the feedback gains should be tuned aiming the reduction of the EEMF derivative impact on EEMF estimation error. Fig. 4.5 demonstrate the bode diagram of the state observer at HFSI low-speed operation. As bandwidth increases, $\boldsymbol{G}_3(s)$ magnitude diminishes, reducing the impact of ρe in the forward path, and consequently, in the observed EEMF. In this way, the observer poles must be set at high values for high-performance EEMF estimation under HFSI.

Figure 4.5: Observer bode diagram as bandwidth increases. (a) $\boldsymbol{G}_3(s)$ and (b) and $\boldsymbol{G}_2(s)$.

(a) (b)
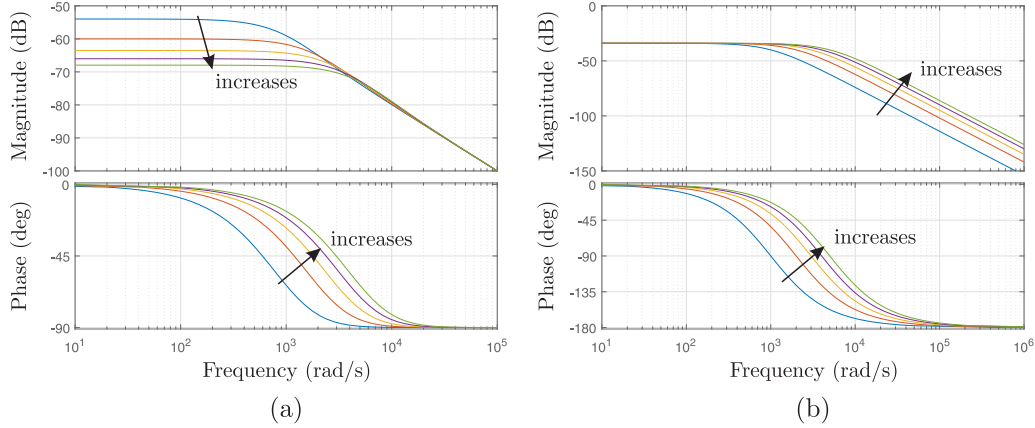
Source: Author.

4.3.3 PLL Design

Finally, the adaptation PLL gains should be fast enough in order to reconstruct the position and speed from the QEMF vector. However, the PLL can not be too fast to respect the cascade design concept and do not impact the state observer design. The PLL frequency response (XIAO et al., 2021) is give by

$$G_{PLL}\left(s\right) = \frac{\hat{\theta}_e}{\theta_e} = \frac{2k_p s + 2k_i}{s^2 + 2k_p s + 2k_i}. \tag{4.16}$$

PLL pole placement can be achieve by the following expression

$$\begin{cases} k_p = \Gamma_2 \\ k_i = \frac{1}{2}\Gamma_2{}^2 \end{cases} \tag{4.17}$$

where Γ_2 is the placement of the PLL poles.

4.4 Comments on the Proposed Estimation Method

In the following are discussed the main design considerations and implementation issues of the proposed algorithm.

1. The bandwidth of the adaptive feedback loop must be selected at lower frequencies so that does not offer additional dynamics to the state observer. However, Γ_2 should be chosen high enough for good estimation of the rotor position and speed dynamics. Thus, the design guidelines for Γ_2 are given as

$$\omega_n \ll \Gamma_2 \ll \Gamma_1. \tag{4.18}$$

2. The state observer must have a fast response so it can observe the EEMF, even with HFSI, and be robust to speed estimation error. As mentioned in Chapter 3, the main limitation of the robustness increase is the sampling time T_s. Here, the Euler discretization is used to define the stability limitation. Therefore, Γ_1 should respect the following expression

$$\omega_{e-\max} \ll \Gamma_1 \ll \frac{2}{T_s}. \tag{4.19}$$

3. The QEMF normalization procedure aims to eliminate the high-frequency components from the QEMF. In practical conditions, measurement noise is expected and can lead to large errors when the normalization is executed at small QEMF values. Thus, the following procedure is performed to reduce this phenomenon

$$\begin{cases} \boldsymbol{Q}^n{}_{(k)} = \boldsymbol{Q}^n{}_{(k-1)} & \quad |\boldsymbol{Q}| \leq q_{\min} \\ \boldsymbol{Q}^n{}_{(k)} = \frac{\boldsymbol{Q}}{|\boldsymbol{Q}|} & if \quad |\boldsymbol{Q}| > q_{\min} \end{cases}, \tag{4.20}$$

where $q_{\min}$ is the minimum acceptable value of $\boldsymbol{Q}$ for position estimation.

4. In the cascade design method proposed in this chapter, Γ_2 adjusts PLL position estimation behavior. For motors which operate in a wide speed range, fixed Γ_2 can be insufficient for both filtering high-frequency components when HFSI is applied and achieving good high-speed estimation. Therefore, a variable Γ_2 may be necessary depending on the application.

5. The $2\theta_e$ is the major drawback of the QEMF model. If the position estimation diverge for a brief moment, it may align to the S pole and cause instability in the sensorless closed-loop control. If this occurs to the EEMF adaptive observer presented in Chapter 3, the observer will realign to the N pole after the error appears.

6. The impacts of parameter variation on the QEMF estimation are investigated in (XIAO et al., 2021). At high-speed, the parameter variation analysis of Chapter 3 remain the same. At HFSI low-speed, the L_d error remains without effect on position estimation. The effects of R and L_q on position estimation are given as follows,

$$\left|\tilde{\theta}_e\right| = \sin^{-1} \frac{\left\|2\tilde{L}_q\omega_e\bar{\boldsymbol{i}}\right\|}{\left\|\bar{M}\right\|} \tag{4.21}$$

and

$$\left|\tilde{\theta}_e\right| = \sin^{-1} \frac{\left\|2\tilde{R}\bar{\boldsymbol{i}}\right\|}{\left\|\bar{M}\right\|} \tag{4.22}$$

where $\bar{M}$ is the average of M and $\bar{\boldsymbol{i}}$ is the average of the $\boldsymbol{i}$ fundamental.

Since $\bar{M}$ is directly related to the variations of ρi_q, it can be increased in order to reduce the parameter effects on position estimation error.

4.5   Experimental Results

The performance of the proposed adaptive full-order observer design method was verified experimentally in an IPMSM sensorless control operation. The IPMSM speed regulation is performed through a field oriented control algorithm with PI controllers. The sensorless algorithm was implemented in an interface with a DSP TMS320F28335, a voltage source inverter (VSI) and a IPMSM. The experimental setup photograph is shown in Fig..2 at Appendix A. Both sampling and inverter switching frequency were set to 10 kHz. The IPMSM parameters are presented in Table 7 at Appendix A. The Euler method is employed for integration of the differential equations of the adaptive observer in discrete-time. An absolute encoder gives the actual rotor position and rotor speed.

Figure 4.6: Steady-state adaptive observer experimental performance with HFSI at $\omega_r = 5$ rad/s.
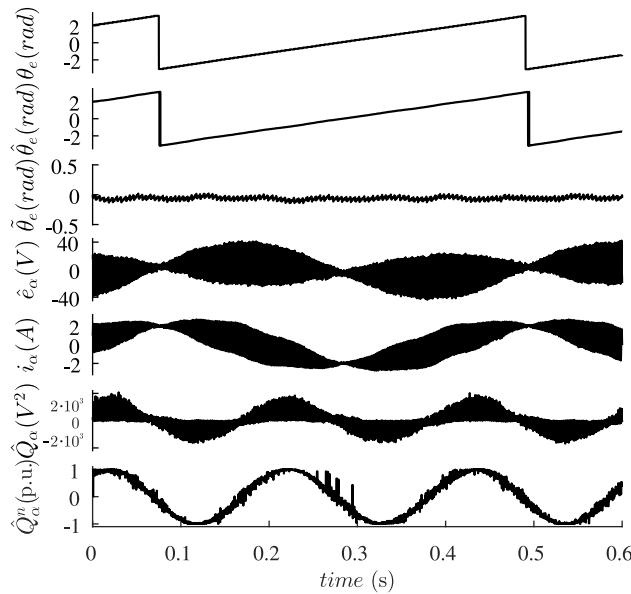
Source: Author.

Due to its easy implementation, the square wave method is chosen as the HFSI algorithm and is applied to the q-axis in order to achieve sufficient ρi_q. The HFSI frequency is set to $f_h = 500$ Hz and the amplitude $v_h = 100$ V. The adaptive observer design are defined with $\Gamma_1 = 5000$ and $\Gamma_2 = 200$, respecting the cascade design guidelines. The QEMF is adjusted with $q_{\min} = 600$. The transition speed for HFSI is set to $\omega_r = 15$ rad/s. Since the estimated rotor speed is an internal state of the PLL, the gains which achieve adequate position estimation performance may not produce adequate speed estimation. Thus, the estimated rotor speed is filtered by a low-pass filter.

Figure 4.7: Adaptive observer HFSI transition experimental results at $\omega_r = 15$ rad/s.
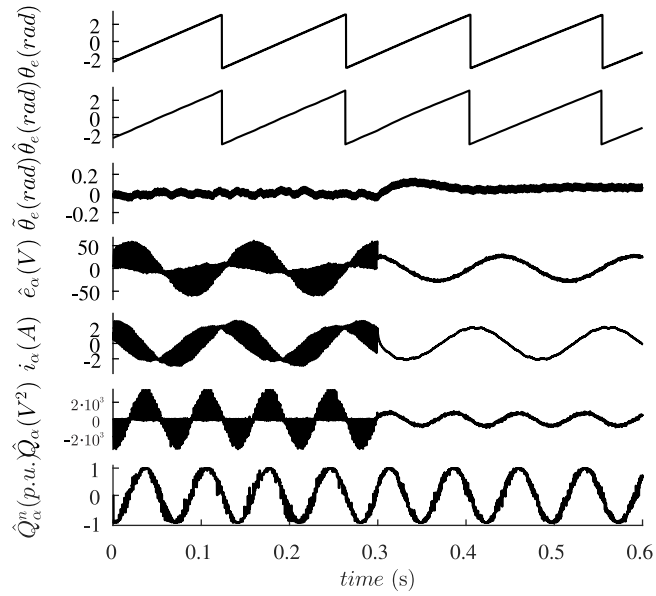
Source: Author.

Figure 4.8: Adaptive observer low-speed experimental results for rotor speed variation.
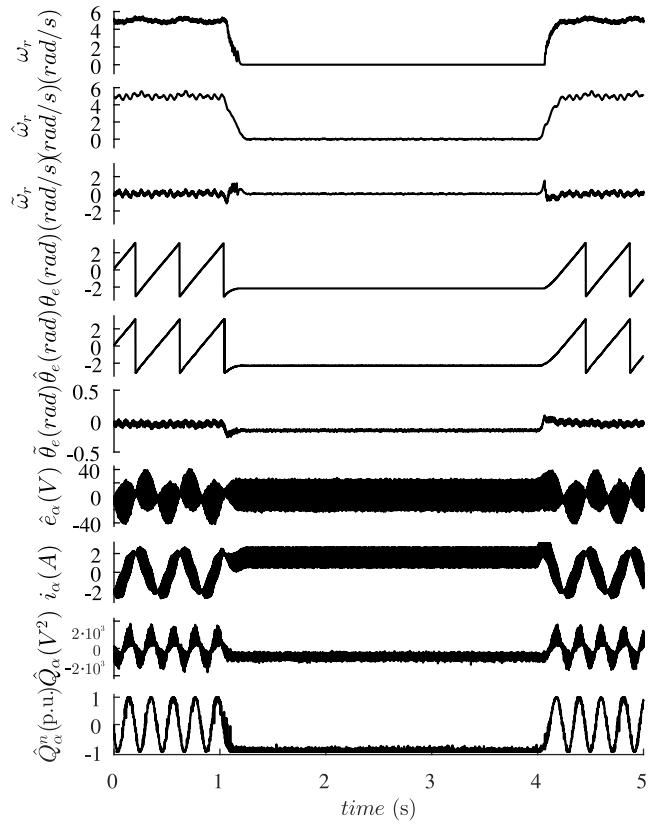
Source: Author.

Figure 4.9: Adaptive observer low-speed experimental results for fast rotor speed reversal.
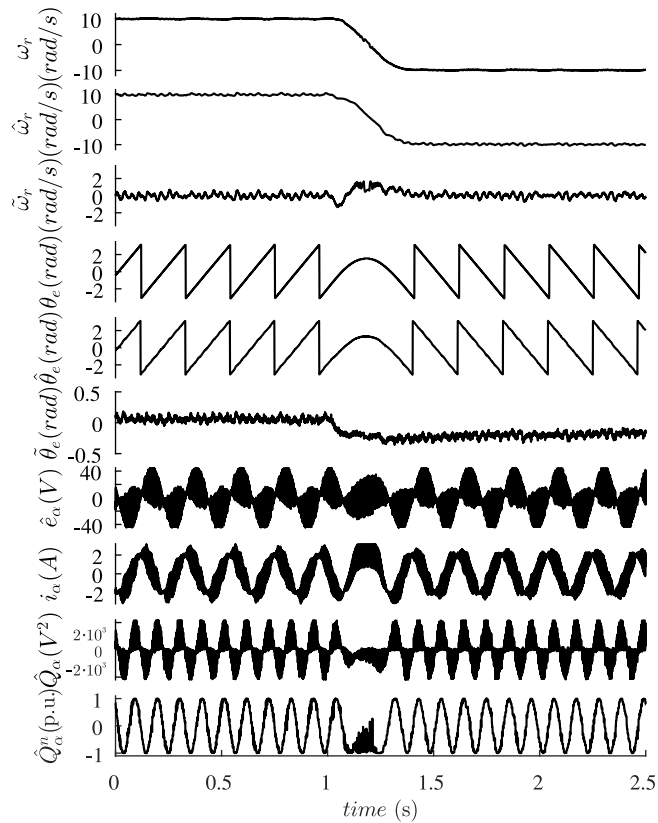
Source: Author.

Figure 4.10: Adaptive observer experimental results for position control.
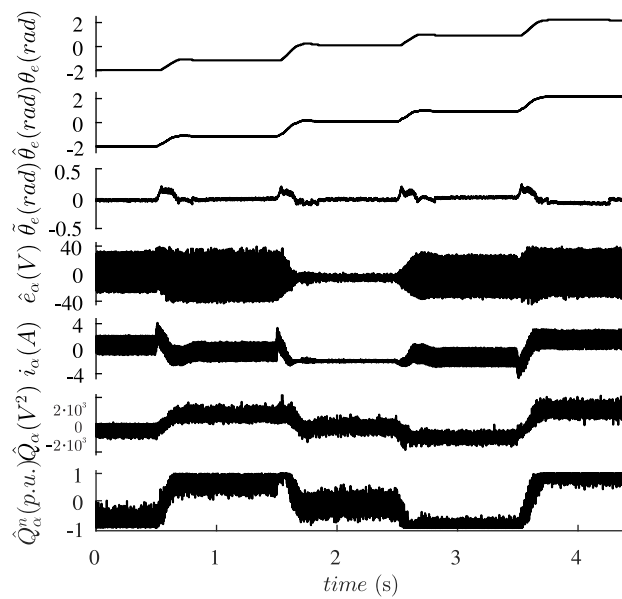
Source: Author.

4.5.1 Low-Speed Sensorless Control

The experimental adaptive full-order observer performance at steady-state is examined, and presented in Fig.4.6 , in order to validate the QEMF demodulation features. The rotor speed is set to $\omega_r = 5$ rad/s. The impact of HFSI on the IPMSM currents and observed EEMF are visible. The normalized QEMF presents a sinusoidal behavior with small noise. The PLL proved capable of filtering the QEMF noise and achieve good position estimation.

Figure 4.11: Adaptive observer experimental results for medium-speed reversal from ω_r = 50 rad/s to ω_r = -50 rad/s.
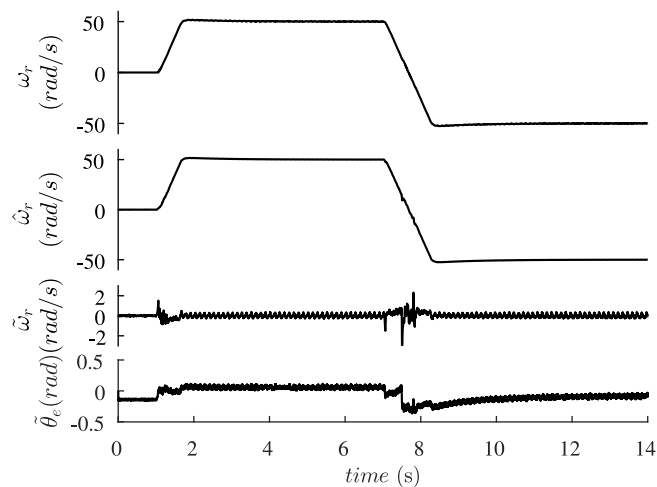
Source: Author.

As the transition between the low-speed to high-speed is of major importance for full-range sensorless control, the position estimation performance when HFSI is disable is investigated in the second experiment and shown in Fig.4.7. The rotor speed is regulated at $\omega_r = 15$ rad/s and the HFSI is disable at 0.3 s. Good position estimation performance is perceived through the transition process.

Rotor speed sensorless control is the subject of the third experiment and is presented at Fig.4.8. The experiment starts with rotor speed at $\omega_r = 5$ rad/s and is change to $\omega_r = 0$ rad/s at 1 s. At 4 s, the rotor speed reference is set to $\omega_r = 5$ rad/s once again. Good rotor speed and position estimation is seen throughout the experiment.

The next experiment, illustrated in Fig.4.9, investigates the adaptive observer performance for fast rotor speed reversal. The IPMSM rotor speed starts with $\omega_r = 10$ rad/s and is switched to $\omega_r = -10$ rad/s at 1.25 s. The adaptive observer reproduces the rotor speed and position properly and achieves satisfactory sensorless control.

The adaptive observer under HFSI enables high-performance low-speed estimation. Therefore, IPMSM sensorless position control is investigated and presented in Fig.4.10. An additional control-loop is added to the rotor speed control-loop and a proportional

Figure 4.12: Adaptive observer experimental results for full-range IPMSM sensorless control.
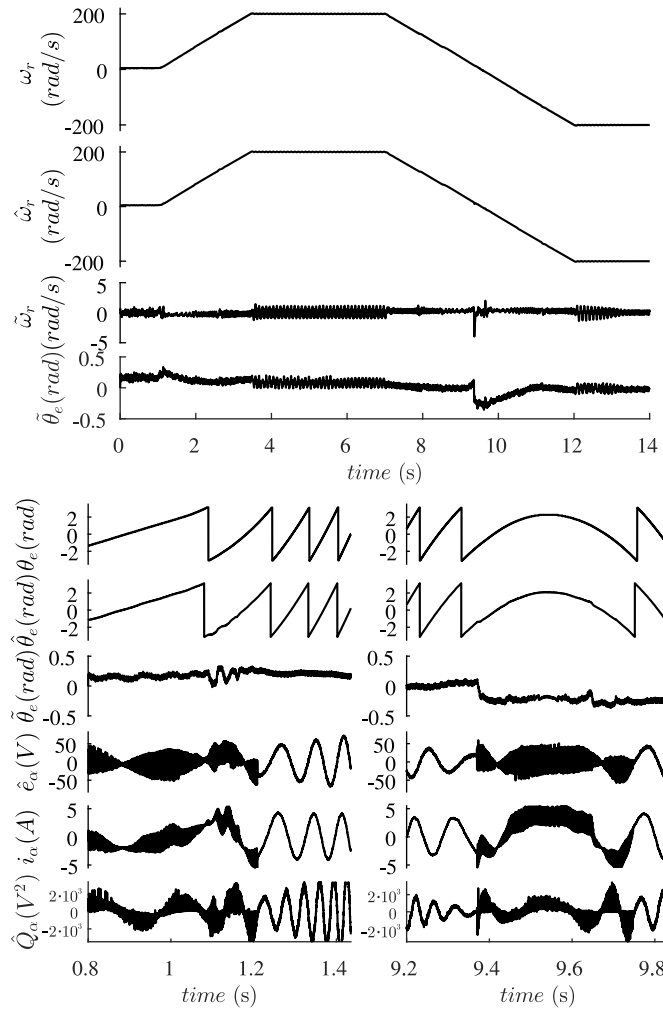
Source: Author.

controller is used. The IPMSM position reference starts with θ_e = -2 rad and 1 rad is added to the reference at 0.5 s and every additional 1 s. As can be seen, the proposed estimation method delivers high-performance position control.

4.5.2   Full-Range Sensorless Control

As the primary objective of the chapter, full-range sensorless control experiments are performed. First, the transition between low to high-speed and high to low-speed sensorless control under speed variation is investigated and presented in Fig. 4.11. The rotor speed starts at ω_r = 0 rad/s and the speed reference is changed to 50 rad/s at 1 s and to -50 rad/s at 7s. The speed variation is 80 rad/s^2. The fast rotor acceleration generates a transitory position estimation error. Nevertheless, the proposed estimation algorithm performs the fast speed transition under sensorless control without losing the

Figure 4.13: Adaptive observer experimental high-speed results with rated load step.
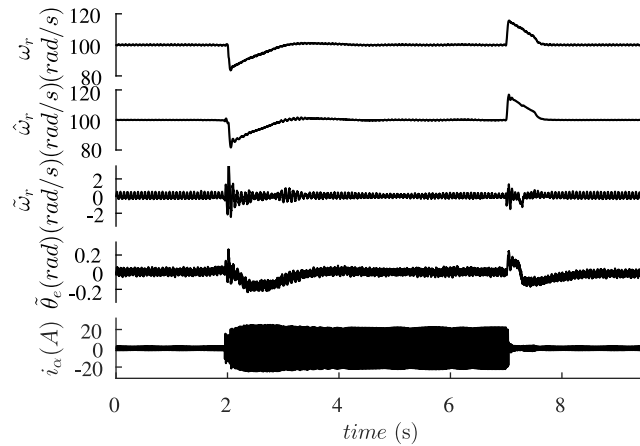
Source: Author.

Figure 4.14: Adaptive observer experimental low-speed results with a fifth of the rated load step.
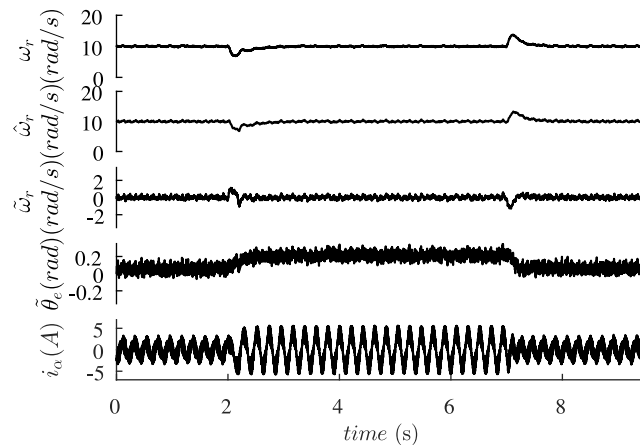
Source: Author.

field orientation.

Full-range sensorless control, from $\omega_r = 200$ rad/s to $\omega_r = $ -200 rad/s, experimental results are illustrated in Fig. 4.12. Once again, the rotor speed acceleration is 80 rad/s^2. As showed by the figure, a transitory position estimation error occurs when HFSI is applied at speed reversal. Furthermore, the adaptive full-order observer maintains its stability throughout the experiment and full-range IPMSM sensorless control is achieved.

The sensorless control algorithm under load operation is investigated. Fig.4.13 presents the estimation algorithm response to rated load step at high-speed operation. Good estimation is perceived throughout the experiment.

The load step response at low-speed HFSI operation is presented in Fig.4.14. The load step is set to a fifth of the rated load and significant error is presented. The same

Figure 4.15: Adaptive observer experimental low-speed results with a fifth of the rated load step and HFSI increase to $v_h = 175$ V.
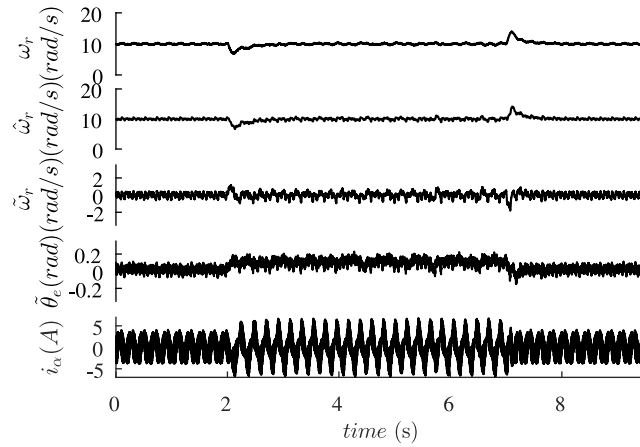
Source: Author.

experiment is reproduced with $v_h = 175$ V and is illustrated in Fig.4.15. The position estimation error step diminishes from $\left|\tilde{\theta}_e\right| = 0.1537$ to $\left|\tilde{\theta}_e\right| = 0.0813$ rad. Although increasing the HFSI reduced the position estimation error variation, it was not possible to keep pushing higher v_h and load conditions with q-axis signal injection due to VSI limitations.

Figure 4.16: Adaptive observer experimental low-speed steady-state results with d-axis HFSI.
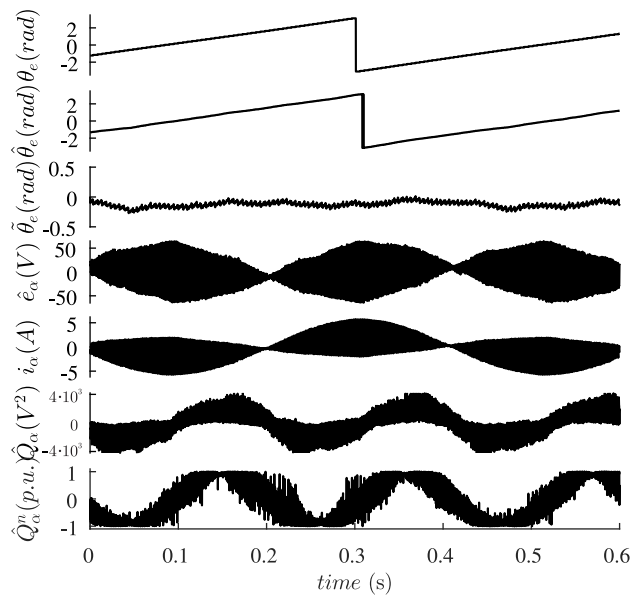
Source: Author.

4.5.3   Investigation of d-axis HFSI

The QEMF at HFSI low-speed is primarily excited by ρi_q. However, as demonstrated in Chapter 2 that d-axis HFSI is preferred over q-axis HFSI, d-axis HFSI is experimentally investigated. The HFSI is first set to $f_h = 500$ Hz and $v_h = 100$ V for comparison with the q-axis method. The steady-state adaptive observer performance with d-axis HFSI is demonstrated in Fig. 4.16. Similar response between q-axis and d-axis HFSI is achieve but a 90 degree shift on the PLL was required.

In order to explore the maximum load step attainable with d-axis HFSI, the voltage was increased to $v_h = 175$ V. The load step is set to 70 % of the rated load and this experiment is presented in Fig. 4.17. A visible error appears when shaft load is applied. However, IPMSM sensorless control at low-speed is obtained at high-load conditions.

Figure 4.17: Adaptive observer experimental low-speed results with 70% of the rated load step and d-axis HFSI.
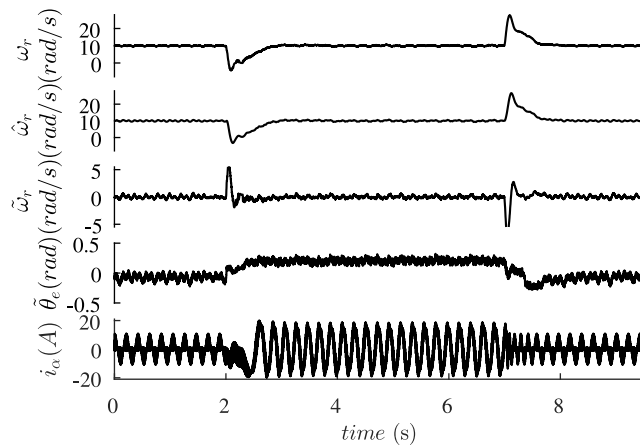
Source: Author.

4.6   Chapter Conclusion

This chapter presented a rotor speed estimation method for full-range sensorless IPMSM drives based on the adaptive full-order observer. The adaptive observer presented in the Chapter 3 is modified in order to achieve EEMF observation under HFSI. QEMF variables are constructed built from the observed EEMF for rotor position observability through the entire operation area. The cascade design strategy is adapted to the modified adaptive full-order observer and feedback and adaptive gains are proposed. The PLL presents low-pass filter features for good rotor speed end position estimation. Through the presented design guidelines, the tuning of the adaptive observer is reduced to two intuitive design variables. Experimental results are provided for validation of the proposed adaptive full-order observer for full-range IPMSM sensorless control.

5   CONCLUSION

5.1   Thesis Conclusion

This Thesis presented an adaptive full-order observer design method for rotor position and speed estimation aiming full-range sensorless IPMSM drives. The gain design methodology sought to simplify the tuning procedure by reducing the high number of gains in intuitive design variables. In this way, the rotor position and speed estimation algorithm can be generalized for a large range of motors. Furthermore, due to the nature of the EEMF model, the presented procedure can be extended for SynRM for full-range sensorless control and for SPMSM for high-speed sensorless control.

More specifically, Chapter 2 presented a deep literature review on position sensorless control for IPMSM drives. In this review, the main IPMSM models for position estimation are investigated and the major observer methods for high-performance estimation are presented. The performance characteristics, stability constraints and gain design complexity are also discussed. Furthermore, recent research aiming high-performance position estimation under non-ideal conditions are presented. This research includes estimation under low f_{ratio}, sensorless parameter estimation and frequency adaptive observers. Furthermore, the main position estimation frameworks with HFSI for low-speed estimation are investigated. The integration of the high-speed and low-speed methods for full-range IPMSM sensorless control are also presented.

In Chapter 3, it was presented an adaptive full-order observer analysis and design for sensorless IPMSM drives based on the EEMF model. This sensorless strategy aims good performance at medium and high speed operation. First, the IPMSM model in the synchronous reference frame is presented and is manipulated in order to create the EEMF mode in the stationary reference frame. The linear EEMF is a generalization of the traditional EMF model for all synchronous sinusoidal machines. An adaptive full-order observer for rotor position and speed estimation is proposed for the sensorless algorithm. This type of algorithm has multiple gains, feedback and adaptive, which need to be precisely adjusted. It is investigated that the state observer stability is subject to speed estimation error. Therefore, a cascade design is proposed for the proposed estimation method. In this approach, the state observer is designed with high bandwidth, which increase the robustness of the observer for speed estimation error. Furthermore, the adaptive loop is easily modeled due to the lack of dynamics that the state observer generates and an unified first order filter response is obtained. Effects of parameter variation on position and speed estimation were investigated. It is concluded that no parameter influences the speed estimation. However, the position estimation is significantly affected by the L_q parameter error. The proposed design and analysis is verified experimentally in a 11 kW IPMSM.

In Chapter 4, the adaptive full-order observer presented in Chapter 3 is modified for operation with HFSI and achieve full-range IPMSM sensorless control. First, the recent developed in the literature QEMF is presented. This new variable enable the unified position estimation and HFSI is used in order to achieve position observability under low-speed. Modifications on the adaptive observer are proposed and the PLL is employed for rotor position and speed estimation. Cascade design guidelines are provided in order to simplify the design procedure into two simple tuning variables. The PLL low-pass filter behavior reduces the high-frequency residual from the QEMF components. Experimental results validate the proposed design method.

5.2   Thesis Contributions

The main contributions of the Thesis are summarized as follows,

- A straightforward design method for the adaptive full-order observer applied to the estimation of rotor position and speed for high speed sensorless IPMSM drives is presented;

- The stability constraints of the adaptive full-order observer are investigated. Through the proposed cascade design method, the estimation method robustness for speed estimation error are improved;

- An analysis of the parameter error effects on position and speed estimation is performed.

- The adaptive full-order observer is adapted to execute position estimation through the QEMF and HFSI. In this way, it is possible to achieve universal sensorless control.

5.3   Future Work

While the sensorless IPMSM control techniques have been studied from decades ago to now, improvements can still be performed in the existing algorithms. This section examines the future trends in this topic.

- From the new PMSM sensorless research topics presented in chapter II, the operation under low f_{ratio} has the fewest studies. The current design algorithms still lack of robustness analysis tools and, since the full-order observer is shown to have its stability dependent on the actual rotor speed, the discrete-time observer design should evaluate the robustness in relation to speed estimation error. Thus, it will be possible to evaluate and extract the lowest f_{ratio} for each operation point. The analysis of the effects of the sampling frequency on the rotor position and speed

estimation, similarly to the parameter variation analysis already presented in the literature, should also be performed. Furthermore, motors with rated speed up to 100 krpm are presented in the literature, which increases the interest in improvements for the estimation under low f_{ratio}.

- As demonstrated in this Thesis, the increase in the observer bandwidth expand the system robustness to speed estimation error. However, adaptive bandpass observer can not change its bandwidth, which is set to be related with the operation speed for adequate filtering. Therefore, improvements in robustness for the adaptive bandpass observer is also a subject to be investigated.

- The QEMF variables enable the use of arbitrary HFSI types, permitting choose the HFSI method that best suits the IPMSM application. However, studies on the types of HFSI and their effects on the resulting torque, audible noise and rotor position observability of the IPMSM are limited. Thus, a deep investigation of the HFSI and its effects on the QEMF are highly demanded.

- Parameter estimation under sensorless control is usually only executed for resistance variation. Since HFSI is used for low-speed estimation, it can also be adopted to estimate and map the L_q variation under load conditions and cancel its effects on position estimation.

5.4 Published Journal Articles

The contributions performed throughout the doctorate were released in prestigious academic journals. The articles written during the doctorate are specified below.

5.4.1 Thesis Related Journal Articles

- **C. J. V. Filho**, D. Xiao, R. P. Vieira and A. Emadi, ”Observers for High-Speed Sensorless PMSM Drives: Design Methods, Tuning Challenges and Future Trends,” in **IEEE Access**, vol. 9, pp. 56397-56415, 2021, doi: 10.1109/ACCESS.2021.3072360.

- **C. J. Volpato Filho** and R. P. Vieira, ”Adaptive Full-Order Observer Analysis and Design for Sensorless Interior Permanent Magnet Synchronous Motors Drives,” in **IEEE Transactions on Industrial Electronics**, vol. 68, no. 8, pp. 6527-6536, Aug. 2021, doi: 10.1109/TIE.2020.3007101.

5.4.2 Other Journal Articles

- **Volpato Filho, C.J.**, Vieira, R.P. Pole Placement Design Methodology of Back-EMF Adaptive Observer for Sensorless PMSM Drives. **J Control Autom Electr Syst** 31, 84–93 (2020), doi: 10.1007/s40313-019-00539-x.

- **Volpato Filho, C.J.**, Vieira, R.P. Fast Parameter Estimation for Adaptive Maximum Torque Per Ampere Control of Interior Permanent Magnet Synchronous Motor Drives. **J Control Autom Electr Syst** 32, 992–1001 (2021), doi: 10.1007/s40313-021-00723-y.

- Rocha, L.R., Araujo, M.B., Silva, E.C., Scher, L.H.O., **Volpato Filho, C.J.**, Vieira, R.P. Speed and Position Observer for Non-sinusoidal PMSM Based on a PSD+PLL Structure. **J Control Autom Electr Syst** (2021), doi: 10.1007/s40313-021-00811-z.

REFERENCES

ALMARHOON, A. H.; ZHU, Z. Q.; XU, P. Improved rotor position estimation accuracy by rotating carrier signal injection utilizing zero-sequence carrier voltage for dual three-phase pmsm. **IEEE Transactions on Industrial Electronics**, v. 64, n. 6, p. 4454–4462, 2017.

AN, Q. et al. Frequency-adaptive complex-coefficient filter-based enhanced sliding mode observer for sensorless control of permanent magnet synchronous motor drives. **IEEE Transactions on Industry Applications**, v. 56, n. 1, p. 335–343, 2020.

_____. Quasi-proportional-resonant controller based adaptive position observer for sensorless control of pmsm drives under low carrier ratio. **IEEE Transactions on Industrial Electronics**, v. 67, n. 4, p. 2564–2573, 2020.

ANDREESCU, G. et al. Combined flux observer with signal injection enhancement for wide speed range sensorless direct torque control of ipmsm drives. **IEEE Transactions on Energy Conversion**, v. 23, n. 2, p. 393–402, 2008.

ANNEX, E. E. M. S. **Police guidelines for motor driven units**. [S.l.: s.n.], 2016.

AUGER, F. et al. Industrial applications of the kalman filter: A review. **IEEE Transactions on Industrial Electronics**, IEEE, v. 60, n. 12, p. 5458–5471, 2013. ISSN 02780046.

AWAN, H. A. A. et al. Discrete-time observer design for sensorless synchronous motor drives. **IEEE Transactions on Industry Applications**, v. 52, n. 5, p. 3968–3979, 2016.

BAO, D. et al. Adaptive Synchronous-Frequency Tracking-Mode Observer for the Sensorless Control of a Surface PMSM. **IEEE Transactions on Industry Applications**, v. 54, n. 6, p. 6460–6471, 2018. ISSN 00939994.

BARATIERI, C. L.; PINHEIRO, H. Sensorless vector control for pm brushless motors with nonsinusoidal back-emf. In: **2014 International Conference on Electrical Machines (ICEM)**. [S.l.: s.n.], 2014. p. 915–921.

_____. New variable gain super-twisting sliding mode observer for sensorless vector control of nonsinusoidal back-emf pmsm. **Control Engineering Practice**, v. 52, p. 59 – 69, 2016. ISSN 0967-0661.

BERNARDES, T. et al. Discrete-time sliding mode observer for sensorless vector control of permanent magnet synchronous machine. **IEEE Transactions on Industrial Electronics**, v. 61, n. 4, p. 1679–1691, 2014.

BILGIN, B. et al. Modeling and analysis of electric motors: State-of-the-art review. **IEEE Transactions on Transportation Electrification**, v. 5, n. 3, p. 602–617, 2019.

BLAABJERG, F.; MA, K. Future on power electronics for wind turbine systems. **IEEE Journal of Emerging and Selected Topics in Power Electronics**, v. 1, n. 3, p. 139–152, 2013.

BOLDEA, I.; PAICU, M. C.; ANDREESCU, G. Active flux concept for motion-sensorless unified ac drives. **IEEE Transactions on Power Electronics**, v. 23, n. 5, p. 2612–2618, 2008.

BOLOGNANI, S.; CALLIGARO, S.; PETRELLA, R. Design issues and estimation errors analysis of back-emf-based position and speed observer for spm synchronous motors. **IEEE Journal of Emerging and Selected Topics in Power Electronics**, v. 2, n. 2, p. 159–170, 2014.

BOLOGNANI, S.; OBOE, R.; ZIGLIOTTO, M. Sensorless full-digital pmsm drive with ekf estimation of speed and rotor position. **IEEE Transactions on Industrial Electronics**, v. 46, n. 1, p. 184–191, Feb 1999.

BOLOGNANI, S. et al. Model Sensitivity of Fundamental-Frequency-Based Position Estimators for Sensorless PM and Reluctance Synchronous Motor Drives. **IEEE Transactions on Industrial Electronics**, v. 65, n. 1, p. 77–85, 2018. ISSN 02780046.

BOLOGNANI, S.; TUBIANA, L.; ZIGLIOTTO, M. Ekf-based sensorless ipm synchronous motor drive for flux-weakening applications. **IEEE Transactions on Industry Applications**, v. 39, n. 3, p. 768–775, 2003.

_____. Extended kalman filter tuning in sensorless pmsm drives. **IEEE Transactions on Industry Applications**, v. 39, n. 6, p. 1741–1747, 2003.

BOYD, S.; SASTRY, S. Necessary and sufficient conditions for parameter convergence in adaptive control. **Automatica**, v. 22, n. 6, p. 629 – 639, 1986. ISSN 0005-1098.

BUI, M. X. et al. A modified sensorless control scheme for interior permanent magnet synchronous motor over zero to rated speed range using current derivative measurements. **IEEE Transactions on Industrial Electronics**, v. 66, n. 1, p. 102–113, Jan 2019.

CAO, R.; JIANG, N.; LU, M. Sensorless control of linear flux-switching permanent magnet motor based on extended kalman filter. **IEEE Transactions on Industrial Electronics**, v. 67, n. 7, p. 5971–5979, 2020.

CAPOLINO, G.; CAVAGNINO, A. New trends in electrical machines technology—part ii. **IEEE Transactions on Industrial Electronics**, v. 61, n. 9, p. 4931–4936, Sep. 2014.

CHEN, G.-R. et al. Position and speed estimation of permanent magnet machine sensorless drive at high speed using an improved phase-locked loop. **Energies**, v. 10, p. 1571, 10 2017.

CHEN, T. et al. Improved-Reduced Order Generalized Integrator Based Sliding-Mode Observer for Interior Permanent Magnet Synchronous Motor Sensorless Control. In: **2019 22nd International Conference on Electrical Machines and Systems, ICEMS 2019**. [S.l.: s.n.], 2019. ISBN 9781728133980.

CHEN, W. H. et al. Disturbance-observer-based control and related methods an overview. **IEEE Transactions on Industrial Electronics**, v. 63, n. 2, p. 1083–1095, Feb 2016. ISSN 0278-0046.

CHEN, Z. et al. An extended electromotive force model for sensorless control of interior permanent-magnet synchronous motors. **IEEE Transactions on Industrial Electronics**, v. 50, n. 2, p. 288–295, Apr 2003. ISSN 0278-0046.

CHI, S.; ZHANG, Z.; XU, L. Sliding-mode sensorless control of direct-drive pm synchronous motors for washing machine applications. **IEEE Transactions on Industry Applications**, v. 45, n. 2, p. 582–590, 2009.

CHOI, J. et al. Robust Adaptive Sensorless Control for Permanent-Magnet Synchronous Motors. **IEEE Transactions on Power Electronics**, v. 32, n. 5, p. 3989–3997, 2017. ISSN 08858993.

CONSOLI, A. et al. Sensorless vector and speed control of brushless motor drives. **IEEE Transactions on Industrial Electronics**, v. 41, n. 1, p. 91–96, 1994.

CORLEY, M.; LORENZ, R. Rotor position and velocity estimation for a salient-pole permanent magnet synchronous machine at standstill and high speeds. **IEEE Transactions on Industry Applications**, v. 34, n. 4, p. 784–789, 1998.

CORRADINI, M. et al. Speed estimation and fault detection for pmsm via quasi sliding modes. **IFAC Proceedings Volumes**, v. 44, n. 1, p. 6142–6147, 2011. ISSN 1474-6670. 18th IFAC World Congress.

DAROUACH, M.; ZASADZINSKI, M.; XU, S. J. Full-order observers for linear systems with unknown inputs. **IEEE Transactions on Automatic Control**, v. 39, n. 3, p. 606–609, 1994.

DAVOINE, J.; PERRET, R.; LE-HUY, H. Operation of a self-controlled synchronous motor without a shaft position sensor. **IEEE Transactions on Industry Applications**, IA-19, n. 2, p. 217–222, 1983.

DING, L.; LI, Y. W.; ZARGARI, N. R. Discrete-time smo sensorless control of current source converter-fed pmsm drives with low switching frequency. **IEEE Transactions on Industrial Electronics**, v. 68, n. 3, p. 2120–2129, 2021.

DING, L. et al. Sensorless control of csc-fed pmsm drives with low switching frequency for electrical submersible pump application. **IEEE Transactions on Industry Applications**, v. 56, n. 4, p. 3799–3808, 2020.

EV-VOLUMES.COM. **Global EV Sales for 2018 - Final Results**. [S.l.: s.n.], 2018.

FILHO, C. J. V. et al. Adaptive observer for sensorless permanent magnet synchronous machines with online pole placement. In: **2017 Brazilian Power Electronics Conference (COBEP)**. [S.l.: s.n.], 2017. p. 1–6.

FILHO, C. J. V.; VIEIRA, R. P. Adaptive full-order observer analysis and design for sensorless interior permanent magnet synchronous motors drives. **IEEE Transactions on Industrial Electronics**, p. 1–1, 2020.

FOO, G.; RAHMAN, M. F. Sensorless sliding-mode mtpa control of an ipm synchronous motor drive using a sliding-mode observer and hf signal injection. **IEEE Transactions on Industrial Electronics**, v. 57, n. 4, p. 1270–1278, 2010.

_____. Sensorless sliding-mode MTPA control of an IPM synchronous motor drive using a sliding-mode observer and HF signal injection. **IEEE Transactions on Industrial Electronics**, v. 57, n. 4, p. 1270–1278, 2010. ISSN 02780046.

FOO, G. H. B.; ZHANG, X.; VILATHGAMUWA, D. M. A sensor fault detection and isolation method in interior permanent-magnet synchronous motor drives based on an extended kalman filter. **IEEE Transactions on Industrial Electronics**, v. 60, n. 8, p. 3485–3495, 2013.

GABRIEL, F. et al. High-frequency issues using rotating voltage injections intended for position self-sensing. **IEEE Transactions on Industrial Electronics**, v. 60, n. 12, p. 5447–5457, 2013.

GOLESTAN, S.; GUERRERO, J. M.; GHAREHPETIAN, G. B. Five Approaches to Deal With Problem of DC Offset in Phase-Locked Loop Algorithms: Design Considerations and Performance Evaluations. **IEEE Transactions on Power Electronics**, v. 31, n. 1, p. 648–661, 2016. ISSN 08858993.

GOLESTAN, S. et al. Single-phase frequency-locked loops: A comprehensive review. **IEEE Transactions on Power Electronics**, v. 34, n. 12, p. 11791–11812, 2019. ISSN 19410107.

_____. Modeling, Tuning, and Performance Comparison of Second-Order-Generalized-Integrator-Based FLLs. **IEEE Transactions on Power Electronics**, v. 33, n. 12, p. 10229–10239, 2018. ISSN 08858993.

_____. A Critical Examination of Frequency-Fixed Second-Order Generalized Integrator-Based Phase-Locked Loops. **IEEE Transactions on Power Electronics**, v. 32, n. 9, p. 6666–6672, 2017. ISSN 08858993.

GONG, C. et al. An improved delay-suppressed sliding-mode observer for sensorless vector-controlled PMSM. **IEEE Transactions on Industrial Electronics**, v. 67, n. 7, p. 5913–5923, 2020. ISSN 15579948.

GUDE, S.; CHU, C. C.; VEDULA, S. V. Recursive Implementation of Multiple Delayed Signal Cancellation Operators and Their Applications in Prefiltered and In-Loop Filtered PLLs under Adverse Grid Conditions. In: **IEEE Transactions on Industry Applications**. [S.l.: s.n.], 2019. v. 55, n. 5, p. 5383–5394. ISSN 19399367.

HASEGAWA, M.; MATSUI, K. Ipmsm position sensorless drives using robust adaptive observer on stationary reference frame. **IEEJ Transactions on Electrical and Electronic Engineering**, v. 3, n. 1, p. 120–127, 2008.

_____. Position sensorless control for interior permanent magnet synchronous motor using adaptive flux observer with inductance identification. **IET Electric Power Applications**, v. 3, n. 3, p. 209–217, 2009.

HASEGAWA, M.; YOSHIOKA, S.; MATSUI, K. Position sensorless control of interior permanent magnet synchronous motors using unknown input observer for high-speed drives. **IEEE Transactions on Industry Applications**, v. 45, n. 3, p. 938–946, 2009.

HEJNY, R. W.; LORENZ, R. D. Evaluating the practical low-speed limits for back-EMF tracking-based sensorless speed control using drive stiffness as a key metric. **IEEE Transactions on Industry Applications**, v. 47, n. 3, p. 1337–1343, 2011. ISSN 00939994.

HINKKANEN, M. et al. Observers for sensorless synchronous motor drives: Framework for design and analysis. **IEEE Transactions on Industry Applications**, v. 54, n. 6, p. 6090–6100, Nov 2018. ISSN 0093-9994.

_____. A combined position and stator-resistance observer for salient pmsm drives: Design and stability analysis. **IEEE Transactions on Power Electronics**, v. 27, n. 2, p. 601–609, 2012.

HUTTERER, P. et al. A study on systematic errors concerning rotor position estimation of PMSM based on back emf voltage observation. In: **2009 IEEE International Electric Machines and Drives Conference, IEMDC '09**. [S.l.: s.n.], 2009. p. 1393–1400. ISBN 9781424442522.

ICHIKAWA, S. et al. Sensorless control of permanent-magnet synchronous motors using online parameter identification based on system identification theory. **IEEE Transactions on Industrial Electronics**, v. 53, n. 2, p. 363–372, 2006. ISSN 02780046.

_____. Sensorless control of synchronous reluctance motors based on extended emf models considering magnetic saturation with online parameter identification. **IEEE Transactions on Industry Applications**, v. 42, n. 5, p. 1264–1274, 2006.

IEA. **Energy-Efficiency Policy Opportunities for Electric Motor-Driven Systems**. [S.l.: s.n.], 2011.

_____. **Global EV Outlook 2017**. [S.l.: s.n.], 2017.

_____. **World Energy Outlook 2018**. [S.l.: s.n.], 2018.

IIZUKA, K. et al. Microcomputer control for sensorless brushless motor. **IEEE Transactions on Industry Applications**, IA-21, n. 3, p. 595–601, 1985.

IM, J.; KIM, R. Improved saliency-based position sensorless control of interior permanent-magnet synchronous machines with single dc-link current sensor using current prediction method. **IEEE Transactions on Industrial Electronics**, v. 65, n. 7, p. 5335–5343, 2018.

INOUE, Y. et al. Performance improvement of sensorless IPMSM drives in a low-speed region using online parameter identification. **IEEE Transactions on Industry Applications**, IEEE, v. 47, n. 2, p. 798–804, 2011. ISSN 00939994.

_____. Effectiveness of voltage error compensation and parameter identification for model-based sensorless control of IPMSM. **IEEE Transactions on Industry Applications**, IEEE, v. 45, n. 1, p. 213–221, 2009. ISSN 00939994.

IOANNOU, P. A.; SUN, J. **Robust Adaptive Control**. Upper Saddle River, NJ, USA: Prentice-Hall, Inc., 1995. ISBN 0-13-439100-4.

JANG, J.-H. et al. Sensorless drive of surface-mounted permanent-magnet motor by high-frequency signal injection based on magnetic saliency. **IEEE Transactions on Industry Applications**, v. 39, n. 4, p. 1031–1039, 2003.

Ji-Hoon Jang et al. Analysis of permanent-magnet machine for sensorless control based on high-frequency signal injection. **IEEE Transactions on Industry Applications**, v. 40, n. 6, p. 1595–1604, 2004.

JI, J. et al. Sensorless Control of Linear Vernier Permanent-Magnet Motor Based on Improved Mover Flux Observer. **IEEE Transactions on Power Electronics**, v. 35, n. 4, p. 3869–3877, 2020. ISSN 19410107.

JIANG, Y.; XU, W.; MU, C. Improved SOIFO-based rotor flux observer for PMSM sensorless control. In: **Proceedings IECON 2017 - 43rd Annual Conference of the IEEE Industrial Electronics Society**. [S.l.: s.n.], 2017. v. 2017-January, p. 8219–8224. ISBN 9781538611272.

JIANG, Y. et al. An Improved Third-Order Generalized Integral Flux Observer for Sensorless Drive of PMSMs. **IEEE Transactions on Industrial Electronics**, v. 66, n. 12, p. 9149–9160, 2019. ISSN 15579948.

KIM, D. et al. Suppression of injection voltage disturbance for high-frequency square-wave injection sensorless drive with regulation of induced high-frequency current ripple. **IEEE Transactions on Industry Applications**, v. 52, n. 1, p. 302–312, 2016. ISSN 00939994.

KIM, H. et al. A novel method for initial rotor position estimation for ipm synchronous machine drives. **IEEE Transactions on Industry Applications**, v. 40, n. 5, p. 1369–1378, 2004.

KIM, H.; SON, J.; LEE, J. A high-speed sliding-mode observer for the sensorless speed control of a pmsm. **IEEE Transactions on Industrial Electronics**, v. 58, n. 9, p. 4069–4077, 2011.

KIM, S.; HA, J.; SUL, S. Pwm switching frequency signal injection sensorless method in ipmsm. **IEEE Transactions on Industry Applications**, v. 48, n. 5, p. 1576–1587, 2012.

KIM, S.-I. et al. A new rotor position estimation method of ipmsm using all-pass filter on high-frequency rotating voltage signal injection. **IEEE Transactions on Industrial Electronics**, v. 63, n. 10, p. 6499–6509, 2016.

KIVANC, O. C.; OZTURK, S. B. Sensorless PMSM Drive Based on Stator Feedforward Voltage Estimation Improved with MRAS Multiparameter Estimation. **IEEE/ASME Transactions on Mechatronics**, IEEE, v. 23, n. 3, p. 1326–1337, 2018. ISSN 10834435.

KOTEICH, M. et al. Discussion on "ac drive observability analysis". **IEEE Transactions on Industrial Electronics**, v. 62, n. 11, p. 7224–7225, 2015.

KRISHNAN, R. **Permanent Magnet Synchronous and Brushless DC Motor Drives**. [S.l.]: CRC Press, 2009.

KSHIRSAGAR, P. et al. Implementation and sensorless vector-control design and tuning strategy for smpm machines in fan-type applications. **IEEE Transactions on Industry Applications**, v. 48, n. 6, p. 2402–2413, Nov 2012.

LARA, J.; CHANDRA, A.; XU, J. Integration of hfsi and extended-emf based techniques for pmsm sensorless control in hev/ev applications. In: **IECON 2012 - 38th Annual Conference on IEEE Industrial Electronics Society**. [S.l.: s.n.], 2012. p. 3688–3693.

LEE, H.; LEE, J. Design of iterative sliding mode observer for sensorless PMSM control. **IEEE Transactions on Control Systems Technology**, IEEE, v. 21, n. 4, p. 1394–1399, 2013. ISSN 10636536.

LEVANT, A.; LEVANTOVSKY, L. Sliding order and sliding accuracy in sliding mode control. **International Journal of Control - INT J CONTR**, v. 58, p. 1247–1263, 12 1993.

LI, B.; LI, L. New integration algorithms for flux estimation of ac machines. In: **2011 International Conference on Electrical Machines and Systems**. [S.l.: s.n.], 2011. p. 1–5.

LI, K.; WANG, Y. Maximum torque per ampere (mtpa) control for ipmsm drives based on a variable-equivalent-parameter mtpa control law. **IEEE Transactions on Power Electronics**, v. 34, n. 7, p. 7092–7102, 2019.

LIANG, D.; LI, J.; QU, R. Sensorless control of permanent magnet synchronous machine based on second-order sliding-mode observer with online resistance estimation. **IEEE Transactions on Industry Applications**, v. 53, n. 4, p. 3672–3682, 2017.

LIANG, D. et al. Adaptive second-order sliding-mode observer for pmsm sensorless control considering vsi nonlinearity. **IEEE Transactions on Power Electronics**, v. 33, n. 10, p. 8994–9004, Oct 2018.

LIANG, Y. et al. Robust dc-link voltage control and discrete-time sensorless control for high-speed flywheel energy storage system. In: **2020 International Conference on Electrical Machines (ICEM)**. [S.l.: s.n.], 2020. v. 1, p. 2457–2463.

LIU, J. M.; ZHU, Z. Q. Novel sensorless control strategy with injection of high-frequency pulsating carrier signal into stationary reference frame. **IEEE Transactions on Industry Applications**, v. 50, n. 4, p. 2574–2583, 2014.

_____. Sensorless control strategy by square-waveform high-frequency pulsating signal injection into stationary reference frame. **IEEE Journal of Emerging and Selected Topics in Power Electronics**, v. 2, n. 2, p. 171–180, 2014.

LIU, T.-H.; CHENG, C.-P. Adaptive control for a sensorless permanent-magnet synchronous motor drive. **IEEE Transactions on Aerospace and Electronic Systems**, v. 30, n. 3, p. 900–909, 1994.

LU, J. et al. Detrimental effect elimination of current sensor accuracy uncertainty for high-precision position sensorless control of interior permanent magnet synchronous motor drives. **IEEE Transactions on Industrial Electronics**, v. 67, n. 7, p. 6101–6111, 2020. ISSN 15579948.

LU, X.; LIN, H.; HAN, J. Load disturbance observer-based control method for sensorless pmsm drive. **IET Electric Power Applications**, v. 10, 04 2016.

MATSUI, N. Sensorless pm brushless dc motor drives. **IEEE Transactions on Industrial Electronics**, v. 43, n. 2, p. 300–308, April 1996.

MEESSEN, K. J. et al. Inductance calculations of permanent-magnet synchronous machines including flux change and self- and cross-saturations. **IEEE Transactions on Magnetics**, v. 44, n. 10, p. 2324–2331, 2008.

MIZUTANI, R.; TAKESHITA, T.; MATSUI, N. Current model-based sensorless drives of salient-pole pmsm at low speed and standstill. **IEEE Transactions on Industry Applications**, v. 34, n. 4, p. 841–846, 1998.

MORIMOTO, S.; SANADA, M.; TAKEDA, Y. Wide-speed operation of interior permanent magnet synchronous motors with high-performance current regulator. **IEEE Transactions on Industry Applications**, v. 30, n. 4, p. 920–926, 1994.

MURAKAMI, S. et al. Encoderless servo drive with adequately designed ipmsm for pulse-voltage-injection-based position detection. **IEEE Transactions on Industry Applications**, v. 48, n. 6, p. 1922–1930, 2012.

NAHID-MOBARAKEH, B.; MEIBODY-TABAR, F.; SARGOS, F. M. Mechanical sensorless control of PMSM with online estimation of stator resistance. **IEEE Transactions on Industry Applications**, v. 40, n. 2, p. 457–471, 2004. ISSN 00939994.

NAKASHIMA, S.; INAGAKI, Y.; MIKI, I. Sensorless initial rotor position estimation of surface permanent-magnet synchronous motor. **IEEE Transactions on Industry Applications**, v. 36, n. 6, p. 1598–1603, 2000.

NALAKATH, S.; PREINDL, M.; EMADI, A. Online multi-parameter estimation of interior permanent magnet motor drives with finite control set model predictive control. **IET Electric Power Applications**, Institution of Engineering and Technology, v. 11, p. 944–951(7), May 2017. ISSN 1751-8660.

NALAKATH, S. et al. Optimization-based position sensorless finite control set model predictive control for ipmsms. **IEEE Transactions on Power Electronics**, v. 33, n. 10, p. 8672–8682, Oct 2018.

NOVAK, Z.; NOVAK, M. Design of high-speed permanent magnet synchronous motor for advanced and sensorless control techniques validation. In: **2018 18th International Conference on Mechatronics - Mechatronika (ME)**. [S.l.: s.n.], 2018. p. 1–8.

PACAS, M. Sensorless drives in industrial applications. **IEEE Industrial Electronics Magazine**, v. 5, n. 2, p. 16–23, June 2011. ISSN 1932-4529.

PARK, M.-H.; LEE, H.-H. Sensorless vector control of permanent magnet synchronous motor using adaptive identification. In: **15th Annual Conference of IEEE Industrial Electronics Society**. [S.l.: s.n.], 1989. p. 209–214 vol.1.

PARK, Y.; SUL, S. Sensorless control method for pmsm based on frequency-adaptive disturbance observer. **IEEE Journal of Emerging and Selected Topics in Power Electronics**, v. 2, n. 2, p. 143–151, 2014.

PEREZ, M. A. et al. Modular multilevel converters: Recent achievements and challenges. **IEEE Open Journal of the Industrial Electronics Society**, v. 2, p. 224–239, 2021.

PIIPPO, A.; HINKKANEN, M.; LUOMI, J. Analysis of an adaptive observer for sensorless control of interior permanent magnet synchronous motors. **IEEE Transactions on Industrial Electronics**, v. 55, n. 2, p. 570–576, Feb 2008. ISSN 0278-0046.

_____. Adaptation of motor parameters in sensorless pmsm drives. **IEEE Transactions on Industry Applications**, v. 45, n. 1, p. 203–212, 2009.

PIIPPO, A.; LUOMI, J. Adaptive observer combined with hf signal injection for sensorless control of pmsm drives. In: **IEEE International Conference on Electric Machines and Drives, 2005.** [S.l.: s.n.], 2005. p. 674–681.

PLUNKETT, A. B.; TURNBULL, F. G. Load-commutated inverter/synchronous motor drive without a shaft position sensor. **IEEE Transactions on Industry Applications**, IA-15, n. 1, p. 63–71, 1979.

PO-NGAM, S.; SANGWONGWANICH, S. Stability and dynamic performance improvement of adaptive full-order observers for sensorless pmsm drive. **IEEE Transactions on Power Electronics**, v. 27, n. 2, p. 588–600, 2012.

POORFAKHRAEI, A.; NARIMANI, M.; EMADI, A. A review of multilevel inverter topologies in electric vehicles: Current status and future trends. **IEEE Open Journal of Power Electronics**, v. 2, p. 155–170, 2021.

QIAO, Z. et al. New sliding-mode observer for position sensorless control of permanent-magnet synchronous motor. **IEEE Transactions on Industrial Electronics**, v. 60, n. 2, p. 710–719, 2013.

QU, L.; QIAO, W.; QU, L. An Enhanced Linear Active Disturbance Rejection Rotor Position Sensorless Control for Permanent Magnet Synchronous Motors. **IEEE Transactions on Power Electronics**, v. 35, n. 6, p. 6175–6184, 2020. ISSN 19410107.

R, S.; Singh, B. Sensorless predictive control of spmsm-driven light ev drive using modified speed adaptive super twisting sliding mode observer with maf-pll. **IEEE Journal of Emerging and Selected Topics in Industrial Electronics**, v. 2, n. 1, p. 42–52, 2021.

RACA, D. et al. A comparative analysis of pulsating vs. rotating vector carrier signal injection-based sensorless control. In: **2008 Twenty-Third Annual IEEE Applied Power Electronics Conference and Exposition**. [S.l.: s.n.], 2008. p. 879–885.

RAFAQ, M. S.; JUNG, J. W. A Comprehensive Review of State-of-the-Art Parameter Estimation Techniques for Permanent Magnet Synchronous Motors in Wide Speed Range. **IEEE Transactions on Industrial Informatics**, IEEE, v. 16, n. 7, p. 4747–4758, 2020. ISSN 19410050.

RAFAQ, M. S. et al. Online Parameter Identification for Model-Based Sensorless Control of Interior Permanent Magnet Synchronous Machine. **IEEE Transactions on Power Electronics**, IEEE, v. 32, n. 6, p. 4631–4643, 2017. ISSN 08858993.

RAMESH, P.; LENIN, N. C. High power density electrical machines for electric vehicles—comprehensive review based on material technology. **IEEE Transactions on Magnetics**, v. 55, n. 11, p. 1–21, 2019.

RAMEZANI, M. et al. A Simple Approach to Enhance the Performance of Complex-Coefficient Filter-Based PLL in Grid-Connected Applications. **IEEE Transactions on Industrial Electronics**, v. 65, n. 6, p. 5081–5085, 2018. ISSN 02780046.

RASHED, M. et al. Sensorless indirect-rotor-field-orientation speed control of a permanent-magnet synchronous motor with stator-resistance estimation. **IEEE Transactions on Industrial Electronics**, v. 54, n. 3, p. 1664–1675, 2007. ISSN 02780046.

REIMERS, J. et al. Automotive traction inverters: Current status and future trends. **IEEE Transactions on Vehicular Technology**, v. 68, n. 4, p. 3337–3350, 2019.

REN21. **Renewables 2021 Global Status Report**. [S.l.: s.n.], 2021.

SANGWONGWANICH, S. et al. A unified speed estimation design framework for sensorless ac motor drives based on positive-real property. In: **2007 Power Conversion Conference - Nagoya**. [S.l.: s.n.], 2007. p. 1111–1118.

SAYED, E. et al. Review of electric machines in more/hybrid/turbo electric aircraft. **IEEE Transactions on Transportation Electrification**, p. 1–1, 2021.

SCHROEDL, M. Sensorless control of ac machines at low speed and standstill based on the "inform" method. In: **IAS '96. Conference Record of the 1996 IEEE Industry Applications Conference Thirty-First IAS Annual Meeting**. [S.l.: s.n.], 1996. v. 1, p. 270–277 vol.1.

SEILMEIER, M.; PIEPENBREIER, B. Sensorless control of pmsm for the whole speed range using two-degree-of-freedom current control and hf test current injection for low-speed range. **IEEE Transactions on Power Electronics**, v. 30, n. 8, p. 4394–4403, 2015.

SEPE, R. B.; LANG, J. H. Real-time observer-based (adaptive) control of a permanent-magnet synchronous motor without mechanical sensors. **IEEE Transactions on Industry Applications**, v. 28, n. 6, p. 1345–1352, 1992.

SEPULCHRE, L. et al. Mtpv flux-weakening strategy for pmsm high speed drive. **IEEE Transactions on Industry Applications**, v. 54, n. 6, p. 6081–6089, 2018.

SHI, Y. et al. Online identification of permanent magnet flux based on extended Kalman filter for IPMSM drive with position sensorless control. **IEEE Transactions on Industrial Electronics**, IEEE, v. 59, n. 11, p. 4169–4178, 2012. ISSN 02780046.

SMIDL, V.; PEROUTKA, Z. Advantages of square-root extended kalman filter for sensorless control of ac drives. **IEEE Transactions on Industrial Electronics**, v. 59, n. 11, p. 4189–4196, 2012.

SOLSONA, J.; VALLA, M.; MURAVCHIK, C. Nonlinear control of a permanent magnet synchronous motor with disturbance torque estimation. **IEEE Transactions on Energy Conversion**, v. 15, n. 2, p. 163–168, 2000. ISSN 08858969.

SOLSONA, J.; VALLA, M. I.; MURAVCHIK, C. A nonlinear reduced order observer for permanent magnet synchronous motors. **IEEE Transactions on Industrial Electronics**, v. 43, n. 4, p. 492–497, 1996. ISSN 02780046.

SONG, X. et al. Adaptive compensation method for high-speed surface pmsm sensorless drives of emf-based position estimation error. **IEEE Transactions on Power Electronics**, v. 31, n. 2, p. 1438–1449, 2016.

STAINES, C.; ASHER, G.; SUMNER, M. Rotor-position estimation for induction machines at zero and low frequency utilizing zero-sequence currents. **IEEE Transactions on Industry Applications**, v. 42, n. 1, p. 105–112, 2006.

STAINES, C. et al. Sensorless control of induction machines at zero and low frequency using zero sequence currents. **IEEE Transactions on Industrial Electronics**, v. 53, n. 1, p. 195–206, 2006.

SUN, L. et al. Investigation of a practical convex-optimization-based sensorless scheme for ipmsm drives. **IEEE Transactions on Power Electronics**, v. 34, n. 12, p. 12437–12452, 2019.

TAHANIAN, H.; ALIAHMADI, M.; FAIZ, J. Ferrite permanent magnets in electrical machines: Opportunities and challenges of a non-rare-earth alternative. **IEEE Transactions on Magnetics**, v. 56, n. 3, p. 1–20, 2020.

TANG, Q. et al. Ipmsms sensorless mtpa control based on virtual q-axis inductance by using virtual high-frequency signal injection. **IEEE Transactions on Industrial Electronics**, v. 67, n. 1, p. 136–146, Jan 2020.

TARVIRDILU-ASL, R. et al. Improved online optimization-based optimal tracking control method for induction motor drives. **IEEE Transactions on Power Electronics**, v. 35, n. 10, p. 10654–10672, 2020.

TEDESCO, F.; CASAVOLA, A.; FEDELE, G. Unbiased Estimation of Sinusoidal Signal Parameters via Discrete-Time Frequency-Locked-Loop Filters. **IEEE Transactions on Automatic Control**, v. 62, n. 3, p. 1484–1490, 2017. ISSN 00189286.

TOMITA, M.; HASEGAWA, M.; MATSUI, K. A design method of full-order extended electromotive force observer for sensorless control of ipmsm. In: **2010 11th IEEE International Workshop on Advanced Motion Control (AMC)**. [S.l.: s.n.], 2010. p. 206–209.

TOMITA, M. et al. New sensorless control for brushless dc motors using disturbance observers and adaptive velocity estimations. **IEEE Transactions on Industrial Electronics**, v. 45, n. 2, p. 274–282, April 1998. ISSN 0278-0046.

TUOVINEN, T. et al. Comparison of a reduced-order observer and a full-order observer for sensorless synchronous motor drives. **IEEE Transactions on Industry Applications**, v. 48, n. 6, p. 1959–1967, 2012.

VACLAVEK, P.; BLAHA, P.; HERMAN, I. Ac drive observability analysis. **IEEE Transactions on Industrial Electronics**, v. 60, n. 8, p. 3047–3059, 2013.

VINH, L. Optimization design of the magnetic system for double rotor synchronous generator with permanent magnets. In: . [S.l.: s.n.], 2016.

WANG, G. et al. Enhanced position observer using second-order generalized integrator for sensorless interior permanent magnet synchronous motor drives. **IEEE Transactions on Energy Conversion**, v. 29, n. 2, p. 486–495, 2014. ISSN 08858969.

_____. Rotor position estimation of pmsm in low-speed region and standstill using zero-voltage vector injection. **IEEE Transactions on Power Electronics**, v. 33, n. 9, p. 7948–7958, 2018.

_____. Position estimation error reduction using recursive-least-square adaptive filter for model-based sensorless interior permanent-magnet synchronous motor drives. **IEEE Transactions on Industrial Electronics**, v. 61, n. 9, p. 5115–5125, 2014. ISSN 02780046.

_____. Quadrature pll-based high-order sliding-mode observer for ipmsm sensorless control with online mtpa control strategy. **IEEE Transactions on Energy Conversion**, v. 28, n. 1, p. 214–224, 2013.

WANG, G.; VALLA, M.; SOLSONA, J. Position sensorless permanent magnet synchronous machine drives—a review. **IEEE Transactions on Industrial Electronics**, v. 67, n. 7, p. 5830–5842, 2020.

WANG, G. et al. Comparative investigation of pseudorandom high-frequency signal injection schemes for sensorless ipmsm drives. **IEEE Transactions on Power Electronics**, v. 32, n. 3, p. 2123–2132, 2017.

WANG, G.; YANG, R.; XU, D. DSP-based control of sensorless IPMSM drives for wide-speed-range operation. **IEEE Transactions on Industrial Electronics**, v. 60, n. 2, p. 720–727, 2013. ISSN 02780046.

WANG, G. et al. Adaptive compensation method of position estimation harmonic error for EMF-based observer in sensorless IPMSM drives. **IEEE Transactions on Power Electronics**, v. 29, n. 6, p. 3055–3064, 2014. ISSN 08858993.

WANG, Q. et al. Offline Parameter Self-Learning Method for General-Purpose PMSM Drives with Estimation Error Compensation. **IEEE Transactions on Power Electronics**, IEEE, v. 34, n. 11, p. 11103–11115, 2019. ISSN 19410107.

WANG, X. et al. A simple and effective compensation method for inverter nonlinearity. In: **2020 IEEE Transportation Electrification Conference and Expo, ITEC 2020**. [S.l.: s.n.], 2020. p. 638–643. ISBN 9781728146294.

WANG, Y.; XU, Y.; ZOU, J. Sliding-mode sensorless control of pmsm with inverter nonlinearity compensation. **IEEE Transactions on Power Electronics**, v. 34, n. 10, p. 10206–10220, 2019.

_____. ILC-Based Voltage Compensation Method for PMSM Sensorless Control Considering Inverter Nonlinearity and Sampling Current DC Bias. **IEEE Transactions on Industrial Electronics**, v. 67, n. 7, p. 5980–5989, 2020. ISSN 15579948.

WANG, Z. et al. Position sensorless control of interleaved csi fed pmsm drive with extended kalman filter. **IEEE Transactions on Magnetics**, v. 48, n. 11, p. 3688–3691, Nov 2012.

WEG. **WMagnet drive system**. [S.l.: s.n.], 2013.

WU, B. **High-Power Converters and ac Drives**. [S.l.: s.n.], 2005. 1–332 p. ISBN 0471731714.

WU, C.; ZHAO, Y.; SUN, M. Enhancing Low-Speed Sensorless Control of PMSM Using Phase Voltage Measurements and Online Multiple Parameter Identification. **IEEE Transactions on Power Electronics**, IEEE, v. 35, n. 10, p. 10700–10710, 2020. ISSN 19410107.

WU, R.; SLEMON, G. R. A permanent magnet motor drive without a shaft sensor. **IEEE Transactions on Industry Applications**, v. 27, n. 5, p. 1005–1011, 1991.

WU, S.; ZHANG, J.; CHAI, B. Adaptive super-twisting sliding mode observer based robust backstepping sensorless speed control for ipmsm. **ISA Transactions**, v. 92, p. 155 – 165, 2019. ISSN 0019-0578.

WU, X. et al. Enhanced position sensorless control using bilinear recursive least squares adaptive filter for interior permanent magnet synchronous motor. **IEEE Transactions on Power Electronics**, v. 35, n. 1, p. 681–698, 2020.

XIA, Z. et al. Computation-Efficient Online Optimal Tracking Method for Permanent Magnet Synchronous Machine Drives for MTPA and Flux-Weakening Operations. **IEEE Journal of Emerging and Selected Topics in Power Electronics**, 2020. ISSN 21686785.

XIAO, D. et al. Universal full-speed sensorless control scheme for interior permanent magnet synchronous motors. **IEEE Transactions on Power Electronics**, p. 1–1, 2020.

_____. Universal Full-Speed Sensorless Control Scheme for Interior Permanent Magnet Synchronous Motors. **IEEE Transactions on Power Electronics**, v. 36, n. 4, p. 4723–4737, 2021. ISSN 19410107.

_____. Complex-coefficient adaptive disturbance observer for position estimation of IPMSMs with robustness to DC Errors. **IEEE Transactions on Industrial Electronics**, v. 67, n. 7, p. 5924–5935, 2020. ISSN 15579948.

_____. Computation-Efficient Position Estimation Algorithm for Permanent Magnet Synchronous Motor Drives Under Distorted Conditions. **IEEE Journal of Emerging and Selected Topics in Power Electronics**, p. 1–1, 2020. ISSN 21686785.

XIE, G. et al. Permanent magnet flux online estimation based on zero-voltage vector injection method. **IEEE Transactions on Power Electronics**, v. 30, n. 12, p. 6506–6509, 2015.

XU, W. et al. Improved Nonlinear Flux Observer-Based Second-Order SOIFO for PMSM Sensorless Control. **IEEE Transactions on Power Electronics**, v. 34, n. 1, p. 565–579, 2018. ISSN 08858993.

_____. An improved adaptive sliding mode observer for middle- and high-speed rotor tracking. **IEEE Transactions on Power Electronics**, v. 36, n. 1, p. 1043–1053, 2021.

YANG, S. Saliency-based position estimation of permanent-magnet synchronous machines using square-wave voltage injection with a single current sensor. **IEEE Transactions on Industry Applications**, v. 51, n. 2, p. 1561–1571, 2015.

YANG, S.; CHEN, G. High-speed position-sensorless drive of permanent-magnet machine using discrete-time emf estimation. **IEEE Transactions on Industrial Electronics**, v. 64, n. 6, p. 4444–4453, 2017.

YANG, S. C.; HSU, Y. L. Full Speed Region Sensorless Drive of Permanent-Magnet Machine Combining Saliency-Based and Back-EMF-Based Drive. **IEEE Transactions on Industrial Electronics**, v. 64, n. 2, p. 1092–1101, 2017. ISSN 02780046.

YAO, Y.; HUANG, Y.; PENG, F. Position sensorless drive of high speed permanent magnet synchronous motor. In: **2018 IEEE Energy Conversion Congress and Exposition (ECCE)**. [S.l.: s.n.], 2018. p. 1733–1740.

YAO, Y. et al. Position Sensorless Drive and Online Parameter Estimation for Surface-Mounted PMSMs Based on Adaptive Full-State Feedback Control. **IEEE Transactions on Power Electronics**, IEEE, v. 35, n. 7, p. 7341–7355, 2020. ISSN 19410107.

YE, S.; YAO, X. A Modified Flux Sliding-Mode Observer for the Sensorless Control of PMSMs with Online Stator Resistance and Inductance Estimation. **IEEE Transactions on Power Electronics**, IEEE, v. 35, n. 8, p. 8652–8662, 2020. ISSN 19410107.

YUAN, L. et al. Sensorless control of high-power interior permanent-magnet synchronous motor drives at very low speed. **IET Electric Power Applications**, v. 7, n. 3, p. 199–206, 2013.

ZALTNI, D. et al. Observability analysis of pmsm. In: **2009 3rd International Conference on Signals, Circuits and Systems (SCS)**. [S.l.: s.n.], 2009. p. 1–6.

ZHANG, G. et al. Pseudorandom-frequency sinusoidal injection based sensorless ipmsm drives with tolerance for system delays. **IEEE Transactions on Power Electronics**, v. 34, n. 4, p. 3623–3632, 2019.

_____. ADALINE-network-based PLL for position sensorless interior permanent magnet synchronous motor drives. **IEEE Transactions on Power Electronics**, v. 31, n. 2, p. 1450–1460, 2016. ISSN 08858993.

_____. Multiple-AVF Cross-Feedback-Network-Based Position Error Harmonic Fluctuation Elimination for Sensorless IPMSM Drives. **IEEE Transactions on Industrial Electronics**, v. 63, n. 2, p. 821–831, 2016. ISSN 02780046.

_____. Discrete-time low-frequency-ratio synchronous-frame full-order observer for position sensorless ipmsm drives. **IEEE Journal of Emerging and Selected Topics in Power Electronics**, v. 5, n. 2, p. 870–879, 2017.

ZHANG, X. et al. Improved initial rotor position estimation for pmsm drives based on hf pulsating voltage signal injection. **IEEE Transactions on Industrial Electronics**, v. 65, n. 6, p. 4702–4713, 2018.

ZHAO, J.; NALAKATH, S.; EMADI, A. A high frequency injection technique with modified current reconstruction for low-speed sensorless control of ipmsms with a single dc-link current sensor. **IEEE Access**, v. 7, p. 136137–136147, 2019.

ZHAO, W. et al. Sensorless control of a linear permanent-magnet motor based on an improved disturbance observer. **IEEE Transactions on Industrial Electronics**, v. 65, n. 12, p. 9291–9300, 2018.

ZHAO, Y.; QIAO, W.; WU, L. An adaptive quasi-sliding-mode rotor position observer-based sensorless control for interior permanent magnet synchronous machines. **IEEE Transactions on Power Electronics**, v. 28, n. 12, p. 5618–5629, 2013.

_____. Improved rotor position and speed estimators for sensorless control of interior permanent-magnet synchronous machines. **IEEE Journal of Emerging and Selected Topics in Power Electronics**, v. 2, n. 3, p. 627–639, Sep. 2014.

_____. Dead-time effect analysis and compensation for a sliding-mode position observer-based sensorless ipmsm control system. **IEEE Transactions on Industry Applications**, v. 51, n. 3, p. 2528–2535, 2015.

ZHAO, Y. et al. An extended flux model-based rotor position estimator for sensorless control of salient-pole permanent-magnet synchronous machines. **IEEE Transactions on Power Electronics**, v. 30, n. 8, p. 4412–4422, 2015.

ZHU, G. et al. A nonlinear state observer for the sensorless control of a permanent-magnet AC machine. **IEEE Transactions on Industrial Electronics**, v. 48, n. 6, p. 1098–1108, 2001. ISSN 02780046.

ZHU, Z. Q. et al. Estimation of winding resistance and PM flux-linkage in brushless AC machines by reduced-order extended kalman filter. **2007 IEEE International Conference on Networking, Sensing and Control, ICNSC'07**, n. April, p. 740–745, 2007.

Appendix A - Experimental Setup

The experimental setup used in this Thesis is composed of an interface with a DSP TMS320F28335, two voltage source inverters (VSI), an IPMSM and an induction motor (IM) as load. The experimental results are obtained with sampling and inverter switching frequency of 10 kHz. Speed and current regulation are performed by PI controllers through a oriented field framework. The Euler method is employed for integration of the differential equations of the adaptive observer in discrete-time. An absolute encoder gives the actual rotor position and rotor speed. The simplified diagram of the implemented sensorless control system is illustrated in Fig..1 and the experimental setup photograph is presented Fig..2. The IPMSM parameters are presented in Table 7.

Figure .1: Experimental setup block diagram.

Source: Author.

Figure .2: Experimental setup.

Source: DOI: 10.1109/TIE.2020.3007101, ©2021 IEEE.

The IM field oriented current control is performed disregarding the nonlinear effects (TARVIRDILU-ASL et al., 2020). Therefore, linear MTPA is implemented.

Rated power	11 kW	Stator resistance	0.5 Ω
Rated speed	188 rad/s	q-axis inductance	40.9 mH
Pole pairs	3	d-axis inductance	20.1 mH
PM flux linkage	0.512 Wb	DC link voltage	500 V

Table 7: IPMSM Parameters

Appendix B - Copyright Statement

This Thesis present reuse content from the following published articles:

- **C. J. V. Filho**, D. Xiao, R. P. Vieira and A. Emadi, "Observers for High-Speed Sensorless PMSM Drives: Design Methods, Tuning Challenges and Future Trends," in **IEEE Access**, vol. 9, pp. 56397-56415, 2021, doi: 10.1109/ACCESS.2021.3072360.

- **C. J. Volpato Filho** and R. P. Vieira, "Adaptive Full-Order Observer Analysis and Design for Sensorless Interior Permanent Magnet Synchronous Motors Drives," in **IEEE Transactions on Industrial Electronics**, vol. 68, no. 8, pp. 6527-6536, Aug. 2021, doi: 10.1109/TIE.2020.3007101.

As required by IEEE copyright guidelines, the following message is included: